Ana Sofia Tomaz Teixeira de Pádua

Graduation in Engineering of Micro and Nanotechnologies

Study and development of synthetic bone strips for spine fusion applications

Dissertation to obtain the Master's degree in

Engineering of Micro and Nanotechnologies

Supervisor: João Paulo Borges, Associate Professor with Habilitation, Universidade Nova de Lisboa

Co-Supervisor: Lígia Figueiredo, PhD, Bioceramed

Panel:

Presidente: Prof. Doutor Rodrigo Ferrão de Paiva Martins

Arguente(s): Prof. Doutora Célia Maria Reis Henriques

Vogal(ais): Prof. Doutora Lígia Margarida Jorge de Figueiredo

FACULDADE DE CIÊNCIAS E TECNOLOGIA
UNIVERSIDADE NOVA DE LISBOA

November 2019

Study and development of synthetic bone strips for spine fusion applications

“The greatest enemy of knowledge is not ignorance,

it is the illusion of knowledge.”

Daniel J. Boorstin

Agradecimentos

Este trabalho é o resultado de uma longa jornada que só foi possível com toda a ajuda das pessoas espantosas que me acompanharam e ajudaram nos últimos anos. Assim gostaria de agradecer primeiramente ao Professor Rodrigo Martins e à Professor Elvira Fortunato pela criação do curso de Engenharia de Micro e Nanotecnologias com o qual cresci intelectualmente, abri os meus horizontes e também conheci pessoas espetaculares de culturas e perspetivas completamente diferentes.

Em segundo lugar, gostaria de agradecer ao meu orientador, Doutor João Paulo Borges por todo o apoio dado no decorrer deste trabalho, pelas sugestões e conhecimentos transmitidos, pelas palavras de incentivo e de calma quando destas precisava, e à minha coorientadora, Doutora Lígia Figueiredo, por toda a disponibilidade tanto em receber-me na Bioceramed, como em facultar-me materiais para as minhas amostras e por todos os conhecimentos de âmbito empresarial que necessitei.

Gostaria também de agradecer a todos os professores e investigadores do DCM que me ajudaram ao longo destes últimos meses sempre com a maior disponibilidade e enorme simpatia como a Doutora Paula Soares, ao Professor João Canejo, a Professora Susete Fernandes e ao Doutor Ricardo Chagas. Ainda gostaria de agradecer a todos os professores e responsáveis que possibilitaram a realização das análises como a Professora Rita Branquinho, Professora Joana Pinto, Doutora Ana Pimentel, Doutora Sónia Pereira e, especialmente, à Deneb, por me ter aturado dezenas de horas para ver as minhas amostras em SEM.

Um especial obrigado a todo o laboratório de cultura celular, mas principalmente ao Professor Jorge Silva, não só por me ter ensinado e acompanhado em todos os procedimentos que realizei como também pelas horas infindáveis que dedicou para debatermos resultados e a aperfeiçoar técnicas de modo a que se enquadrassem aos meus estudos. Gostaria de agradecer também à Professora Célia Henriques que mesmo não sendo a responsável por mim sempre demonstrou imensa simpatia e disponibilidade mesmo que fosse só para coordenar a utilização da câmara celular. Ainda do laboratório de cultura celular, gostaria de agradecer pelo bom ambiente que sempre me receberam, da preocupação se tinha ou não tinha tido tempo para almoçar e pelos docinhos e todos os chocolates. Assim, aqui fica um grande abraço para a Alice (que mais que ninguém percebe os stresses e desgostos de trabalho que passamos), Ema (sempre com um sorriso na cara e uma energia contagiante), Sara (com paciência infindável para duvidas de química), José Diogo (pela companha e conversas não relacionadas com trabalho), Catariana (por toda a boa disposição mesmo nos dias complicados) e Tânia (pelo bom ambiente, fotos do bebe fofo e ajuda na camara celular).

À equipa da Bioceramed gostava de agradecer por me terem recebido de braços abertos principalmente ao Doutor Eduardo Pires por ter permitido a colaboração com a FCT e a elaboração deste tema, à Andreia Pimenta que acompanhou todo o processo da tese e ao Diogo Cartaxo que teve a disponibilidade de criar um mini reator de modo a testarmos possíveis alterações aos processos de síntese da Bioceramed.

Gostaria ainda de agradecer a todas as pessoas que suportaram o meu stress no dia a dia e que sem a colaboração deles não teria conseguido terminar este trabalho a horas. Assim fica um gigantesco obrigada à Adriana, Cesar, David, JP, Margarida, Beatriz, Miguel e Rita. Um especial obrigada à Bárbara por todas as conversas (não de trabalho para variar), companhia ao longo de placas e placas de células e apoio, mesmo quando a exaustão era muita para as duas, ao João e à Íris por todas as horas que ficaram no laboratório para que eu pudesse ficar a trabalhar, pelas ajudas com as minhas mil e uma amostras (quase como se fossem uma fábrica chinesa), por todas as ajudas no “washie, washie” mas mais que todo pelas brincadeiras que quase sempre melhoraram os meus dias.

Ainda nesta grande família, FCT gostava, de agradecer a todos os alunos de doutoramento que me ajudaram e aconselharam neste percurso, o Ricardo por todas as duvidas e organização do laboratório, a Catarina, que além de ter levado as minhas amostras para TEM estava sempre pronta para ajudar com um sorriso gigantesco, ao Diogo Ramos, por todos os conhecimentos transmitidos, o Henrique, pelas fofocas e por se ter voluntariado para aprender a funcionar com um reómetro do seculo passado e o Diogo Saraiva por todas as vezes que o interrompi à procura de algum material de laboratório.

Não posso deixar de agradecer não só aos meus colegas destes cinco anos, com quem passei pelas dificuldades e alegrias, mas também às minhas amigas Catariana e Marta que sempre estivarem aqui e que nestes meses arranjaram sempre um tempinho para um café (a.k.a. Starbucks) ou um lanche mesmo quando as horas que podia não eram as melhores.

Por fim, gostaria de agradecer às pessoas mais importantes a minha família, especialmente aos meus pais por sempre me terem ensinado a lutar e a não desistir dos meus objetivos mesmo quando parecem inatingíveis, obrigado por serem a minha rede de suporte e por aturarem todo o meu stress, o meu vício em trabalho, o meu raro mau feito e a minha cabeça no ar. Obrigada à minha avó e tio que sempre estiveram lá e acreditaram me mim mais do que eu própria acreditei.

P.S. Aproveito também para pedir desculpa por ter ocupado quase todas as mesas do laboratório e a estufa com o meu exército de caixinhas.

Abstract

The increase of musculoskeletal diseases and trauma injuries due to the changes in the human life style in the more recent decades has been one of the major driving forces of the research for bone substitutes and regeneration. The most recent researches and the best products in the market, point to polymeric/ceramic composite grafts, as they have shown the best results on bone regeneration.

In this work different composite scaffolds were developed, with the purpose to identify the ones with adequate structure and properties. The produced scaffolds are based on chitosan (CH) with small and Large Molecular Weights (MW) and ceramics like biphasic ceramics (75% hydroxyapatite and 25% β-TCP), mesoporous bioactive glass (MBG), mesoporous hydroxyapatite (MHap), in different concentrations and a combination of the mesoporous materials (12.5% MHap/12.5% MBG and 25% MHap/25% MBG).

The mesoporous ceramics were produced by the sol-gel method with Pluronic® as surfactant. The membranes were obtained by lyophilization of the composite suspension. Resulting membranes were neutralized and dialyzed so they would not dissolve on contact with liquids.

The new MHAp showed a lower crystallization temperature in the XRD, FTIR and DST-TGA analysis. The samples were also analyzed by TEM.

The composites had a high porous structure, with interconnected pores. Furthermore, the scaffolds with higher ceramic content presented column like pores and compressive modules increased with the ceramic concentration.

The materials used in the composites and the composites themselves, were tested for cytotoxicity, and none presented any cytotoxic response. In addition, adhesion tests showed that scaffolds produced with CH of lower molecular weight, have higher cell adhesion and proliferation than those produced with CH of high molecular weight. Moreover, compositions involving the mixture of MHap and MBG presented the best adhesion and proliferation results.

Sumário

Um dos maiores impulsionadores da investigação de substitutos e regeneradores ósseos tem sido o aumento das doenças e lesões osteo musculares, devido às mudanças de comportamento humano nas mais recentes décadas. Destes substitutos destacam-se os compósitos de base cerâmica e polimérica, devido aos resultados muito positivos conhecidos, durante a fase de investigação, bem como quando já integrados em produtos existentes no mercado.

Neste trabalho são desenvolvidos diferentes compósitos, com o propósito de identificar a composição com a estrutura e propriedades mais adequadas aos mesmo. Os compósitos produzidos tiveram como base o quitosano (CH) com baixo e alto peso molecular, bem como diferentes concentrações de bifásicos (75% hidroxiapatite/25% β-TCP), Bio vidro mesoporosos (MBG), Hidroxiapatite mesoporosos (MHAp) e a combinação dos materiais mesoporosos (12,5% MHap/12,5% MBG e 25% MHap/25% MBG).

Os cerâmicos mesoporosos foram sintetizados em sol-gel com adição de Pluronic® como elemento surfactante. As membranas resultantes das suspensões compósitas foram obtidas por liofilização, posteriormente neutralizadas e finalmente dialisadas, para não se dissolverem em contacto com líquidos.

A MHAp analisada por difração de raio-X (XRD), FTIR e DST-TGA demonstrou que esta nova estrutura apresenta menor temperatura de cristalização. Recorreu-se também ao TEM para analisar este material.

Os compósitos apresentaram uma estrutura porosa, com poros interconectados e nas composições com maior percentagem de cerâmicos, formam-se poros colunares ao longo da amostra. Por sua vez o modulo de compressão das membranas aumentou com o aumento da concentração de cerâmicos nas membranas.

Todos os materiais utilizados nos compósitos e os próprios compósitos foram submetidos a testes de cito toxicidade e nenhum apresentou propriedades citotóxicas. Por outro lado, os testes de adesão demonstraram que CH de baixo peso molecular apresentou melhores adesões e proliferações celulares que o polímero de elevado peso molecular. Em adição, os materiais que tiveram a melhor adesão e proliferação foram os compósitos constituídos por ambos os materiais mesoporosos

Table of Contents

List of Figures

List of Figures in Appendix

List of Tables

List of Abbreviations

α-TCP - α tricalcium phosphate

BET - Barrett– Emmett–Teller

BJH - Barret–Joyner–Halenda

BPC - biphasic ceramics

β-TCP - β tricalcium phosphate

CH - Chitosan

CHL - Chitosan with low molecular weights

CHH - Chitosan with high molecular weights

DALY - Disability-Adjusted Life-Years

DD - Degree of Deacetylation

DMSO - Dimethyl sulfoxide

DSC - Differential Scanning Calorimetry

ECBM - extracellular bone matrix

EISA - Self-assembly

EU - European Union

F127 - Pluronic F127

FR - ForRegen

FTIR - Fourier-Transform Infrared Spectroscopy

HAp – hydroxyapatite

MC – Mesoporous composite

MBG – Mesoporous Bioglass

MHAp - Mesoporous hydroxyapatite

MSK - Musculoskeletal

MW - Molecular Weights

NA - not available

nHAp - Nano hydroxyapatite

NP - nanoparticles

OA - Osteoarthritis

PBS - Phosphate buffered saline

PEO - Poly (Ethylene Oxide)

PGA - poly-glycolic acid

PLA - poly-lactic acid

PLGA - poly- (lactide-co-glycolide)

PMMA - poly (methyl methacrylate)

poly-HEMA - Poly-hydroxyethylmethacrylate

PPO - Poly (Propylene Oxide)

PUR - poly (urethane)

RA - Rheumatoid Arthritis

SBF - Simulated Body Fluid

SEM - Scanning Electron Microscopy

TEOS - Tetraethyl orthosilicate

TEM - Transmission electron microscopy

TEP - Triethyl Phosphate

TGA - thermogravimetry analysis

XRD - X-ray diffraction

Motivation

One of the major social goals for this century is life quality improvement (including paid reduction, enhanced mobility and autonomy, increase life expectancy) and overall wellbeing. However, the rising geriatric population and sedentary lifestyles increased problems such as the chronic skeletal conditions and Musculoskeletal disorders (MSK). The MSK includes issues as severe as low back and neck pain, hip and knee osteoarthritis (OA), rheumatoid arthritis (RA), gout and low bone mineral density and bone mass (Osteoporosis) which are becoming the most common causes of disability worldwide, the Disability-Adjusted Life Years (DALY) is worsening also due to debilitant fractures that reach 5.8 million of which 51% in Europe and North America. [1]–[4]

Just in the European Union (EU) the number of new fractures in 2010 due to Osteoporosis, was estimated at 3.5 million, comprising approximately 620,000 hip fractures, 520,000 vertebral fractures, 560,000 forearm fractures and 1,800,000 other fractures. Related to these fractures was estimated 43,000 deaths. These numbers are predicted to increase 28% to a total of 4.5 million in 2025. [5]

The goal of achieving an increased overall wellbeing, have boost the researches on biomaterials/biomedical materials for bone implantation, replacement and regeneration of organs over the last four decades with consistent growth of global market demand. [6], [7]

Likewise, the spine injuries and disorders affect life quality. These spine problems include defects caused by spine trauma, congenital anomalies, infections and degenerative diseases. Currently the majority of spine treatments recourse to spine fusions. Within next generation orthopedic biomaterials tailor-made, aim to meet the need of each patient, orthopedic procedure and make it the less evasive possible at the lowest price. [3], [8]

Next generation materials will attempt to reproduce the various properties of the original tissue, to aid the regeneration and consolidation of bone. These new materials share an improved composition similar to bone structure (e.g. chitosan), mineral phase (HAp) and mechanical properties. These improvements lead to biomaterials production of 3D hierarchical structures design, to improve bone regeneration. [8]

The main objective of this work is to develop a lyophilized porous strip for bone regeneration applications composed of a mixture of calcium phosphates, bioglass and natural polymer (chitosan), thus conferring good biological properties. The ultimate goal is to study potential materials and compositions, that in the future can be used as products for posterolateral spine fusion applications, with CE marking.

The next section contains a short introduction to ECBM and biomaterials evolution, as context for bone-mimicking biomaterials research and development understanding.

1 Introduction

1.1 Bone structure and composition

The composition of secondary bone is important focus of this work. These bones are found in both mature cortical and cancellous bones. The cortical bones have a dense and compact structure as the cancellous bones have a trabecular or spongy, with less organization than cortical fraction. [9]–[11]

The overall composition of the extracellular matrix of bone, is about 25 wt% organic components (glycoproteins, proteoglycans, sialoproteins, bone "gla" proteins), 65 wt% mineral component like hydroxyapatite (HAp) ($Ca_{10}(PO_4)_6(OH)_2$), and 10 wt% water content, except for the various cell types that populate the matrix. [10], [12]

The organic matrix of bone represented in Figure 1.1 consists approximately of 90 wt% type I fibrillar collagen and 10 wt% noncollagenous proteins. Type-I collagen molecules aggregate in triple helices (tropocollagen) which are stacked longitudinally (Figure 1.1 D). [13] A collagen fibril is made up of staggered rows of axially packed and tropocollagen molecules with lateral crosslinks. [10], [14]–[16] These crosslinks can be enzymatic or nonenzymatic. [17]–[20]

The enzymatic links are further divided into divalent immature ketoimines and trivalent mature pyridinium crosslinks. Their total amount and ratio are related to the mechanical properties of bone, such as stiffness, tensile strength, and fracture toughness. [17]–[20] The divalent are formed via the action of the enzymes lysyl oxidase and lysyl hydroxylase, that then undergo spontaneous reaction to form a trivalent mature pyridinium cross-link and strengthens the bone structure. [18], [20] The nonenzymatic crosslinks result from accumulation of product's advanced glycation end (AGE) and are correlated with increased of bone brittleness due to aging or disease. [17], [18], [21]

The spaces within the collagen fibril are templates that are populated by mineral during bone formation. While collagen is the main organic component of the extracellular matrix, the matrix contains a multitude of other noncollagenous proteins (NCPs). [21], [22] This proteins have a regulatory function in the process of biomineralization, but some, like Osteopontin (OPN), also have direct implications for the mechanical properties of bone, though their structural role in the formation and regulation of the extracellular matrix. [23], [24]

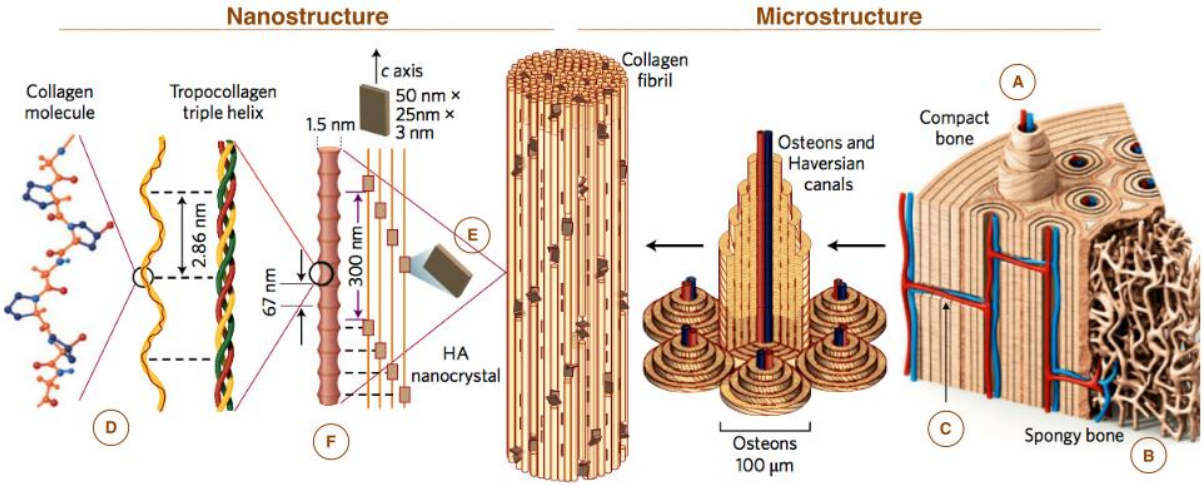

Figure 1.1 - Hierarchical structure of bone from nanostructural (Collagen) to microstructural. Where A is the Haversian system; B) trabecula; C) Volkmann's canal; D) collagen; E) hydroxyapatite crystal and F) collagen fibril. Adopted from [25]

Bone mineral or bone apatite, can be found inside the collagen fibril (intrafibrillar mineral, Figure 1.1 F) as well as surrounding it (extrafibrillar mineral) in different fractions, depending on the type of bones. [10], [21]–[23] The morphology of the mineral particles can be classified in four hierarchies: the thin (5 nm base), elongated (50–100 nm) and curved crystals aggregate laterally (width 20–30 nm) to form

the platelets often described in literature. Those morphologies can aggregate in order to form complex shapes for diverse purposes. [26], [27]

The chemical composition of bone apatite is far from the stoichiometric hydroxyapatite, as it is highly substituted with ions from the physiological fluids along with around 4–8 wt% carbonate. These substitutions can occur in any of its four crystallographic domains: the PO_4^{3-} tetrahedral positions, the Ca^{2+} (I) positions (phosphate surrounded hexagonal columns) or Ca^{2+} (II) positions (staggered triangular surrounding hydroxide) or in the OH^- "channel" positions. [14], [17], [28], [29]

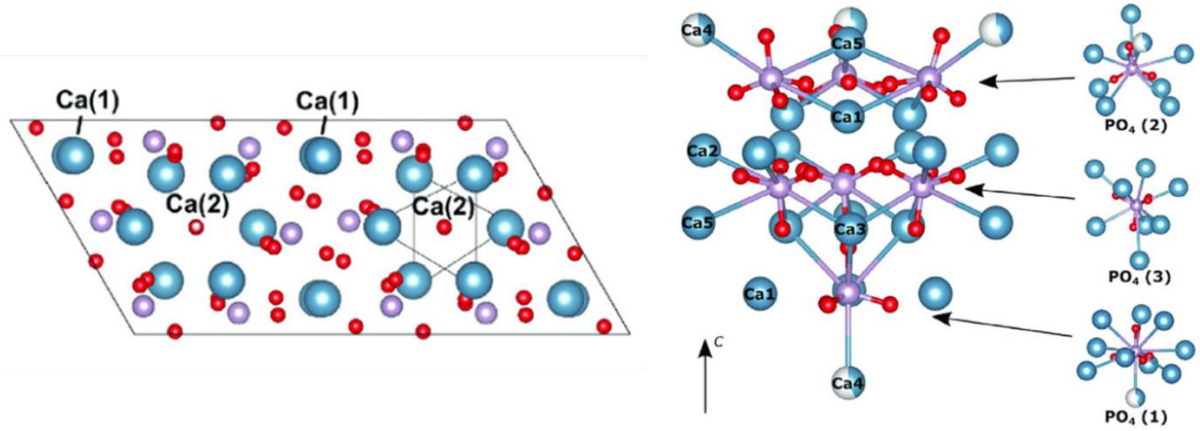

Figure 1.2 - HAp crystal molecular organization, at the left schematic representation, for two different Ca positions and at the right representation of the tricalcium phosphate (TCP) structure. Oxygen atoms are shown as small red balls, phosphorous as purple balls, calcium atoms as big blue balls. Adapted from [30]

In general, the composition of ion substitutes present are: CO_3^{2-} (around 5 wt%), Na^+ and Mg^{2+} (both between 0,5 and 1 wt%), K^+, Sr_2^+, Cl^-, F^- (up to 0,1%), and trace amounts of several other metallic elements: B, Al, Si, Ti, Cr, Mn, Fe, Co, Zn, Sr, Cd, La, and Pb. [10], [11], [27], [29], [31] These ions can aid the restriction of apatite crystal growth [32] and the stabilization of an amorphous calcium phosphate phase. [33]

The mineralized collagen fibrils bundle together in fibril arrays or fibers. Collagen fibers are arranged in parallel stacks.[15], [16] A lamella consists of typically parallel fibril arrays, but can be arranged in parallel stacks, with a slight angle offset, or alternating at sharp angles. [11], [34]–[36]

Osteons are the main structure of secondary bone and consists of a central canal (Haversian), occupied by a blood vessel and surrounded by concentric lamella (Figure 1.1). [11], [27] Canals perpendicular to the Haversian canal, the so-called Volkmann canal, link adjacent osteons. Lacunae resident osteocytes populate the bone surrounding the Haversian canal, with long axis concentric to the Haversian canal. Canaliculi extend from the lacunae, linking adjacent osteocytes to each other and to a filtering surface.[10], [12], [16] This lamellar structure is the center of spine fusion treatment, since it is where bone regeneration will occur with the osteoblast differentiation to osteocytes. [10], [11], [14] This structure is present cortical and trabecular bone. The cortical bone or compact bone is the major structure of the skeleton (around 80%) and forms the hard shell–like surface of a bone, while trabecular bone, also called cancellous or spongy bone, fills its core representing around 20% of the total skeleton with different proportions of cortical and trabecular bone at various locations in the skeleton. [9]–[12] The vertebral column, for example, consists predominately of trabecular bone. [11]

Compact bone is almost solid (≈6% porosity) with spaces only for osteocytes, canaliculi and blood vessels. In contrast, trabecular bone is 50 to 90% porous, making its modulus of elasticity and ultimate compressive strength as much as 10 times less than that of cortical bone (Table 1.1). Cancellous bone has a sponge-like morphology, with a honeycomb of branching bars, plates and rods of various sizes called trabeculae, which undergo constant remodeling (orientation and local density) for better functionality of the bone depending on the typical load applied. [9]–[11], [13] The pores in this sponge-like structure houses the bone marrow. [10], [11], [13]

Table 1.1 - Summary of the mechanical properties and porosity of human bone. [37]

	Compressive strength (MPa)	Flexural strength (MPa)	Tensile strength (MPa)	Elastic modulus (GPa)	Porosity (%)
Cortical bone	130–180	135– 193	50–151	12–18	5–13
Cancellous bone	4–12	NA	1–5	0,1–0,5	30–90

NA indicates data not available.

1.2 Bone Graft Substitutes

The increasing awareness of bone disorders resulted in the acceleration of investigation for bone grafting and bone regeneration. Bone-grafting materials can be divided into two main groups, based on the material source (e.g. natural and/or synthetic bone grafts).

Natural bone grafts can thus be divided in these three types: allografts, xenografts and autologous. [15], [38] Other materials used in allografts technique include the transplanted material from human cadavers and xenografts, obtain from animal bone. These organic materials present a problem with immunogenic reactions and risk of acquiring transmissible diseases, examples include: human immunodeficiency virus (HIV-1 and HIV-2), hepatitis B and C, syphilis and human T-cell lymphotropic virus (HTLV-1 and HTLV2) from tissues and fluids, as it has been recorded multiple times in the past. [6], [15], [39]–[41] To reduce these risks, allogeneic bone undergoes through alternative process techniques such as: lyophilization, irradiation or freeze-drying to remove all immunogenic proteins. These techniques consequently decrease their biological performance. [40]–[43]

In the autograft technique, bone from another part of the body (autologous) will be transplanted to fill the gaps providing optimal results and almost no risk of immunogenic response. The autograft presented properties such as Osteoinductivity (induction of differentiation of undifferentiated stem cells into osteoprogenitor cells); Osteoconductivity (migration of osteogenic host cells into the transplanted material) and Osteogenic (properties forming bone from the interior of transplanted material). These properties make autologous the current “gold standard” of care, for bone repair and regeneration of defects that do not heal spontaneously.[12], [15], [40], [42], [43]

In the spine case, Iliac crest autograft, obtained from the Gordy tubercle of the tibia, distal tibia, the proximal ulna and distal radius, is the most effective treatment for spine fusion as it provides both the osteogenic factor and scaffold necessary for fusion. [6], [15], [40] However, the failure rates are between 5% and 35%, the high mortality rate associated with complications in wound healing, additional surgeries, infections, prolonged wound drainage, sensory loss and chronic post-operative pain. On the other hand, it is an inadequate and there is a limited supply of bone for gap filling, with possible damage of lateral femoral cutaneous nerve, that may lead to paranesthesia and disturbances of gait. In addition some extreme rare complications may happen, including pelvic fracture, peritonitis and arterial injury. [6], [40], [44]

These facts led to the development of alternative bone graft options, including synthetic bone graft substitutes. These grafts try to mimic the mineral composition of bone tissue. These synthetic materials have the potential to perform as well as an autograft without it’s disadvantages for the patients, although there are still challenges of accomplish this at an affordable product cost .[15], [40]

Synthetic bone substitutes can be produced from metals, ceramics polymers or composites of previous groups. The metallic implants such as titanium and its alloys, stainless steel and cobalt-chromium alloys are used for load-bearing orthopedic applications because of their mechanical and morphological similarities with trabecular bone. However, it lacks tissue adherence, which may lead to additional surgeries, in order to remove bone implants, due to malfunctions, corrosion, or as a result of stress-shielding effect. Metallic implants also present a high risk of toxicity, by accumulation of metal corrosion ions due to acid pH and high surface area associated with porosity.[8], [42]

The ceramics, such as calcium phosphate, alumina, carbon and glass ceramics, are the major type of bone grafts substitutes available in the market, either alone or in combination with other materials because of their versatility and variety from different forms, porosities, pore sizes or topographies. An example of natural ceramics is coralline hydroxyapatite (HAp), while synthetic HAp, 45S5 bioactive glass (composition in wt%: 45 SiO_2, 24.5 Na_2O, 24.5 CaO and 6 P_2O), beta-tricalcium phosphate (β-

TCP) or alfa-tricalcium phosphate (α-TCP) are among the synthetic ceramics more commonly used. The most common combinations of ceramics are biphasic ceramics (BPC) mixtures of either β-TCP + HAp or α-TCP + HAp.[8], [42], [45], [46]

One of the major improvements in the ceramic materials for grafts applications, is the doping of the materials and structural modifications. The doping with Zinc proved to increase cell adhesion and proliferation [47]. Additionally better mechanical properties and biological response with co-doping of Zinc and Fluor.[48]

Out of the recently develop structures, the Mesoporous structure is the one with better improvement of both the biological response and the mechanical properties of the material. The biological response showed bioactivity due to their outstanding surface area values and porosity. The high efficiency in drug incorporation and releasability such as antibiotics, anticancer drugs or cytokines, confirmed bioactivity. [49], [50] The improved mechanical properties include higher resistance during the swelling and assays of simulated body fluids (SBF).[51]

This structure is obtained from the incorporation of surfactant agent to the sol–gel processes [51] or a surfactant catalyst in the micro-wave syntheses [52], as presented in Figure 1.3.

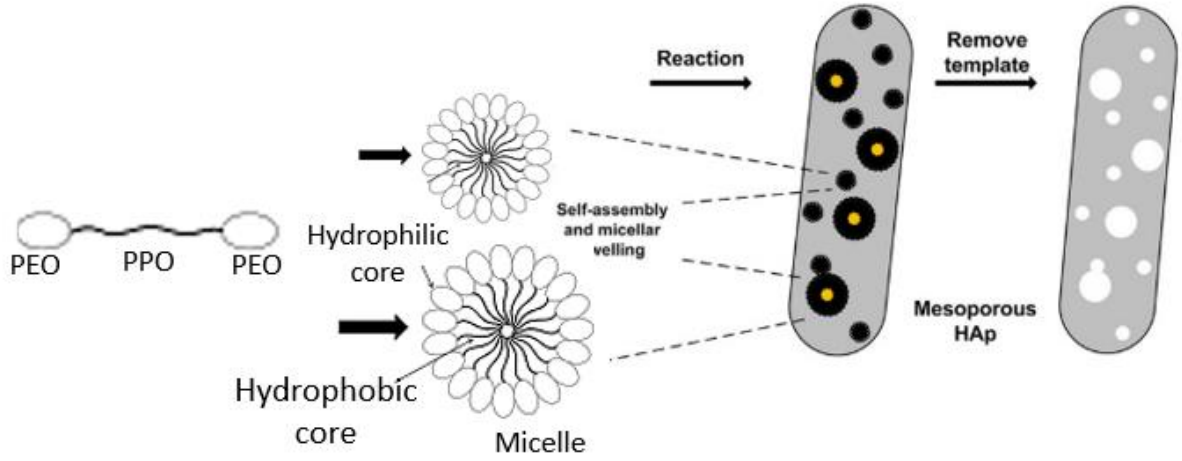

Figure 1.3 - Schematic of the syntheses of mesoporous particles. Adapted from [53] *and* [54].

Research in polymeric materials can be breakdown in two branches: the natural and synthetic polymers. The natural polymers such as collagen, fibrin, gelatin, starch, hyaluronic acid or chitosan, offer the advantages like good biocompatibility, bioactivity and biodegradability. Some of the natural polymers like chitosan, show antibacterial properties which prevent bacterial infection of the wound. [55] Those natural polymers are present in the structural native extracellular matrix of tissues and will contribute to a promising development of biomimetic biomaterials research, by using processes such as electrospinning and lyophilization, to create extracellular analogue matrixes.[8], [56], [57]

The Chitosan is composed of β (1→4)-linked 2-acetamido-2-deoxy-β-D-glucose (*N*-acetylglucosamine) and is obtained from the partial deacetylation of chitin. [58], [59] The degree of deacetylation (DD), crystallinity, and molecular weight (MW) are the main aspects in which chitosan can be modified to obtain different physical and mechanical properties. [58]–[60]

Chitosan consists of carbon (44.1%), hydrogen (6.84%), and nitrogen (7.97%), with a molecular weight in between 50 KDa and 2000 KDa and DD between 40 to 98%. Due to this properties chitosan has a strong hygroscopic nature. [58], [60]

The most used synthetic polymers are poly (methyl methacrylate) (PMMA), poly (urethane) (PUR) and poly- (α- hydroxy acids) such as poly-glycolic acid (PGA), poly-lactic acid (PLA), poly- (ε-caprolactone) and poly- (lactide-co-glycolide) (PLGA) a copolymer of PLA and PGA.[8], [42] These polymers provide

great versatility, as they can have different porosities, pore sizes, degradation rates, mechanical properties and poly-hydroxyethylmethacrylate (poly-HEMA), shown also osteoinductivity upon implantation.[8], [61] However, they also present disadvantages as inflammatory responses from high local concentration of acidic degradation products. This problem can be managed with ceramic addition which will reduce the polymer degradation. [62], [63]

Composites, such as calcium phosphate–ceramic coating on metallic implants and polymer–ceramic, in different material combinations can overcome same of the drawbacks as bone grafting materials, but in general the results discourage the apparent initial advantages.[42]

Table A. 1 presented in Appendix I, summarizes the different groups of bone substitutes: natural and synthetic biodegradable polymers, ceramics (including bioglasses), metals and composites.

So far, there is no ideal bone substitute that comprises all the properties of an autograft, namely: osteoconduction, osteoinduction and osteointegration (scaffold integration with the host bone [64], [65]).[8], [66]

The mechanism of osteoinduction by biomaterials is still under investigation, but several studies showed that biomaterials need to meet very specific requirements in terms of (a) macrostructure, (b) microstructure and (c) chemical composition in order to be osteoinductive. [9], [12], [66]–[68]

1.3 Market

In a quick market view, it's clear that biomaterial-based bone graft can substitute natural bone grafts in spine-fusion. In the UK it has showed that only 4 out of 59 commercially available products could perform equally or better than bone autograft.[6], [12], [15] Some of these products were Alpha-BSM (DePuy),[69] a resorbable calcium phosphate paste, Cortoss (Orthovia),[70] a non-resorbable bioactive glass cement, Vitoss (Orthovia),[71]–[74] a resorbable composite of calcium phosphate and collagen, and Norian SRS (Synthes),[75] a resorbable CaP cement, NanOss® 3D Plus™ (RTI Surgical),[76], [77] preformed strip composed of osteoconductive nanostructured hydroxyapatite, combined with an engineered extracellular matrix bio scaffold that mimics a natural bone growth solution. From all those products, only Vitoss and NanOss shown signs of osteoinduction, an essential property for successful bone regeneration and spine fusion.[74], [77]

It's also important to note that most of the products available are based on calcium phosphates, the exception being the bioglass cement (Cortoss™ or BIOGLASS C®), which has similar properties to CaPs possessing tunable degradability allowing direct contact with bone tissue. Despite the proven bioactivity, none of these materials can sustain loads by themselves and therefore are typically used in combination with metallic fixation apparatuses. [6], [66]

2 Materials and Methods

2.1 Materials

For the study of composite scaffolds two Chitosan types supplied by Bioceramed were used. One with low Molecular Weight (CHL) of 100 KDa with a Degree of Deacetylation (DD) of 80% and a second with high Molecular Weight (CHH) of 500 KDa with DD of 79.4%. For the polymer solution lactic acid was used 2-Hydroxypropanoic acid or $CH_3CH(OH)CO_2H$, purchased to HiMedia (minimum assay = 99.0%).

Bioceramed also supplied ForRegen (FR) (Lot:2015002), a biphasic powder with 75.2% w/w of HAp and 24.8% w/w of β tricalcium phosphate (β-TCP), particle size D50% = 2.18 µm and D90% = 10.51 µm.

In the MBG syntheses, Tetraethyl orthosilicate (TEOS), $Si(OC_2H_5)_4$, from Aldrich Chemistry (puriss. ≥ 99.0% (GC)), Triethyl phosphate (TEP), $PO(C_2H_5)_3$, from Fluka Analytical (puriss. ≥ 98.0% (GC)), calcium nitrate tetrahydrate ($Ca(NO_3)_2 \cdot 4H_2O$) from AnalaR NORMAPUR (puriss.≥ 99.0% (GC)), Pluronic F127 (F127), from Aldrich life Science and Ethanol from Sigma- Aldrich (puriss. ≥99.8% (GC)) were used.

For the MHap syntheses, calcium nitrate tetrahydrate ($Ca(NO_3)_2 \cdot 4H_2O$) from AnalaR NORMAPUR (puriss.≥ 99.0% (GC)), phosphoric pentoxide (P_2O_5,) from Sigma-Aldrich, F127 from Aldrich life Science and Ethanol from Sigma- Aldrich (puriss. ≥99.8% (GC)) were used.

For the neutralization it was used a solution of Sodium hydroxide (10% w/v) that was obtained by dissolving sodium hydroxide pellets in Ultrapure (Milli-Q).

For the Simulated Body Fluid (SBF) production several trademarks contribute. Merck: Sodium chloride (NaCl, J.T.Baker), Sodium bicarbonate ($NaHCO_3$); Aldrich: Potassium chloride (KCl, Scharlau), Potassium Hydrogen Phosphate Trihydrate ($K_2HPO_4 \cdot 3H_2O$); Roth: Magnesium Chloride Hexahydrate ($MgCl_2 \cdot 6H_2O$); Sigma-Aldrich HCl dilution of Hydrochloric acid (HCl); Honeywell: Calcium chloride ($CaCl_2$); Fluka: Sodium sulfate (Na_2SO_4); Apollo: Tris, or tris(hydroxymethyl) aminomethane $(CH_2OH)_3CNH_2$. Production of SBF was made according Kokubo's protocol.[78]

For the PBS, sodium chloride (NaCl, J.T.Baker), Potassium chloride (KCl, Scharlau), Hydrogen Phosphate (Na_2HPO_4, Sigma-Aldrich), Potassium dihydrogen phosphate (KH_2PO_4, Sigma-Aldrich) and HCl (Sigma-Aldrich) were used.

For all the dissolutions and cleaning of samples it was used Ultrapure Water (Milli-Q).

Human osteosarcoma cells (SaOS2 cell line), cultured in *McCoy's 5A* (Sigma-Aldrich) medium, were used for the cytotoxicity and adhesion tests. In both tests, population quantification was a result of the Resazurin (Alfa Aesar) reduction by viable cells. In the cytotoxicity tests, the positive control was obtained using dimethyl sulfoxide (DMSO). Helix NP™ Green nuclear stain from BioLegend was used for the cell fluorescence assay .

2.2 Synthesis

2.2.1 Sol-gel synthesis of MBG

The MBGs were synthesized by using a nonionic block copolymer PEO106 PPO70 PEO106 (F127), as surfactant agent (PEO is poly -ethylene oxide- and PPO is poly -propylene oxide-). A typical synthesis of MBG with molar ratio of Si/Ca/P=80:15:5 uses: TEOS (6.7 g), $Ca(NO_3)_2 \cdot 4H_2O$ (1.4 g), TEP (0.73 g), 1M HCl (0.5 g) and 21% of precursor mass in F127 (1.853 g), were dissolved in ethanol (60 g), stirred at room temperature and ambient conditions for one day. The resulting gel was introduced into a kiln at 60C˚ in order to evaporate the solvent and induce the self-assembly (EISA) process. [79]

The dried gel, was calcined at 700˚C for 5h with a ramp of 5˚C/min and placed in a ball mill for 6h to obtain the final MBG nanoparticles (NP).

2.2.2 Sol-gel synthesis of Hydroxyapatite

MHap powders were also synthesized by using F127 (1.96 g) and phosphoric pentoxide (P_2O_5, 1.44 g) and calcium nitrate tetrahydrate ($Ca(NO_3)_2 \cdot 4H_2O$, 7.88 g), used as precursors of phosphorous and calcium, respectively, in a molar ratio of Ca/P=10:6. Precursor solutions were obtained by dissolution

of the pentoxide and the nitrate in ethanol (30 mL). The precursor solutions and polymer solution were mixed at ambient conditions until the solutions appears clear. All the solutions were added and transferred to a heated silicone bath at a temperature of about 90˚C. After reaction, the obtained gel was dried at 80˚C for 24h in a kiln.

The dried gel was calcined at 400˚C and 700˚C for 1h at 5C˚/min to obtain a crystalline powder. This powder was grounded in a ball mill for 6h to obtain the MHap powders.

For comparison, nHAp was synthesized by an similar process but without surfactant. [80]

2.2.3 Preparation of nanocomposite scaffolds

2.2.3.1 Lyophilization

The composite scaffolds were fabricated by lyophilization of chitosan (CH) and CH/ceramic solutions. To produce the composite scaffold samples with different fractions of MHap, MBG, MHAp with MBG in a ratio of 1:1 (MC) and FR, the solutions present in Table 2.1 were prepared with a similar procedure as previously reported by [81]. CH solutions were obtained by dissolution of CH powder in lactic acid (2 % w/v) [62], The ceramics were ultrasonically dispersed (Ultrasonic processor UP400S from Heilscher) in an acid solution until all the clusters were disaggregated and then the CH was added while the solution was being agitated. Next, the composite dispersions were vigorously mixed using a magnetic stirrer for 2h to 3h to obtain a homogenous mixture without polymeric aggregates.

Table 2.1 - Composition in %w/w of the composite solutions used to produce the scaffolds.

Sample organization			**Sample name**	**Samples composition**				
Polymer	Ceramic			CHL (%w/w)	CHH (%w/w)	MHap (%w/w)	FR (%w/w)	MBG (%w/w)
CHL		0%	CHL	2	0	0	0	0
	MBG	25%	CHL + 25%MBG	2	0	0	0	0,5
		50%	CHL + 50%MBG	2	0	0	0	1
		75%	CHL + 75%MBG	2	0	0	0	1,5
	MHap	25%	CHL + 25%MHAp	2	0	0,5	0	0
		50%	CHL + 50%MHAp	2	0	1	0	0
		75%	CHL + 75%MHAp	2	0	1,5	0	0
	FR	25%	CHL + 25%MFR	2	0	0	0,5	0
		50%	CHL + 50%MFR	2	0	0	1	0
		75%	CHL + 75%MFR	2	0	0	1,5	0
	MC	25%	CHL + 25%MC	2	0	0,25	0	0,25
		50%	CHL + 50%MC	2	0	0,5	0	0,5
CHH		0%	CHH	0	2	0	0	0
	MBG	25%	CHH + 25%MBG	0	2	0	0	0,5
		50%	CHH + 50%MBG	0	2	0	0	1
		75%	CHH + 75%MBG	0	2	0	0	1,5
	MHap	25%	CHH + 25%MHAp	0	2	0,5	0	0
		50%	CHH + 50%MHAp	0	2	1	0	0
		75%	CHH + 75%MHAp	0	2	1,5	0	0
	FR	25%	CHH + 25%MFR	0	2	0	0,5	0
		50%	CHH + 50%MFR	0	2	0	1	0
		75%	CHH + 75%MFR	0	2	0	0,5	0

After obtaining the homogenous dispersions, the samples were transferred to Teflon tray with 11.8 cm^2 of area and 6 mm of height separations. To remove the air bubbles and level the CHL and CHH structures, the tray was kept in the freezer for approximately 16 hours. After the tray transference to *FreeZone Triad Cascade Benchtop Freeze Dryer* (Labconco, 7400030 model). Lyophilization was introduced at a step rhythm of 0.1mbar, as presented in Table 2.2 and Figure 2.1.[58]

Table 2.2 – Description of the Lyophilization cycles used to obtain the scaffolds. [58]

Program Cycles	Description
Pre-Freeze	The sample is frozen till -52°C and hold for 3h
Primary Drying	The sample is heated till -25°C at 2°C·min^{-1} and hold for 10h
Secondary Drying	The sample is heated till 17°C at 0.5°C·min^{-1} and hold for 10h

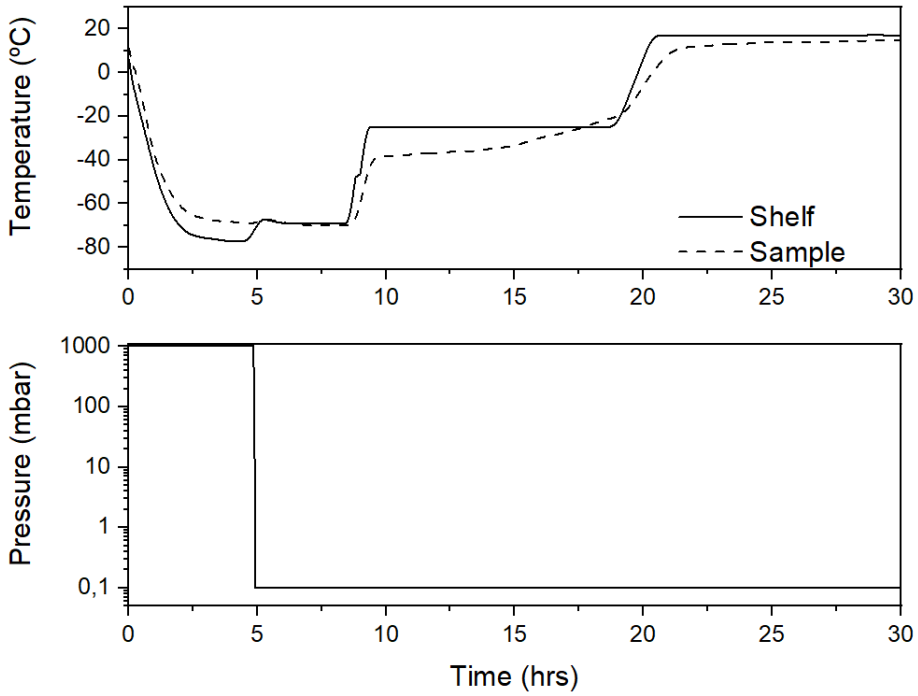

Figure 2.1 - Lyophilization parameters and samples temperatures during the process.

2.2.3.2 Neutralization

The resulting scaffolds still have lactate inside their structure and consequently the membranes dissolve when in contact with water. Therefore, in order to maintain the scaffolds integrity when implanted the lactate needs to be neutralized.

The neutralization process consisted of immersing the scaffolds in 10% w/v NaOH for 2 min, followed by 48h dialysis (until reaching a pH of around 7) and again lyophilized (VaCo 2 by Zirbus). [62]

2.3 Characterization

2.3.1 Microstructure and Morphology of NP and scaffolds

2.3.1.1 X-ray diffraction (XRD)

The X-ray diffractograms were used to determine the crystal phases of the different samples. These analyses were carried out at room temperature using a *X'Pert PRO PANAlytical X-ray* powder diffractometer (Cu K-alpha radiation) operating at a voltage of 45 kV. The process had an angle range of 10°–90° and the process parameters were: scan step size 0.033º (2 θ).

2.3.1.2 Transmission electron microscopy (TEM)

The morphology of the MBG, MHAp and nHAp particles was examined in TEM (JEOL JEM 1400), the samples were suspended in ethanol with a concentration of 1 mg/mL and dispersed on the sample holder. The Images were recorded using a SC ORIOUS CCO camera.

2.3.1.3 Nitrogen sorption porosimetry

Textural properties of the materials were determined by nitrogen sorption porosimetry, using a Gas porosimeter Micromeritics ASAP 2010 at 77 K. For this measurement, samples were previously degassed under vacuum for 10 h at 200°C.

The surface area was determined using the Brunauer–Emmett–Teller (BET) method and the pore size distribution, has been determined from the desorption branch of the isotherm by means of the Barret–Joyner–Halenda (BJH) method. The total pore volume was estimated from the amount adsorbed at a maximum relative pressure.

2.3.1.4 Porosimetry

The porosimetry of the membranes were calculated by the Archimedes method reported in [82]. Using Sartorius BP110 S balance and a 7 days PBS bath instead of an ethanol bath. This analysis used a three replica for each scaffold.

2.3.1.5 Scanning Electron Microscopy (SEM)

The morphology of the composite scaffolds was examined in a field emission SEM (Hitachi S-2700). The samples were frozen and broken in liquid nitrogen, mounted on aluminum platforms for horizontal/transversal view and sputter-coated with gold-palladium conductive layer (Q3000T D Quorum sputter coater). The images were taken with 15 kV and several magnifications.

2.3.2 Mechanical properties of scaffold

2.3.2.1 Compression modulus

The mechanical properties of the scaffold samples, were measured with a testing machine from Rheometric Scientific (Minimat Firmware version 3.1), equipped with a 100 N load cell, at a crosshead speed of 1 mm min^{-1} at room temperature and in compression mode. Prior to this test, the area and thickness of the ten scaffolds replicates were measured, to calculate the normalization of the curve and the standard deviation. [62], [83]

The compression modulus of the scaffolds was calculated by the slope of the stress–strain plot at 5 to 10% deformation range. [83]

2.3.3 Physicochemical properties

2.3.3.1 Fourier-transform infrared spectroscopy (FTIR)

Fourier Transform Infrared (FTIR) spectroscopy was performed over different materials, using a Thermo Nicolet 6700 spectrometer in a wave range of 4000–500 cm^{-1}.

2.3.3.2 Differential Thermal Analysis –Thermogravimetric analysis (DSC-TGA)

The thermal analysis of the HAp samples was conducted using a STA (*NETZSCH STA 449* ***F3*** Jupiter), in the Differential Scanning Calorimetry (DSC) and Thermogravimetry Analysis (TGA) mode. The samples were heated from 20˚C to 800˚C in nitrogen at a heating rate of 5˚C min^{-1} and a gas flow rate of 30 mL min^{-1}.

2.3.3.3 Swelling

The water uptake or swelling and retention abilities studies were performed in PBS at pH 7.4 at 37 °C with five replicates of each sample. With the dry weight (W_0) of the scaffold registered, scaffolds were placed in PBS buffer solution at pH 7.4 for 12h, 24h, 48h, 72h and 96h. The excess water adsorbed in the interior and surface, was removed with filter paper (Filter-Lab 1300/80) and wet weight (W_f) was recorded of the three replica.

Both these properties are determined by the following ratio:

$$E = \frac{W_f - W_0}{W_0} \times 100$$

Where W_f represents the final wet weight of the sample.

2.3.3.4 Degradation

Degradation of the composite scaffold was studied in PBS medium, with ionic force of 0.06 and 5 µg/mL of lysozyme from chicken egg white (Lysozyme BioChemica). [84], [85] The samples were immersed in the degradation solution and incubated at 37 °C in closed falcon tube for 7 and 14 days, with enzyme refreshing in 2 day periods. In the end of each predetermined interval to remove ions adsorbed on surface, the scaffolds were taken from the degradation medium and rinsed methodically with Milli-Q.

The biodegradation was quantified by the sample's variation of viscosity (HAAKE, MK 500) (six replicas for each time) and by weight loss in the three replicas (after a lyophilization as a drying process). [86] The quantification of the remaining weight is given by:

$$weight\ remaining\ (\%) = 100 - \frac{W_0 - W_f}{W_0} \times 100$$

The samples for viscosity were prepared dissolving the degraded scaffolds in a 1%w/v concentration with lactic acid. The measurement was performed with a shear stress rate of 1 min^{-1}.

2.3.3.5 Bioactivity

For the Bioactivity tests, the different samples were cut in squares of 0,5 cm edge and immersed in 30mL of SBF solution to guarantee the ratio $V_S = {}^{S_A}/_{10}$, where V_S is the volume of SBF in mL and S_A is the samples apparent surface area in mm^2. The samples were incubated at 37 °C in closed falcon tube for 3, 6, 12, 24, 48, 72 hours and also for 7 days with two replicas of each analysis. [78] After the specified periods to remove non adsorbed minerals, scaffolds were washed five times with Milli-Q. Then in order to identify and analyze if the samples have an apatite precipitation, the scaffolds were dried at ambient conditions, viewed using SEM.[78], [87]

2.3.4 Cell culture studies Cell

2.3.4.1 Cytotoxicity

The cytotoxicity tests were performed according to the ISO 10993-5 standard using the extract method. Samples were sterilized with ethanol and irradiated with UV for 2 hours and then 2 extra hours at 80˚C, to guarantee the ethanol evaporation. For extract preparation, the scaffolds were immersed in McCoy's culture medium with a ratio of 25 mg/mL (mass of sample/volume of culture medium). These preparations, as well as some extra medium for the extract dilution and the negative control, were incubated at 37˚C in a controlled 5% CO_2 atmosphere for 48h.

The Saos-2 cells were seeded at a concentration of 30 k cells/cm^2, on the wells and incubated for 24h. Then, the medium was exchanged for the extract and 2 dilutions (12,5 mg/mL and 6,25 mg/mL) made, each with 4 replicates. For the Resazurin test it was set a negative control (cells cultured in a standard, non-cytotoxic environment) and a positive control (cells in a cytotoxic environment, created through the addition of 10 µL of DMSO, a cytotoxic agent, to normal culture medium). [58]

The extracts and controls were incubated for 48h following the ISO 10993-5 regulation. After 48h, the media were switched for a 1:1 solution of Resazurin and McCoy's medium including extra wells for this solution control and incubated for 3h. The cell activity was evaluated by measuring the absorbance of the medium at 570 nm and 600 nm in a microplate reader (Biotek ELx 800UV). [88]

2.3.4.2 Cell Adhesion

The ability of the scaffolds to support cell metabolism, was evaluated through cell adhesion and proliferation studies. [25], [89] The scaffolds were sterilized the same it was as done for the cytotoxic tests. Then the materials for the cell culture and material controls, were fixed in a Teflon support in the 24 wells plate.

The Saos-2 were seeded at a concentration of 30 k cells/cm^2 directly over the sample surface and for the cell control on the well. The cells were maintained in McCoy's medium and incubated 37˚C in a controlled 5% CO_2 atmosphere for 24h. [25], [89]

The cell adhesion rate was determined by evaluating the reduction of Resazurin to Resorufin by metabolically active cells. For this process the medium was substituted by 1:1 solution of Resazurin /McCoy's medium and incubated for 4h. The medium and McCoy's control (both wells without cells) were also incubated. The cell activity was evaluated by measuring the absorbance of the medium at

570 nm (absorption maximum of Resorufin) and 600 nm (absorption maximum of Resazurin) in a microplate reader (Biotek ELx 800UV). [88] The Resazurin assay was repeated at 3, 6, 8 and 10 days for evaluation of the cell proliferation for each of the six replicas of all the materials.

After the last readings, the materials were removed from the multi well plate, washed with PBS and fixed with a 3.7% paraformaldehyde solution, incubated at room temperature for 15 min. Then, the samples were washed with water and stained with Helix NP^{TM} Green and observed through fluorescence microscopy.[90]

2.3.5 Statistical treatment

All average values calculated and displayed in the graphics, include a representation of standard deviation with a segment.

The calculation of the standard deviation used in the laboratorial data processing, was the sample standard deviation.

3 Results and Discussion

The results presentation and discussion will be divided in two stages. In the first stage it will be analyzed the raw materials used in the composite scaffolds and in a second stage the produced membranes are studied and analyzed.

3.1 Raw Materials Analyses

3.1.1 Physicochemical properties

3.1.1.1 FTIR

A FTIR spectroscopy was used to analyze the powders of the scaffolds and, later on to verify the presence of the materials in the pretended composite scaffolds.

3.1.1.1.1 HAp

The FTIR analyses on the HAp is used to identify the temperature where HAp formation happens and if the addition of F127 alters the final chemical composition of the sample. The FTIR analysis is presented in Figure 3.1, where graphic A shows nHAp and graphic B the MHap. Each of the samples is analyzed in the amorphous state (no sintering), sintered at 400°C and 700°C.

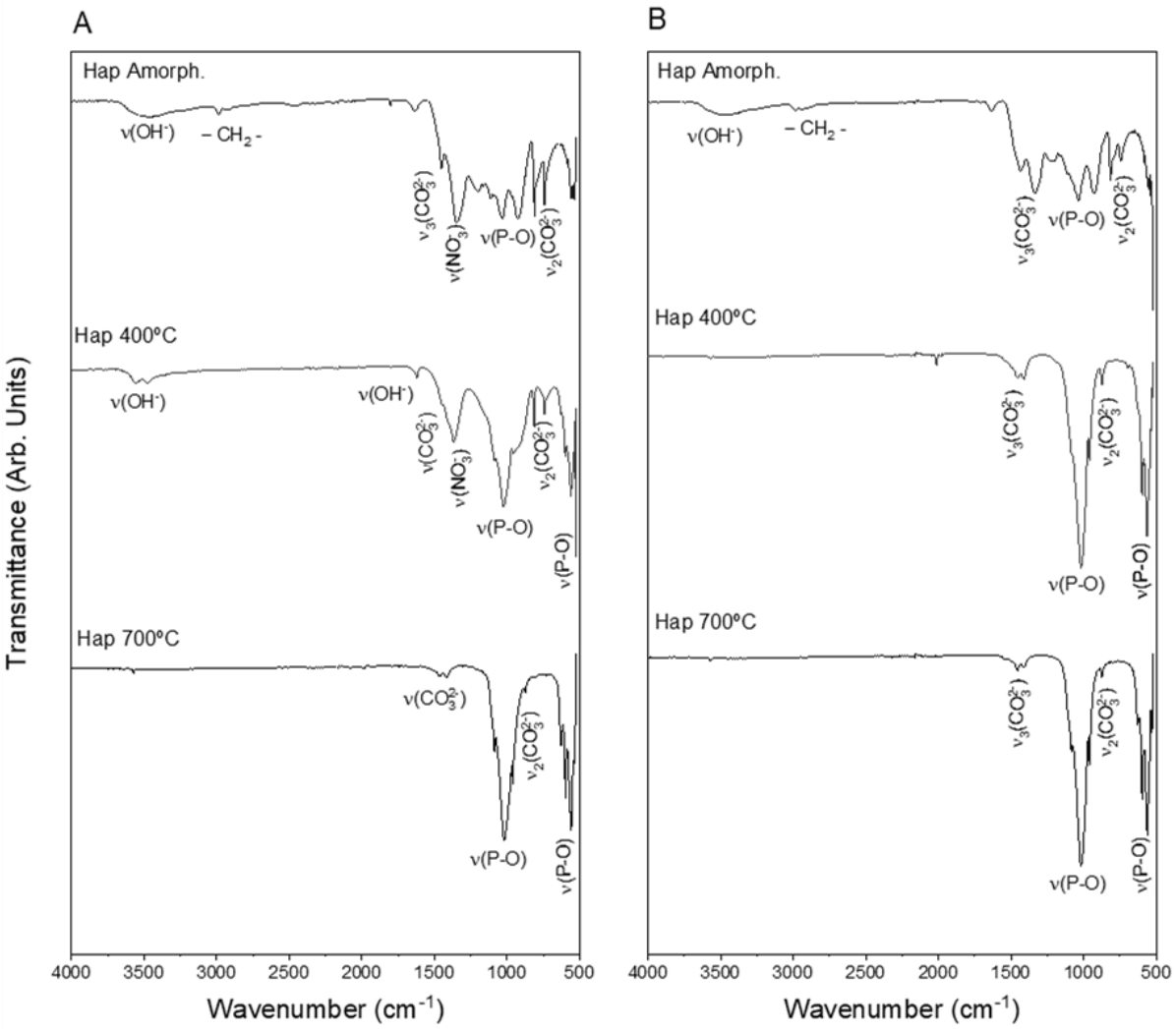

Figure 3.1 - FTIR of nHAp (A) and MHAp (B)

The amorphous MHap and HAp shows the organic bonds in the range of 3556 cm^{-1} to 2989 cm^{-1}, 1626 cm^{-1} and around 2956 cm^{-1}. HAp first bands represent the presence of adsorbed water in the stretching vibration modes of hydroxyl groups and the bending mode of H–O–H molecules, respectively. The last represents the -CH_2- bending and stretching vibrations of the PEO in the F127 surfactant. [91]–[93]

The FTIR spectra shows the inorganic carbon ions (CO_3^{2-}) in both sintered and no sintered samples. These bands are located at 1456 cm^{-1} to 1414 cm^{-1} and from 742 cm^{-1} to 879 cm^{-1}, both a result of asymmetric bending mode of CO_3^{2-}. [90], [94] Both bands decreases in intensity during the synthetization process and at the ends of the process (700ºC for the nHAp and from 400ºC in the MHAp) it's weak peak almost totally masked with the PO_4^{3-} bands. [90]

In the non-sintered samples, the FTIR analysis presented a band at 1350 cm^{-1} from the NO_3^- which disappears during synthetization at high temperatures (700ºC). [94]

The first indication of the formation of HAp is the formation of a broad bands centered at 1115 cm^{-1}, 1020 cm^{-1}, in the range of 925 cm^{-1} to 960 cm^{-1} and at 580 cm^{-1}. The first bands correspond to P-O vibrating bonds of the phosphate groups in the asymmetric stretching mode, the third a symmetric stretching mode of the ion and the least to the asymmetric bending mode PO_4^{3-}. [25], [62], [90], [93], [94]

The described bands are summarized in Appendix II Table A. 2.

The FR FTIR spectra is presented in Appendix II, Figure A. 1. This material just shows two bands already described above for the P-O vibrating bonds of the phosphate groups in the asymmetric stretching mode and to PO_4^{3-} asymmetric bending mode. [95]

3.1.1.1.2 MBG

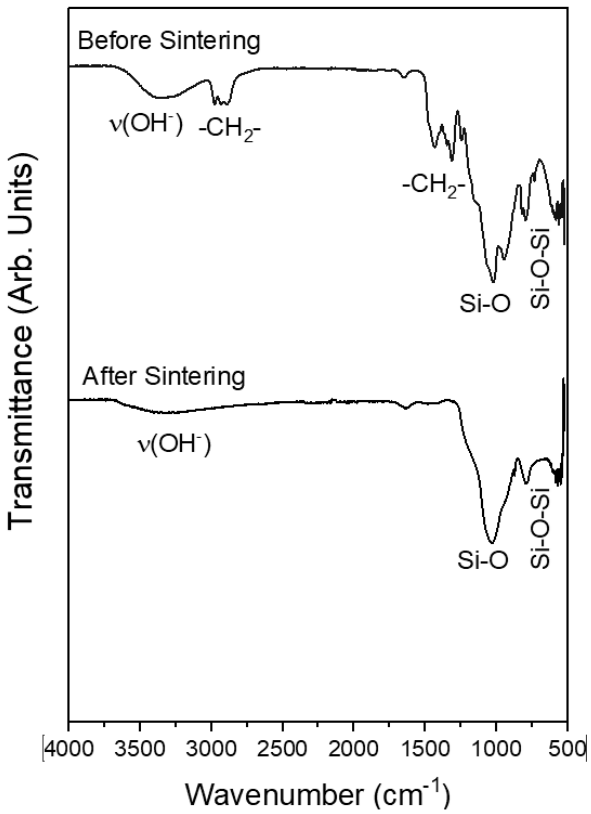

Figure 3.2 -FTIR of MBG before and after sintering at 700˚C.

The FTIR spectra in Figure 3.2 shows MBG before and after the sintering process at 700°C.

The amorphous MBG still shows the organic bonds in the 3375 cm^{-1}, 2983 cm^{-1} to 2880 cm^{-1} and 1433 cm^{-1} to 1246 cm^{-1} ranges. The first band is the O-H stretching vibration mode on the adsorbed in material surface. [96] The other two organic bands represent the -CH_2- bending and stretching vibrations of the PEO in the F127 surfactant. With the sintering process at 700°C those organic bands almost completely disappear. [91]

The rest of the bands represents the structural MBG bonds. The bands at 1150 cm^{-1}, the range of 820 cm^{-1} to 780 cm^{-1} and 569 cm^{-1} corresponds to the Si–O–Si asymmetric stretching, symmetric

stretching or vibration modes and bending mode, respectively. The Si–O bond with the Q^2 and Q^3 units can be seen at 1032 cm^{-1} and the Q^1 and Q^2 units at 947 cm^{-1}. [51], [97]

The described bands are summarized in Appendix II, Table A. 3.

3.1.1.1.3 CH

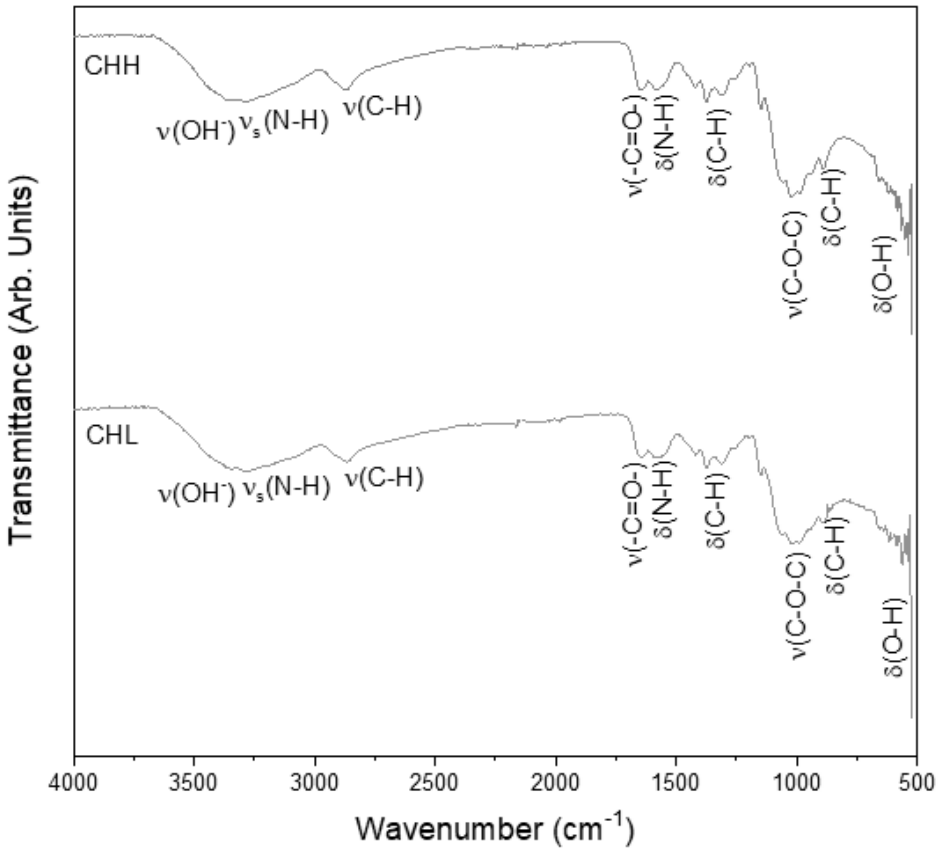

Figure 3.3 - FTIR of CHH and CHL.

In the FTIR spectra presented in Figure 3.3, the bands of the functional groups present in the CHH and CHL are shown. These bands are also summarized in Appendix II, Table A. 4.

The broad band in the range of 3270 to 3365 cm^{-1} represents the overlap of N-H (3280 cm^{-1}) and O-H (3358 cm^{-1}) stretching vibration. This band also is attributed to the polymeric intramolecular hydrogen bonds. The band around 2867 cm^{-1} and 2921 cm^{-1} corresponds to asymmetric and symmetric stretching mode of C-H of CH_2, respectively. The symmetric stretching is present in both FTIR spectra but with less intensity than the asymmetric stretching, so it is partially hidden with the overlapping of the bands. [58], [98], [99]

The band around 1645 cm^{-1} shows the C=O stretching of amide I from the residual presence of N-acetyl groups. The 1311 cm^{-1} band is for the N-H bending of amide II. This group usually have one more band at 1550 $cm^{-1}$for the C-N stretching of the amide III, which also were hidden by other bands. [62], [98], [100]

The band 1581 cm^{-1} represents the N-H bending of the primary amine. The absorption signal at 1423 and 1372 cm^{-1} is attributed to all hydro carbonates bonds, CH_2 bending and CH_3 symmetrical deformations. [98]

The stretching of the C-O-C bridge is present in the wave number of 1149 cm^{-1} and in the 1065 to 1016 cm^{-1} range, respectively to an asymmetric stretching and a simultaneous symmetric and asymmetric stretching vibration of the ester bond. [62], [100], [101]

The CH out of the plane bending of the ring of monosaccharides is visible by the band at 896 cm^{1}. The band around 650 cm^{-1} represents the bending deformation of O–H on the polymeric structure. [62], [98]

3.1.1.2 DSC-TGA

The thermal behavior of nHAp and MHAp was studied, by differential scanning calorimetry (DSC) and thermogravimetry (TGA) analysis. This analysis allows the identification of the sintering temperature, F127 elimination from the ceramic structure and optimization of MHap the process temperature.

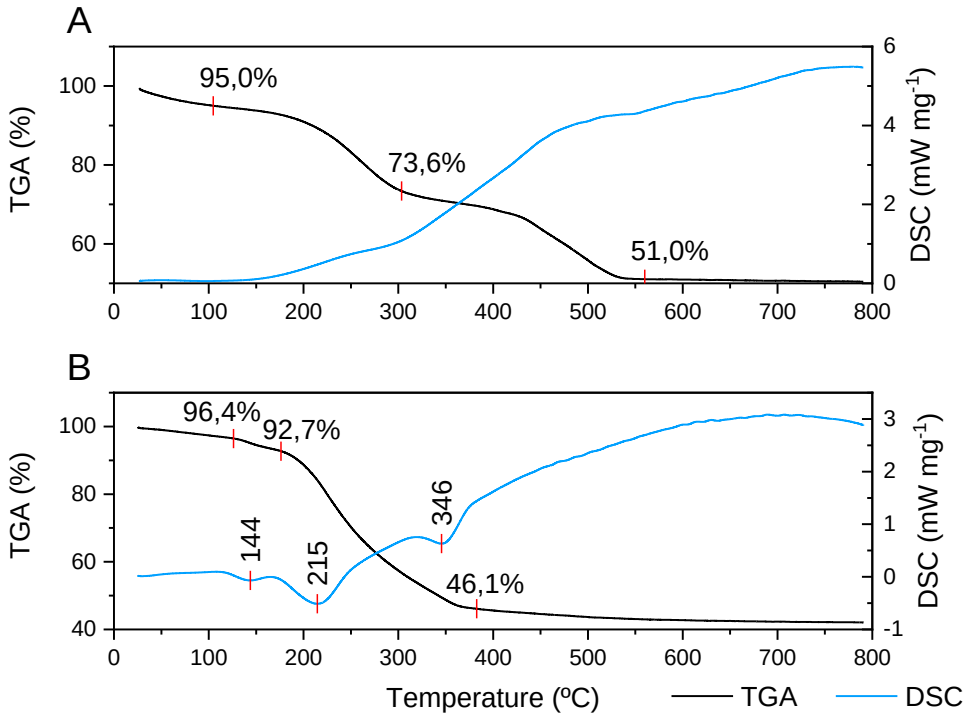

Figure 3.4 - DSC/TGA of A) nHAp and B) MHAp

The first mass loss in both TGA curves (nHAp and MHAp) is around of 5% at 125°C, along with a slight endothermic peak in DSC curve. This loss is due to evaporation of physical water adsorbed, lattice water result of dehydration of the structure and ethanol residues from the reaction.[25], [102], [103]

In the nHAp there were two rapid weight loss from 200˚C to 300˚C of 22.17% and from 400°C to 550°C of 22%. The first weight loss is a result of thermal decomposition of organic macromolecules and the second, is an indicator of precursor decomposition reactions ($Ca(NO_3)_2.4H_2O$). [25], [103], [104] It's also important to mention the exothermic peak in DSC curve at 550˚C, which may be assigned to the transformation of the amorphous structure, into an organized crystalline phase without significant mass loss. [103]

The last segments of nHAp, TGA curve correspond to a small mass lost after 550°C due to decarbonation (1%) and a straight region without mass variations (700°C-800°C). The last segment shows the HAp thermal stability. [102]

The MHAp DSC curve have three exothermic peaks, at 144˚C, 215˚C and 346˚C. The peaks at a lower temperature are a result of structural alterations due to thermal decomposition of block copolymer templates. The peak at 346˚C is most likely from the precursor, surfactant copolymers decomposition reactions and crystallization temperature. [79], [103] The TGA also shows an almost straight region of thermal stability (600°C-800°C).

The DSC-TGA analysis showed that the MHAp sample crystalized at lower temperatures revealing a different structure from nHAp since the XRD and FTIR analysis presented the same results meaning that the two samples have the same chemical composition however with different structural organizations. From the STA is also possible to identify the sintering temperature for the MHAp and nHAp powders. The MHAp can be sintered at 500˚C and the nHAp need to be sintered at temperatures at least around 600˚C in order to be fully crystalized.

3.1.2 Microstructure of the raw materials

In this chapter the raw materials used on the membranes will be analyzed based on their crystallography (XRD and TEM), size (TEM) and porosity (Nitrogen sorption porosimetry).

3.1.2.1 XRD

In order to determine the level of crystallinity and crystalline phase of each used material, all the raw materials used in the scaffolds were analyzed by XRD.

3.1.2.1.1 MHap analysis

The study of crystallization and crystallographic organization during the syntheses of MHAp with the addition of F127 in the Sol-Gel method was not previously analyzed. However, it's important to analyze the crystallization temperature and organization of the used materials, so with this purpose is represented in Figure 3.5 the crystallography analyses, comparing MHAp to nHAp in different stages (no sintering and with sintering at 400ºC and 700ºC).

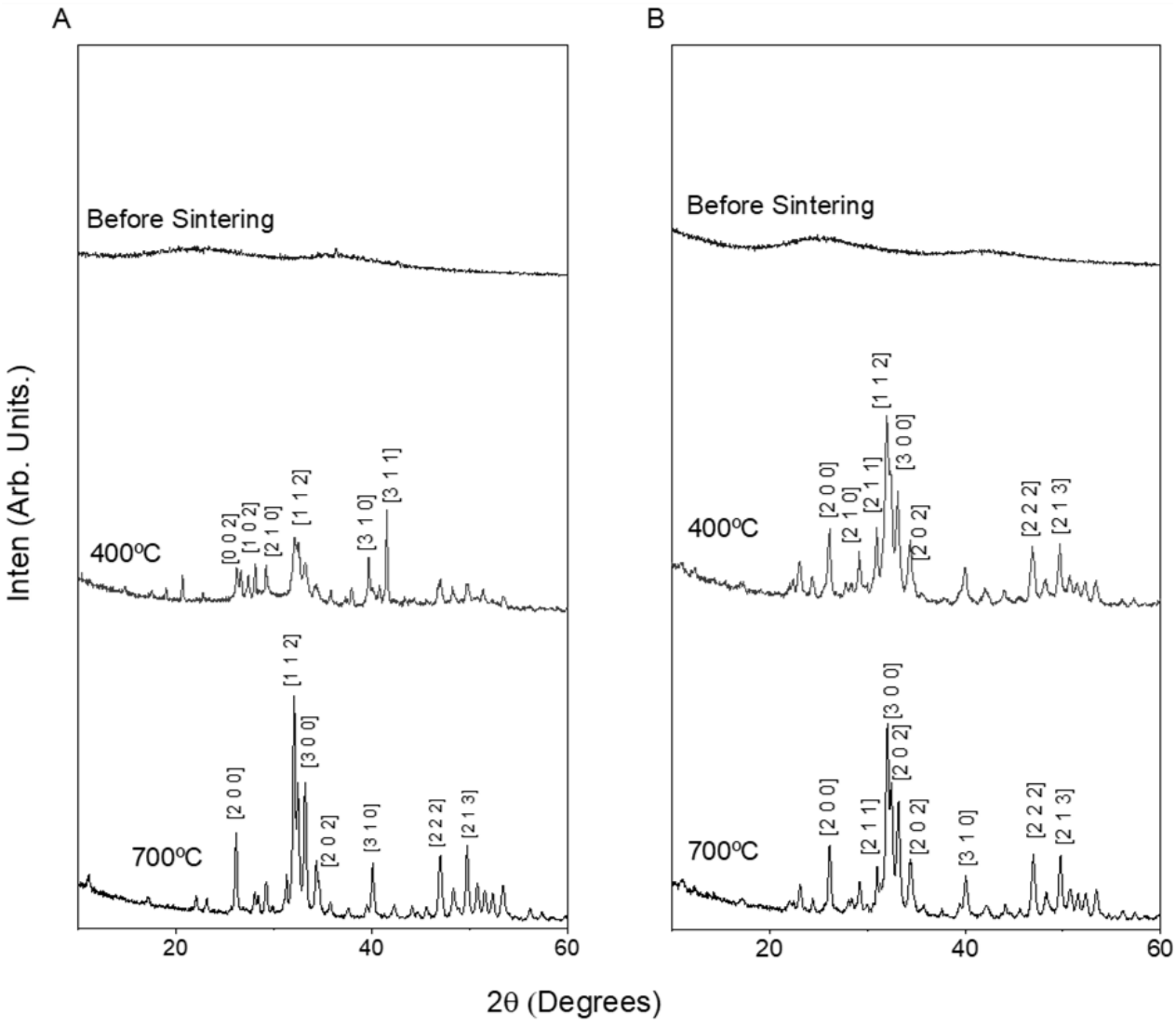

Figure 3.5 - XRD diffractograms of nHAp (A) and MHAp (B) with no sintering and 1h of sintering at 400˚C and 700˚C.

At 400˚C the materials present a different degree of crystallization. The MHap shows an almost completely crystalized structure with defined peaks similar to the diffractogram at 700˚C. In the nHAp sample at 400˚C the crystallization is just beginning. This process is showed with the presence of broader and of less intensity than the XRD diffractogram at 700˚C. So, the MHap crystallizes at lower temperature.

At 700˚C both materials present a crystallized structure with the typical HAp peaks. [105]

In Figure 3.6 the XRD diffractograms of the synthetized ceramics (graphic A) and the used polymers (graphic B) are presented.

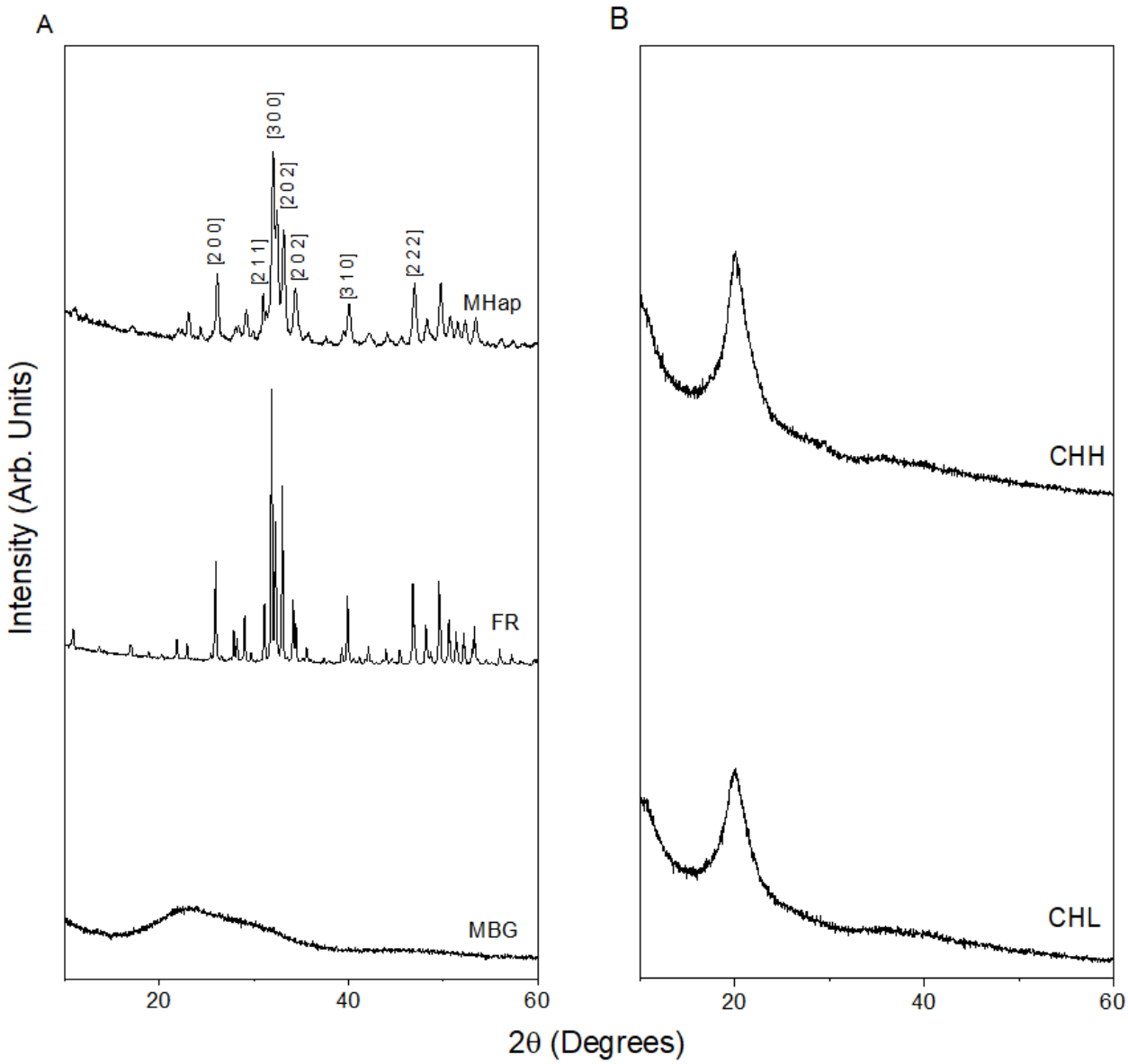

Figure 3.6 - XRD of the ceramic (A) and the polymeric (B) materials.

The HAp particles used in this study (MHAp and FR) presented the major peaks for the HAp and the FR diffractogram the major peaks for the HAp and the β-TCP phases.

The MBG sample only present a broad peak at 30º since this material it's totally amorphous. The polymeric samples present a broad peak at 20º meaning that the used chitosan have a slightly crystalline structure.

3.1.2.2 TEM

TEM images enables the study of NP structure and crystallographic organization. The MBG in Figure 3.7 (image A and B) and HAp in Figure 3.8 (image A for nHAp and image B for MHAp) allows to analyze related morphology and structure.

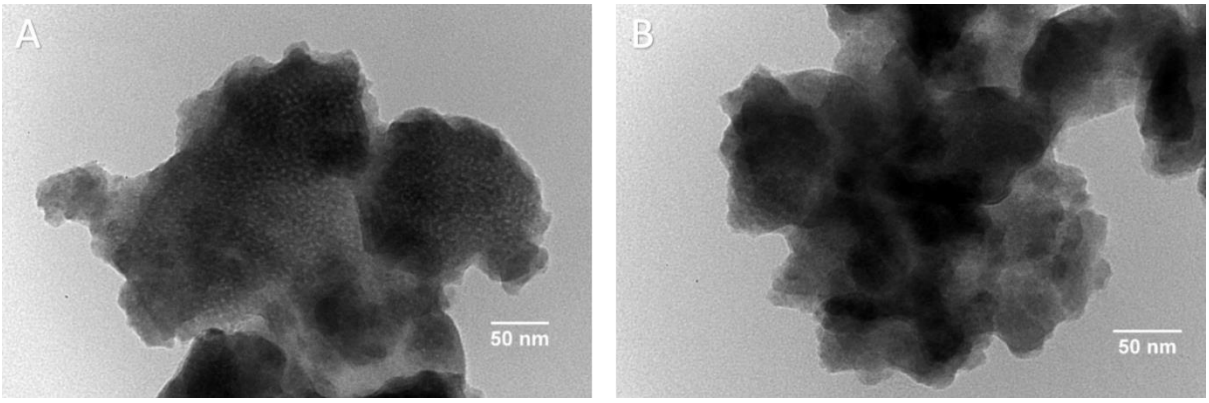

Figure 3.7 - TEM images of MBG nanoparticles.

The MBG NP showed in Figure 3.7 presents a pattern typical of a mesoporous structure composed exclusively of poorly ordered wormlike aggregates with numerous individual mesoporous (white nanodot). This structure is formed when the surfactant concentration exceeds the critical micelle concentration during the ethanol evaporation, beyond the critical concentration, micelles are formed and occurs co-assembly of silica-surfactant micellar species (Figure 1.3). This process results in disordered cylindrical micelles. [106], [107]

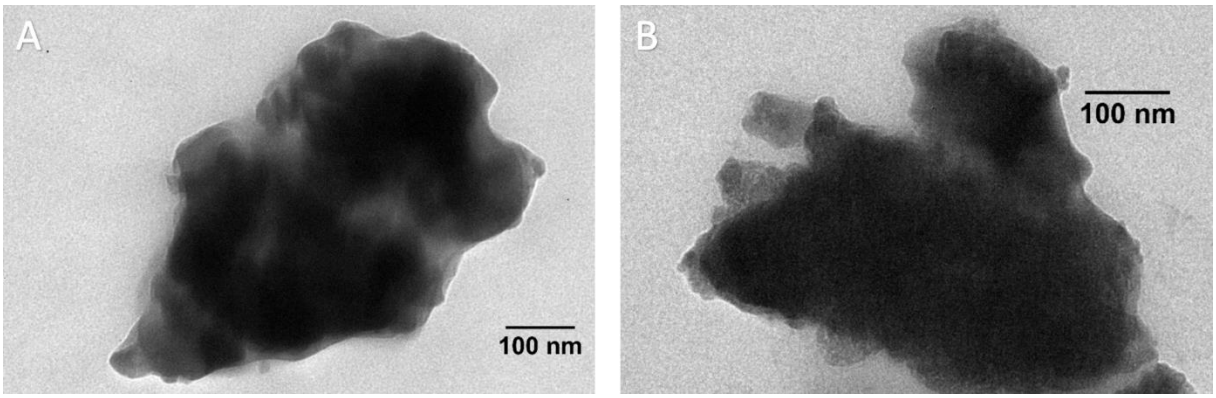

Figure 3.8 - TEM images of nHAp (A) and MHAp (B) nanoparticles.

The HAp samples seem to present a similar structure to the MBG samples. However, to assure it, is necessary to have higher magnification and Fourier transform patterns. [53], [106]

3.1.2.3 Nitrogen sorption porosimetry

The obtained nitrogen sorption porosimetry curve, used the Barrett– Emmett–Teller (BET) method to calculate the specific surface areas and the Barrett–Joyner–Halanda (BJH) method to derive the adsorption branches of the isotherms, calculate the pore volume and the mean pore size. The total pore volume was obtained from the extent of adsorbed nitrogen at a maximum relative pressure. The resulting values are presented in Table 3.1.

Table 3.1 - Physicochemical properties of MBG, nHAp and MHAp.

	surface area (m^2/g)	**pore volumes (cm^3/g)**	**pore sizes (nm)**
MBG	223.5	0.19	3.5
nHAp	12.5	0.08	26.4
MHAp	19.9	0.11	21.4

The MBG presented lower surface area (224 m^2/g) than previous studies with F123 in 80S15C composition (351 m^2/g) [79], [103], [108]. This fact could be attributed to the use of F127 surfactant at low concentrations, which already showed a decrease of surface area on 70S25S. [79] However the orders of magnitude are similar. The pore volumes (0.19 cm^3/g) was also lower than the previously reported values (0.49 cm^3/g) [79], [103], [108], this fact could be due to the surfactant type, related

surfactant concentration and oven calibration. The conjugation of these factors could be responsible for the reduction of 61% in pore volume. In [79] study the F127 has reduced the pore volume by 20% and in [108] study the oven was offset by plus 100ºC calcination temperature, resulting a reduced pore volume by 59%. However, the surfactant concentration is the major factor for reduction of pore volume, so polymers lower concentration result in smaller micelles and create smaller templates for material precipitation.

In the HAp study, the introduction of F127 surfactant increased the surface area, increased pore volumes and reduced the pores size, it's the expected behavior, based on the introduction of F127 in the bioglass syntheses reported by X. X. Yan *et al.* [103]. The obtained values for pore volume and pore size in the nHAp sample are similar to previously reported values (0.1 m^3/g and 27 m^3/g, respectively) [54], however the surface area was inferior than reported values (23 m^2/g) this fact could be a consequence of having bigger NP and therefore lower surface area. [109]

The obtained nitrogen sorption porosimetry results for the MHAp sample confirms the presence of a mesoporous structure verifying the proposed hypotheses in Figure 3.8.

3.1.3 Cytotoxicity

Cell response to the materials was tested using Resazurin as a metabolic indicator. Resazurin is a blue colorant that is reduced by metabolically active cells. Upon reduction, Resazurin changes to Resorufin, which presents a pink color and high fluorescence. This conversion is quantified by measuring the absorbance at 570 nm and 600 nm. Relative cell viability of the tested sample is obtained by comparing with the negative control absorbance.[110]

If the relative cell viability for the highest concentration of the sample extract (100% extract) is equal or superior than 70% of the control group, then the material shall be considered non-cytotoxic. [110]

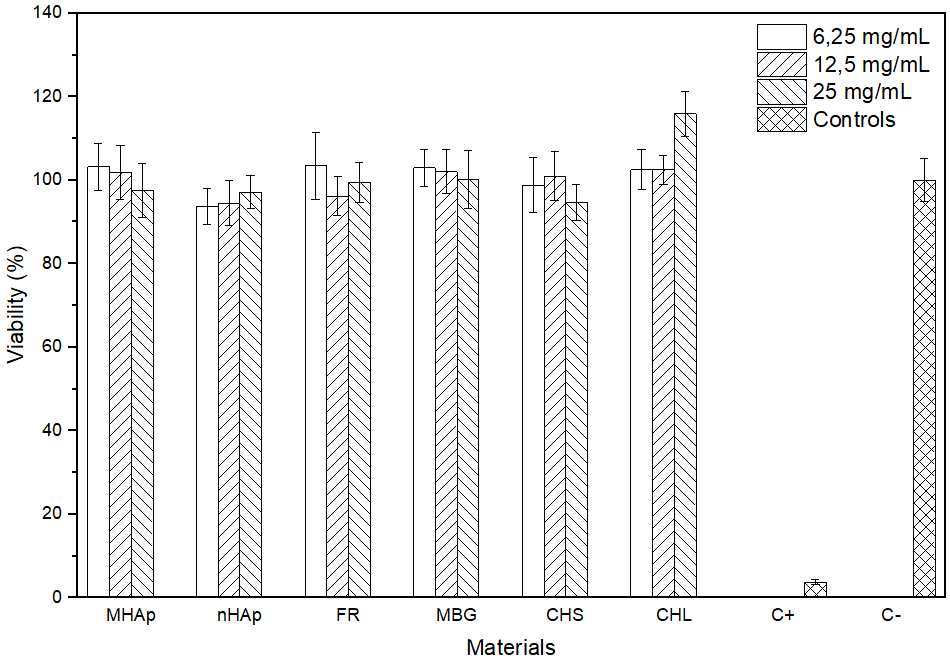

Figure 3.9 - Cell viability in response of the scaffold's base materials cytotoxicity. Data obtained from a sample of four replicas for each scaffold.

The cytotoxicity assay of the polymeric and ceramic materials presented in Figure 3.9 showed that for all the materials and extract concentrations tested, relative cell viability is higher than 90%, in comparison of these results with the negative control, and therefore the materials are cytocompatibility. These results were expected because all the tested materials, with the exception of MHAp, had already been tested in previous works and are part of the composition of clinically available products. [58], [89], [90], [111].

These results suggest that all tested materials are safe to be used in the composite scaffolds. [110]

3.2 Membranes analysis

3.2.1 Structural and Morphology Analysis

3.2.1.1 XRD

The XRD diffractograms of the polymeric membranes are presented in Figure A. 13, graphic A and the composite scaffolds are presented in Figure A. 14 for the FR composites, Figure A. 15 for the MHAp, Figure A. 16 for the MBG and Figure A. 13, graphic B for the mesoporous composite . In Figure 3.21 the diffractograms of higher ceramic concentration scaffolds are presented, where the CHL membranes are in graphic A and CHH in graphic B.

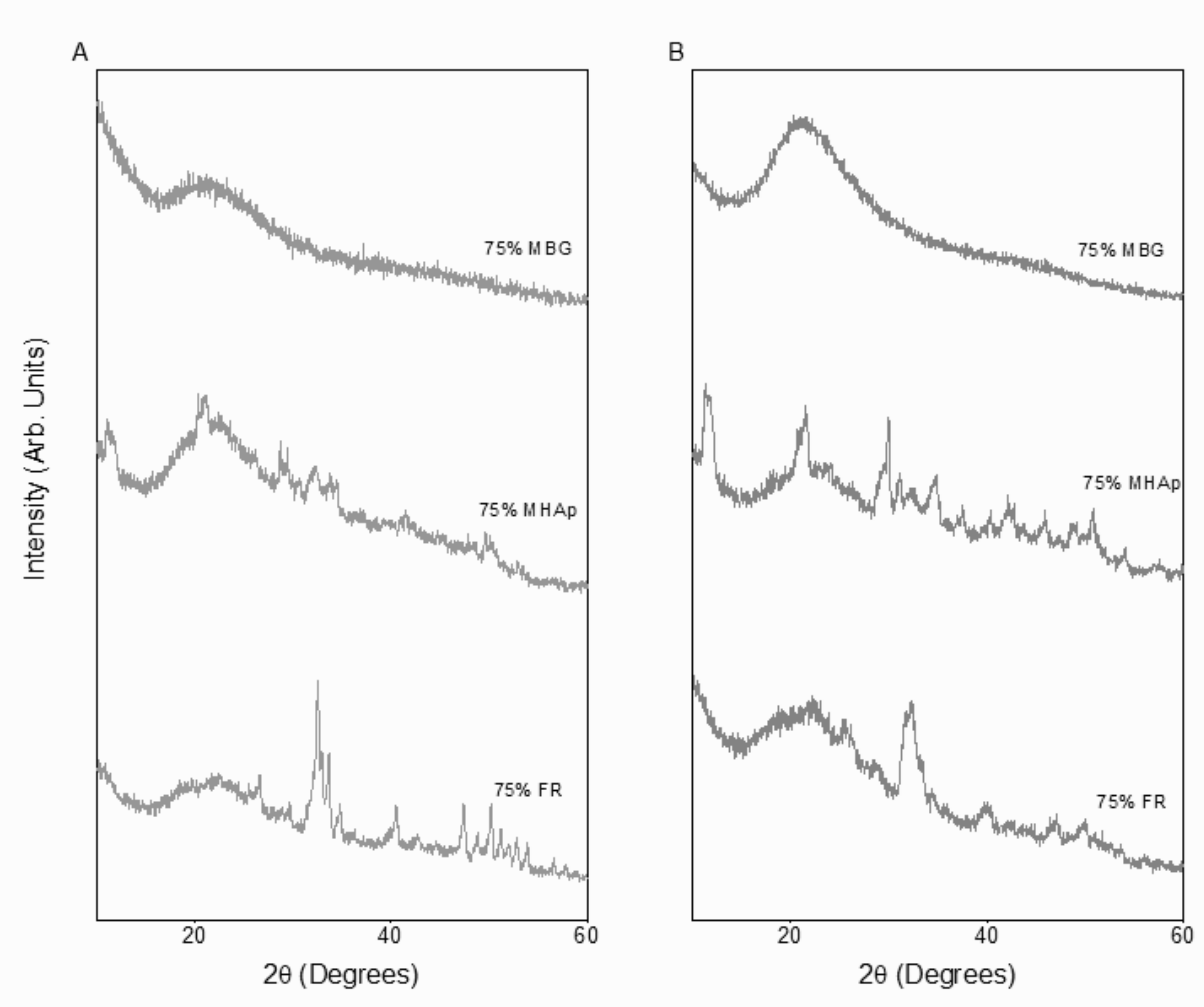

Figure 3.10 - XRD diffractograms of composite membranes with CHL (A) and CHH (B) with different ceramics.

All the composite membranes with MBG just presented a peak approximately at 20°. This peak is attributed to chitosan present in the sample and already tested in raw material (Figure 3.6, graphic B) and in membrane (Figure A. 16). The absence of any new diffraction peak confirmed that during the membrane production and treatment the MBG maintained an amorphous state as the initial synthetized material (Figure 3.6, graphic A). [87]

The composite membranes with MHAp and FR only present the broad peak of chitosan since the intensity of the chitosan signal is higher than the ceramic. However, with the increase of ceramic concentration the main peaks of these materials begin to appear.

3.2.1.2 Porosimetry

The major parameters of a scaffold for tissue engineering is the pore size, porosity and surface area. [112], [113] These parameters have direct implications on the scaffold's functionality during biomedical applications, such as allowing the transport for tissue vascularization, cell adhesion, proliferation and migration. [67], [112], [113] For these reasons it's important to test the porosimetry of the produced scaffolds. The obtained results are presented in Table 3.2.

Table 3.2 - Porosimetry results of the produced samples (data obtained of three replicas for each scaffold).

		CHL	CHH
Ceramics	0%	93% ± 2%	95% ± 2%
FR	25%	89% ± 3%	89% ± 1%
	50%	85% ± 5%	90% ± 5%
	75%	84% ± 3%	81% ± 3%
MHAp	25%	90% ± 1%	89% ± 3%
	50%	85% ± 2%	84% ± 2%
	75%	89% ± 3%	87% ± 2%
MBG	25%	91% ± 2%	91% ± 4%
	50%	90% ± 1%	87% ± 2%
	75%	95% ± 2%	90% ± 1%
MC	25%	94% ± 3%	
	50%	90% ± 1%	

All values are between 80% and 90% of porosity. The polymeric membranes present a lower porosity than the previous works with the similar polymer and same freeze dryer [58] but this could be due to the contraction of the membranes after the lyophilization processes. Membranes produced with CHH presented the average maximum value of porosity, which is in agreement with literature [114].

The increase of ceramic concentration did not present an evident direct variation in porosity values. However, inclusion of ceramic the matrix tended to reduce scaffold porosity. For a better idea of the real porosimetry values the analysis should use ethanol instead of PBS and water or with other method such as mercury intrusion porosimetry.

Furthermore, is important to mention to the heterogenous distribution of pores throughout the membrane, as can be observed in the SEM and Bioactivity chapters.

3.2.1.3 SEM

The morphologies of the scaffolds were examined with SEM. This analysis allows the study of pose size distribution and sample structure. The SEM images of the produced polymeric scaffolds is presented in Figure 3.11, where image A and B represent the CHH and image C and D represent the CHL.

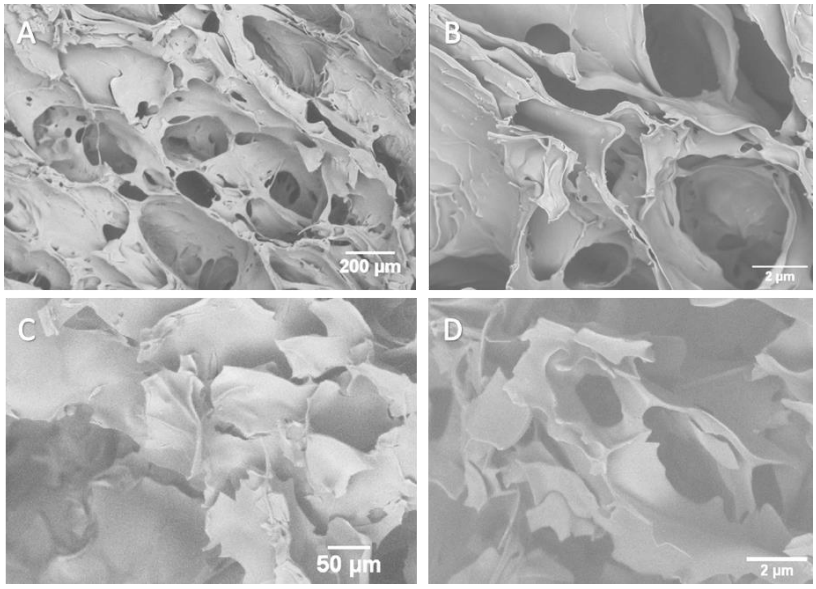

Figure 3.11 - SEM images of CHH (A and B) and CHL (C and D) scaffolds at different magnifications.

Variable porous size and interconnected porous structure are observed in both polymeric membranes. The produced structure is similar to human bone tissue presented in Figure 3.12, which will enable a faster tissue regeneration by channeling and boosting new tissue formation. [113]

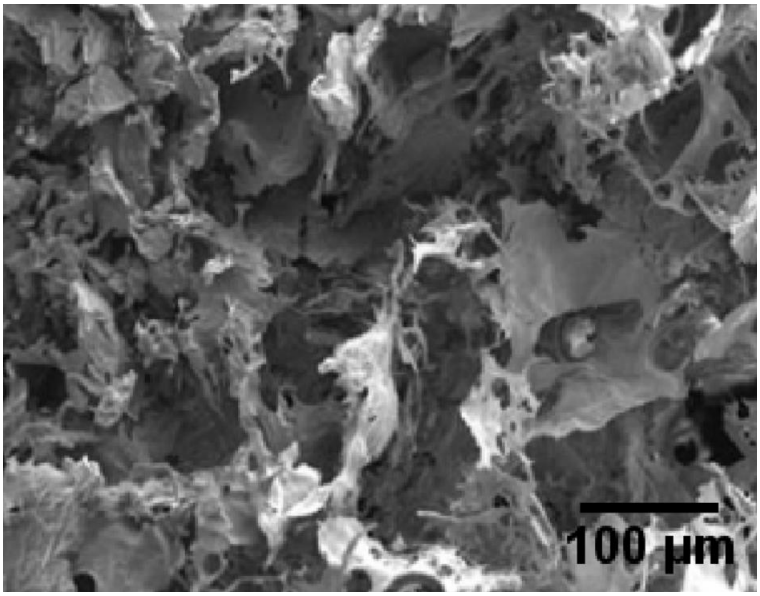

Figure 3.12 - SEM image of human bone tissue with interconnected pores. Adopter from [113].

Since the SEM images of chitosan membranes are similar, only the composite membranes with CHL are presented below (Figure 3.13). The CHH composite membranes are displayed in Appendix VII, Figure A. 17.

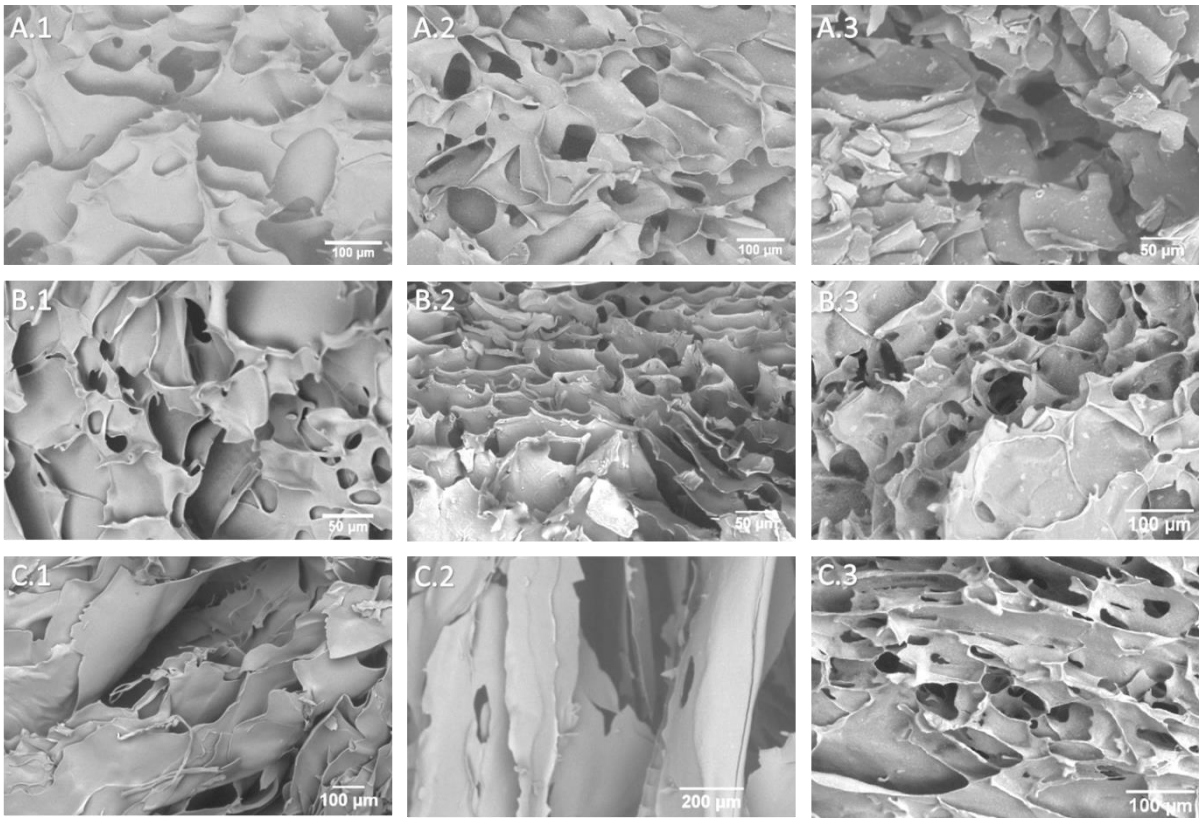

Figure 3.13 - SEM imaging of low-MW chitosan with FR (A), MHAp (B) and MBG (C) composite membranes at 25%w/w (1), 50%w/w (2) and 75%w/w (3).

All the produced scaffolds presented interconnected porous structure in all the tested composite compositions. The pores have a preferential orientation (Figure 3.13 C.2 and Figure A. 18) varying inside the same sample mold, as a result of the cold front direction in the freezing stage of the lyophilization process. [58] The samples also showed variations on pores sizes as observed in Figure A. 18 from the deposition of ceramic materials before the lyophilization process.

The structures presented a uniform distribution of ceramic NP in the polymeric structure with the exception of same agglomeration nucleus in punctual locations on the high concentration membranes. However, the NP appeared to be integrated within the chitosan matrices. [62]

All the produced scaffolds presented microporous structure with high porous size distribution not just ideal for cell adhesion and proliferation, but also for interlocking between the scaffolds and surrounding tissue which will improve the mechanical stability of the implant. [113]

3.2.2 Physicochemical properties

3.2.2.1 FTIR

The FTIR analysis for the polymeric scaffolds is presented in Figure 3.14 (graphic A) and for the mesoporous composite scaffolds is presented in **Error! Reference source not found.** (graphic B). F TIR spectra of the rest of the samples is presented in Appendix II: Figure A. 2 for the FR samples, Figure A. 3 for the MHAp samples and Figure A. 4 for MBG samples. In all of the figures the graphic A refers to the membranes with CHL and graphic B to those with CHH.

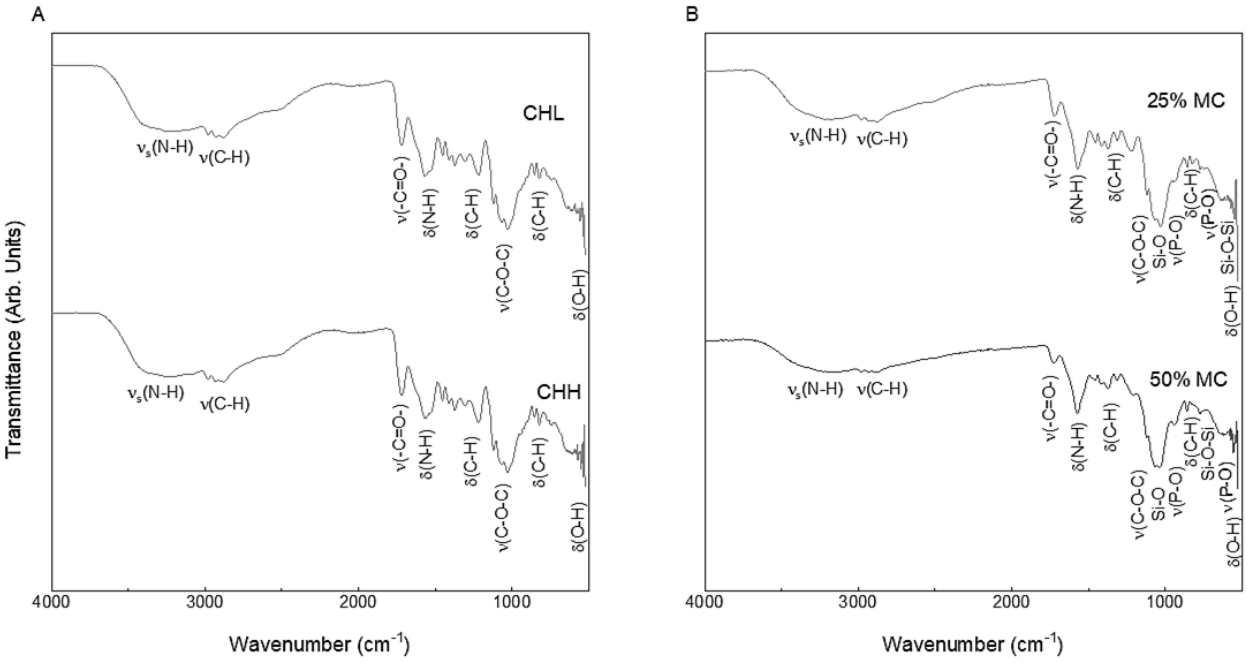

Figure 3.14 - FTIR of polymeric membranes (A) and mesoporous composite membranes (B).

The polymeric membranes presented the same bands as the polymeric raw material. The composite membranes present the bands for all the ceramic and polymeric materials used.

In **Error! Reference source not found.** it's possible to observe the width reduction of the 1000 cm^{-1} b and which corresponds to the major MBG and MHAp bands. This variation is due to the overlap of asymmetric stretching mode of the PO_4^{3-} group and to Si–O Q^2 and Q^3 units. The MHAp also induces the formation of 560 cm^{-1} peak for the asymmetric bending mode of the PO_4^{3-} . The introduction of MBG alters the peak of Si–O–Si symmetric stretching at 800 cm^{-1}.

The composite membranes with just MHap or MBG present the CH FTIR bands and the variations described above for the respective used ceramic.

3.2.2.2 Swelling

Swelling of the membranes occurs in three different stages. The first stage has a quick water absorption attributed to the interaction between water molecules and the chitosan hydrophilic groups (OH and NH_2).[93] In the second stage, the swelling rate gradually slows down since the formation of hydrogen bonding interaction within CH matrix, constrained the membranes swelling behavior. The last stage the

swelling reaches the plateau due to stabilization of membranes. [115] Swelling behavior of the polymeric scaffolds is as shown in Figure 3.15.

The membranes without ceramic have a longer first stage, still there is a significant increase of swelling during 48hrs, which does not happen in the composite membranes. Following the samples 72hrs submersion, the swelling rate starts to stabilize. [115]

At the end of the swelling test, the high-MW chitosan membranes showed higher swelling capacity and higher uptake time than the membranes with CHL. [116]

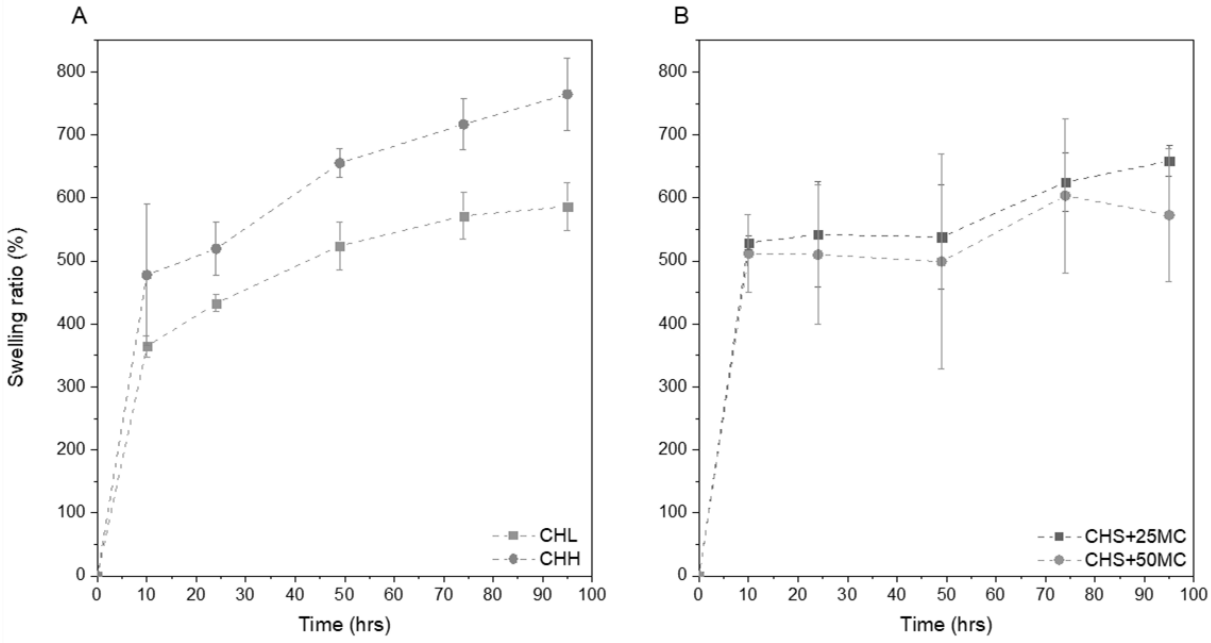

Figure 3.15 - Swelling behavior of CHL and CHH Polymeric scaffolds (A) and of CHL+MC scaffolds (B). Data obtained from a sample of three replicas for each plot point.

The swelling behavior of composite membranes is presented in Appendix III, where Figure A. 5 presents the swelling ratio of FR composite, Figure A. 6 for MHAp composite, Figure A. 7 for MBG and Figure A. 8 for the mesoporous composite. In Figure 3.16 is presented the resume of swelling capacities for every stabilized composite scaffold.

The composite membranes with FR present swelling rates in same order of values for both the polymer membranes. Comparing the composite scaffolds with the same type of polymeric membrane, the low-MW polymeric scaffolds were of the same order and the CHH scaffolds presented a slightly reduction of swelling with the addition of FR. The increase of ceramics concentrations in scaffolds, showed a decrease of swelling capacity at a faster rate, as expected from previous studies. [62]

The composite membranes with MHAp, displayed swelling capacity in the same range of values, in both polymers. The swelling capacity decreased, with the increase of ceramics concentrations for the CHH membranes. In the low-MW membranes the increase of ceramics did not produce any significant swelling variations.

The CHH/MBG composite membranes present slightly higher swelling ability than CHL/MBG. CHL/MBG swelling behavior is similar to the that of the polymeric membranes. The swelling analysis of the variation with MBG concentration shows that with the increase of ceramic concentration in the scaffolds the swelling capacity increases, until it reaches superior values than those of the pure polymeric membranes. This behavior was not expected, since previous works established BG to decrease scaffolds swelling capacity [87], [117]–[119]. However, *V. Maquet et al*. [120] concluded that the water absorption, in high concentration of BG composites, is much more swiftly (similar behavior to Figure 3.15, graphic B), thus reaching higher swelling capacities in the short term analysis. Nevertheless it's maximum water capacity is more stable than of polymeric scaffolds, which still did not reach the plateau in the Figure 3.15 (graphic A) at the last measurement taken, so when stabilization

occurs the swelling capacity will be similar or superior to the composite swelling capacity. Other reason for the increase of the swelling capacity of the MBG membranes is the water retention inside the pores of the MBG which is almost impossible to remove because of the small pores size.

The composites produced with mesoporous powders showed the similar swelling capacity for both ceramic concentrations (25% and 50%). Swelling plateau is also attained sooner for these samples. From all the samples, these compositions were the ones more stable in the last swelling stage.

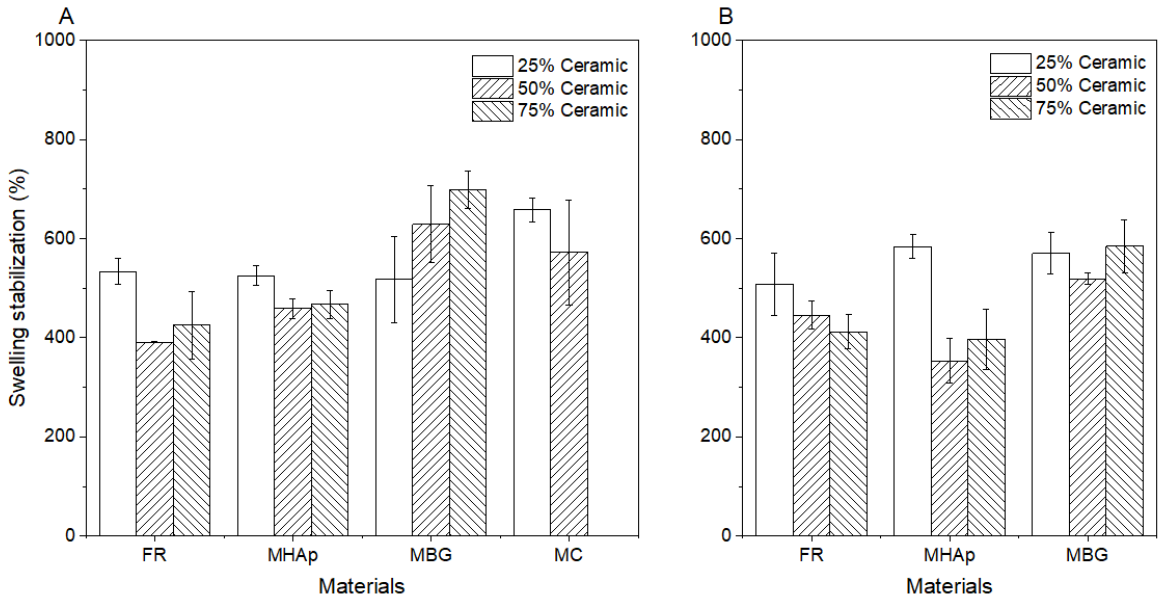

Figure 3.16 - Resume of composite membranes swelling capacity. Data obtained from a sample of three replicas for each scaffold.

All samples were able to absorb water, in proportions of more than three times than their own weight. The individual values obtained were greater than 300%, even in the scaffolds with higher ceramic concentration. This swelling capacity can guaranty an increase of the pores size and volume, that facilitates cell infiltration, growth through the scaffolds surfaces and the supply of nutrients and oxygen to the interior regions of the composite scaffolds. [119], [121], [122]

However, studies [87], [122], [123] show that uncontrolled increase in swelling, can also decrease the mechanical properties of the scaffolds which can be harmful for tissue regeneration applications. Therefore, controlled swelling is ideal for the pretended applications. Nevertheless, *D. Arcos* et al. [51] show that incorporation of mesoporous ceramics may increase compressive modulus after submersion in SBF, so the MBG higher water retention capacity is a beneficial factor for tissue engineering applications.

3.2.2.3 Degradation

The biodegradation behavior of the material is a crucial factor on the long-term performance of tissue-engineered cell–material construct, as cells need a stable material to adhere and proliferate. [59], [124] In order to, analyze the polymeric membranes biodegradation profile, the different MW chitosan scaffolds were immerged in PBS containing lysozyme for 7 days and 14 days. The obtained results are presented in Figure 3.17.

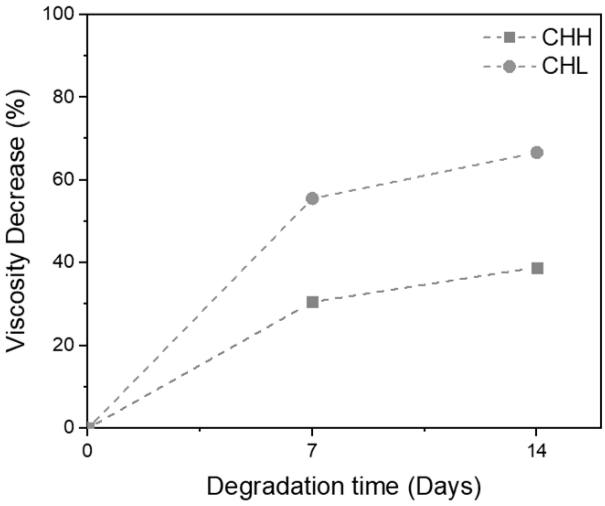

Figure 3.17 - Viscosity decrease of CHL and CHH polymer in function of degradation time. Data obtained from a sample of six replicas for each plot point and error bars are not visible in the presented scale.

The viscosity decrease was greater in the CHL, situation observed in other works [62]. Since the samples viscosity alter in function of the polymeric chain size, a reduction of viscosity means a decrease of chitosan MW and the low-MW chitosan suffered a higher degradation than the CHH. [86], [125]

The presented results are slightly higher than the expected (5% to 15% weight loss from [62], [126], [127] and decrease of viscosity from [85], [128]) for the period of degradation time in stake. Two of the factors outside from the reduction of polymer chain, that could have resulted in these values are the absorbed water that remained after the scaffold primary drying (previous to the lyophilization drying) or the PBS precipitations that remained after washing the samples. The absorbed water reduces the polymer concentration and therefore decreases solution viscosity. [125] In the PBS precipitation hypothesis, when the polymer was dissolved for the viscosity analysis, the precipitates were also dissolved and altered the ratio between the original sample and the ones subjected to degradation. The obtain results might be questioned if they are due to PBS crystals or water swelling. Although the result seamed to point to water swelling since the samples presented a weight reduction after lyophilization, further studies like X-ray fluorescence might be required to confirm this.

From the maximum weight loss analysis presented in Figure 3.18 and the degradation results of CHL (89.3 ± 0.2%) and CHH (90.3 ± 0.8%), the composite membranes reduced the scaffolds degradation. This behavior was expected since the Lysosome only degrades the polymer and the ceramic remains unaltered. Therefore, the increase of ceramic concentration on the membranes decreases the membrane degradation (Appendix IV). [62], [63]

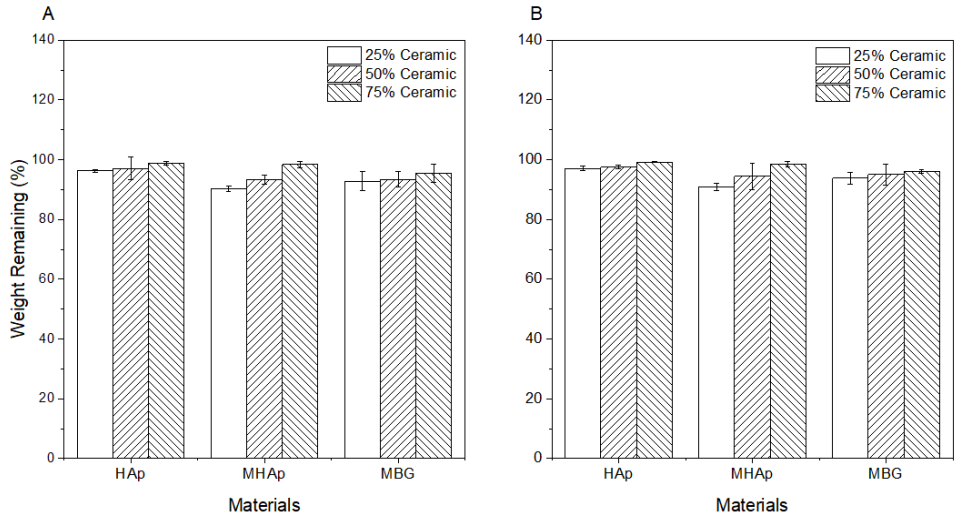

Figure 3.18 - Degradation behavior of CHL composite scaffolds (A) and CHH composite scaffolds (B). Data obtained from a sample of three replicas for each scaffold.

The obtain weight data confirmed that CHL have a higher degradation rate and the results based on the remaining weight fit in the previous degradation expectations. [62], [126], [127]

One of the solution for a lower polymeric degradation is to reticulate the polymeric membranes so that the bonds between polymeric chains are stronger and the Lysozyme cannot reach the β-1-4 glycosidic bond of the polysaccharides as easily. [126]

3.2.2.4 Bioactivity

Larry L. Hench et al. defined a biomaterial as a material "that elicits a specific biological response at the interface of the material which results in the formation of a bond between the tissues and the material". [129] This bond is formed due to the formation of bonelike apatite on the scaffolds surface when implanted in the living body (bioactivity). [78], [129]

The *in-vitro* bioactive study allows a simulation of the expected response of the materials *in-vivo* bone bioactivity from the apatite formation on its surface, when immersed in SBF for a specified time gap, since the SBF solution have a nearly equal ion concentrations to human blood plasma. [78]

The in-vitro bioactive results are presented in Figure 3.20, where column 1 presents the CHL membranes, column 2 presents the CHL+25%FR membranes, column 3 presents the CHL+25%MHAp membranes and column 4 presents the CHL+25%MBG membranes. The rows represent the time of SFB immersion where row A is 3h, row B is 6h, row C is 12h, row D is 24h, row E is 48h, row F is 72h and row F is 7 days. The same organization is applied to Appendix V, Figure A. 12.

This analysis showed the CHL almost did not present any apatite precipitation in the 7 days study. However, the polymeric walls of the membrane changed texture and organization throughout the majority of the tested times.

The composite scaffolds presented different responses to the test, nevertheless, all the composites had an increase of apatite precipitation. The precipitation begins at spots with higher rugosities or with small pores and then increases in size and distribution. The time gap of the assay did not show a high surface coating for most of the tested scaffolds and in same samples was presented apatite precipitation and for higher times no precipitation was registered (e.g. Figure 3.19**Error! Reference source not found.** C), this fact could be due to from local increase of ceramic concentration.

The CHL membrane with 25% FR had the better result with the formation of an almost complete layer of apatite on the 72h sample.

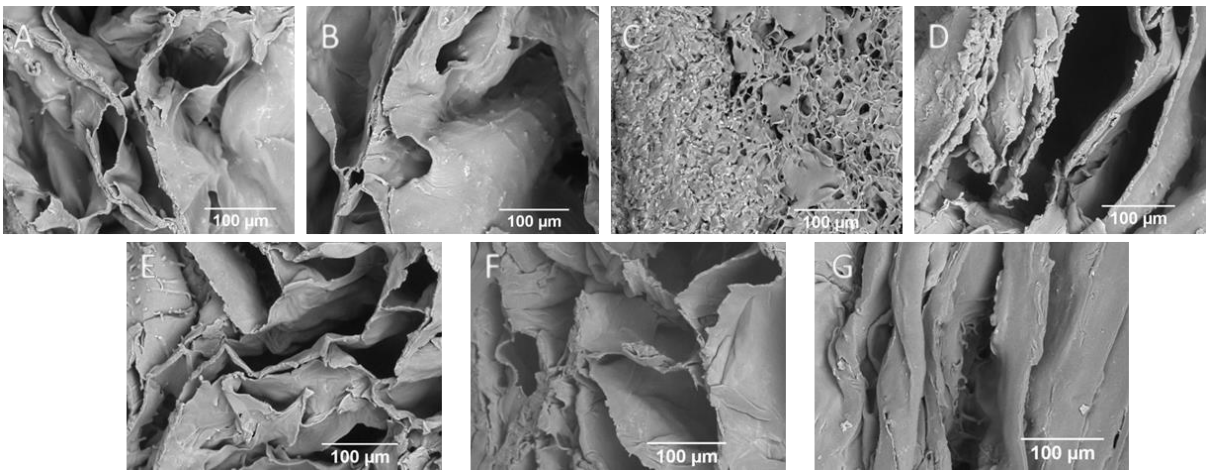

Figure 3.19 - SEM images of the CHL+25%MC membranes after immersion in SBF for 3h (A), 6h (B), 12h (C), 24h (D), 48h (E), 72h (F) and 7days (G).

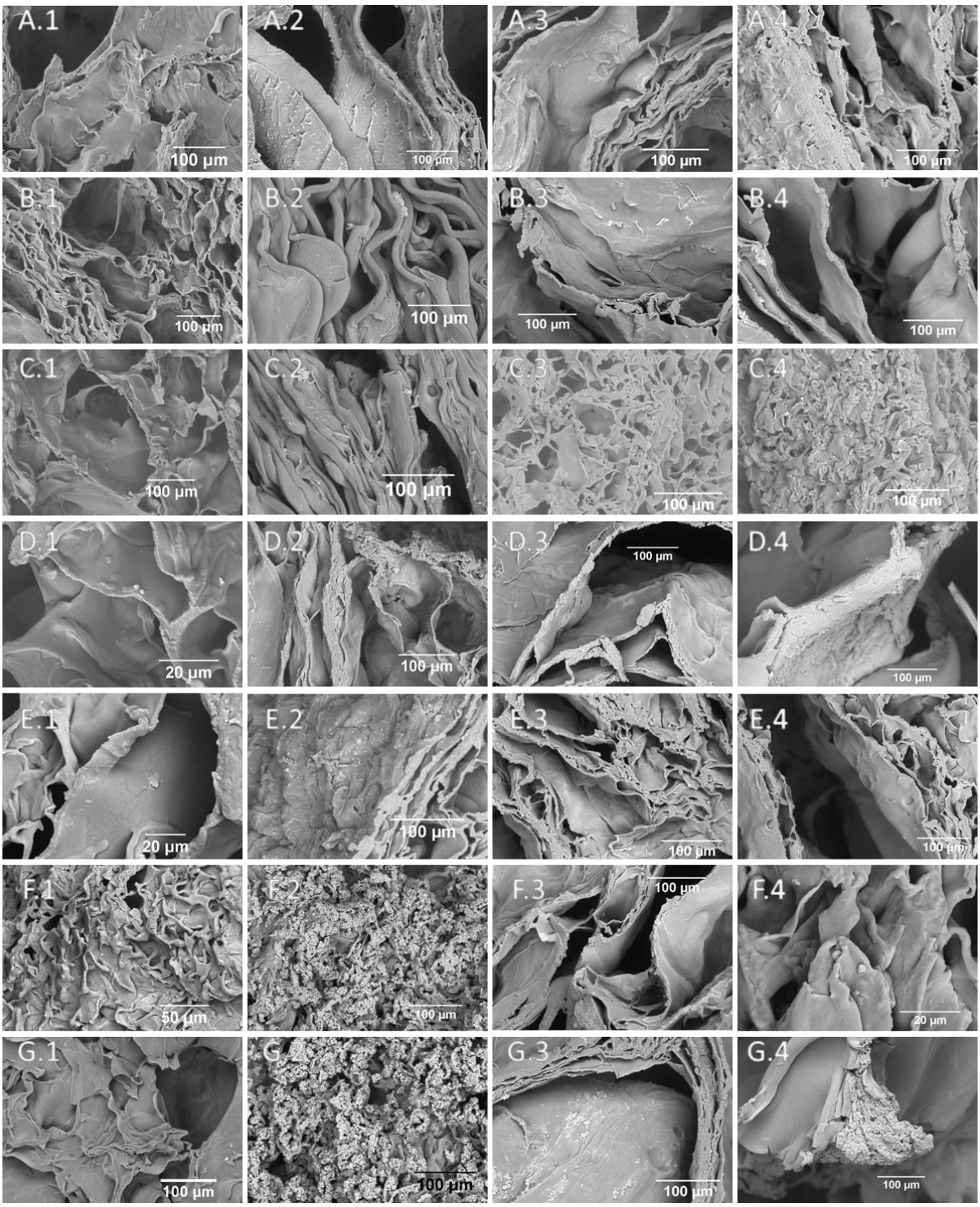

Figure 3.20 - SEM images of the CHL membranes (1), CHL+25%FR (2), CHL+25%MHAp (3) and CHL+25%MBG (4) after immersion in SBF for 3h (A), 6h (B), 12h (C), 24h (D), 48h (E), 72h (F) and 7days (G).

3.2.3 Mechanical properties of scaffold

3.2.3.1 Compression modulus

The developing of load-bearing scaffolds with high porosity is one of the major purposes of bone tissue engineering. However, the highly porous structure is obtained at the expense of mechanical strength. [112] In this tradeoff the highly porous structure is preferred in Tissue Engineering applications.

In order to analyze the compressive modulus of porous composite scaffolds, the samples were tested using a mechanical testing machine and from the obtained data the slope of the stress–strain plot at 5 to 10% deformation range was calculated. During the test the pores collapse and the structure underwent densification . [119]

The typical stress-stain curves are classified in three regions: linear elastic, collapse plateau, and densification regimes as illustrated in Figure 3.21 graphics A and B. [123]

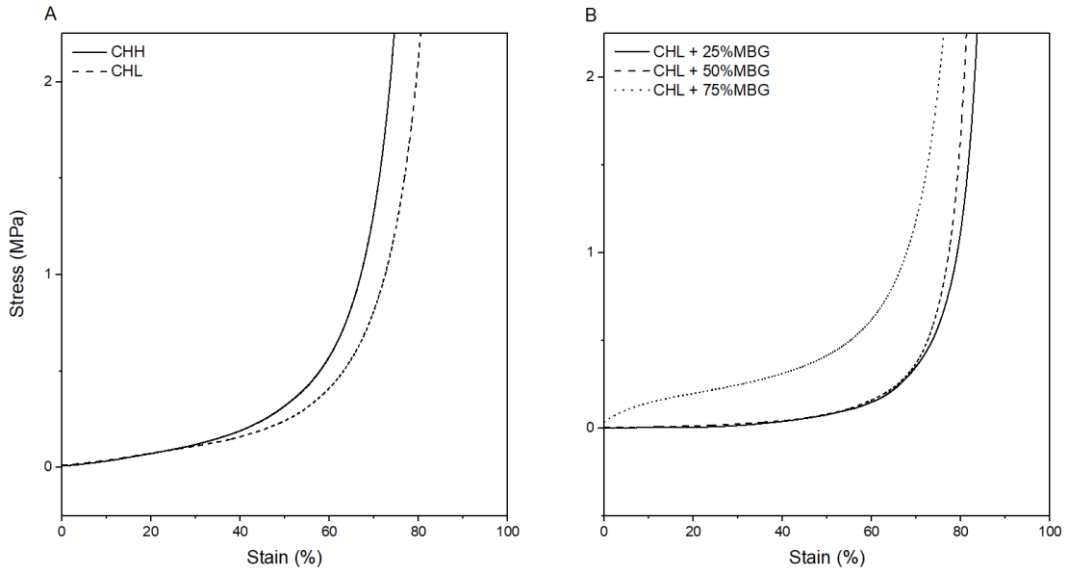

Figure 3.21 - Stress–strain curves of the chitosan scaffolds (A) and an example of different ceramic concentrations of MBG with CHL (B).

The polymeric membranes presented a similar compressive modulus of 159 ± 9 KPa for the CHL and 151 ± 46 KPa for the CHH. The similarity in values were not expected since it's been reported a superior mechanical behavior with the increase in MW of the polymeric chain. [62] However, the similar mechanical strength of the different polymers could be due to the slight increase in the porosity in the CHH scaffold.

With the increase of ceramic in the scaffolds, the elastic Slope tented to increase in on the first 15% of the stress-strain curve, as showed in graphic B of Figure 3.21. This Slope increase means an increase of compressive modulus of the tested membranes.

The resume of composite compressive strength is presented in Figure 3.22, where the scaffolds in graphic A are from the CHL and the membranes in graphic B from the membranes with CHH.

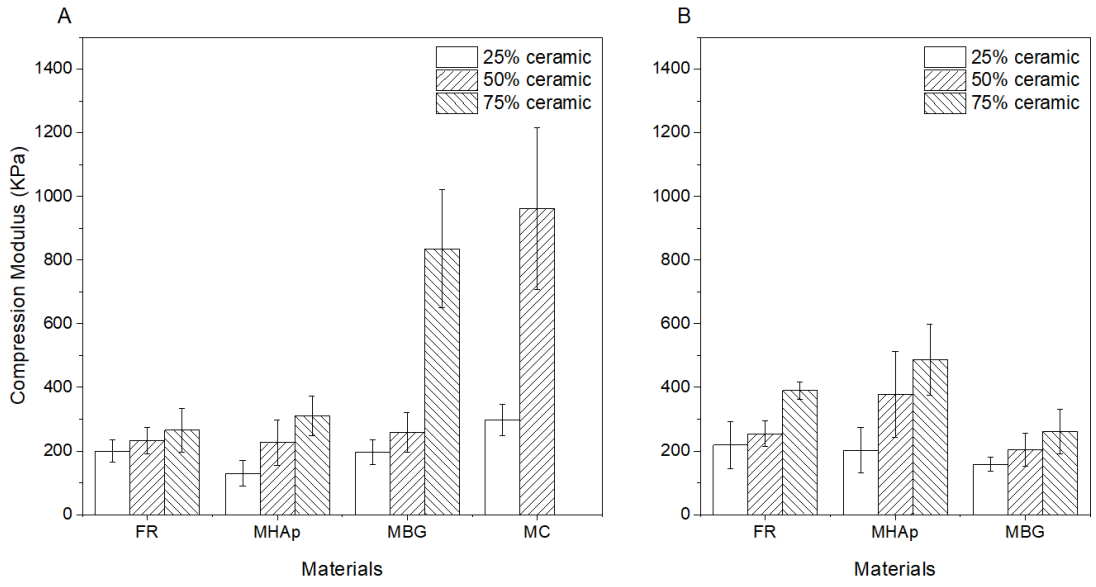

Figure 3.22 – Compression modulus of composite scaffolds with CHL (A) and CHH (B). Data obtained from a sample of ten replicas for each scaffold.

The compressive modulus significantly increased with the incorporation of ceramic materials in both low and high MW chitosan scaffolds for all the tested compositions. All composite scaffolds, except the 75%MBG, presented a higher increase of mechanical strength with the CHH than the low-MW CH.

The results showed a significant increase in the CHL membranes, especially for the MBG and MC scaffolds. This fact could be due to the mesoporous structure of the produced MBG. Furthermore, the CHL presented smaller errors bars, this fact is due to an easier NP dispersion and a more uniform polymer solvability, where was granted no polymer granules. These facts render the CHL samples more uniform.

The highest value of compressive modulus was obtained from the composite produced with mesoporous powders. The MC membranes at 25% of ceramic concentration obtained comparable compressive modulus results other composites at 50% ceramic concentration. The behavior was obtained with half ceramic concentration, meaning less material thus lower cost solution.

3.2.4 Cell culture studies

The cell response to the composite membranes was evaluated through cytotoxicity, adhesion and proliferation tests.

3.2.4.1 Cytotoxicity

The cytotoxicity of the composite scaffolds produced was tested to confirm that the synthesis of the membranes does not cause chemical modifications. These modifications could alter the non-cytotoxicity of chitosan. The results are displayed in Figure 3.23 for the polymeric membranes and in Appendix VIII, Figure A. 19 for the composite membranes with the FR biphasic, in Figure A. 20 for the MHAp, Figure A. 21 for the MBG scaffolds and in Figure A. 22 for the mesoporous composites with low-MW chitosan. In all these figures the graphics A are for the CHL and the graphics B for CHH.

Of the two tested polymers, CHL showed higher cell viabilities for all the composites. Comparing the different ceramics results, MHAp had the lowest and MBG the highest cell viability. This fact is most noticeable for the extracts with high concentration (12.5 mg/mL and 25 mg/mL).

None of the composite samples were cytotoxic, therefore all can be used in bone regeneration applications.

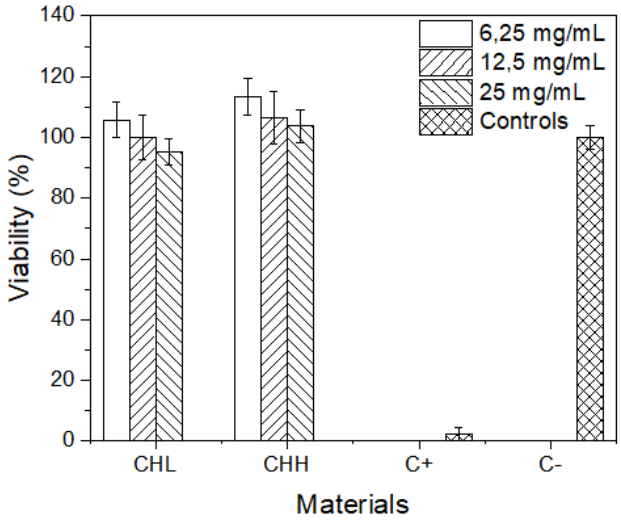

Figure 3.23 - Relative Cell Viability in cytotoxicity tests of CHL (A) and CHH (B) membranes. Data obtained from a sample of four replicas for each membrane.

3.2.4.2 Cell Adhesion and Proliferation

The cell adhesion assays were performed in two stages. In the first stage, chitosan with different MW were tested in order to identify the best response so that in the second stage all the tested composites contained the same polymer. This selection method allowed the analyzes of the second stage to focus on the different ceramics under study and their concentration on the scaffold.

The first stage assay revealed that the chitosan scaffolds with CHL have a slightly higher cellular adhesion (48 ± 6%) than the CHH (41 ± 6%). These values were expected since chitosan is known for its low cell adhesion [130]. The better response of low-MW CH could be due to the polymer slightly higher degree of deacetylation, which is one of the major factors influencing cell adhesion to chitosan.[58]

Cell proliferation on CHL scaffolds is also slightly higher than on CHH scaffolds and is presented in Figure 3.24.

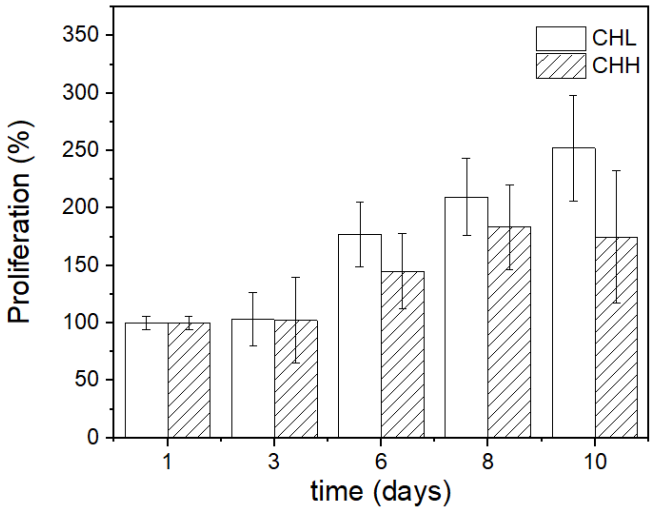

Figure 3.24 – Cell proliferation of chitosan with CHL and CHH. Populations are normalized to day 1 values. Data obtained from a sample of six replicas for each membrane.

Based on these results, on the second stage assay only the composite membranes with the CHL were tested since they should also have better adhesion than the composite CHH based scaffolds. One of the major purposes of this experiment is to identify the best sample for bone regeneration: therefore, all ceramics were tested using their highest and lowest concentrations (75%w/w and 25%w/w). This method guaranteed that all ceramics in composite scaffolds were tested and its possible to identify cell adhesion dependence on ceramic concentration.

The second stage cell adhesion assay (24h), summarized in Figure 3.25 and Table A. 5 (Appendix VII), presented that the MC scaffolds and the lower concentration MBG scaffolds, have a higher cellular adhesion than the other tested materials.

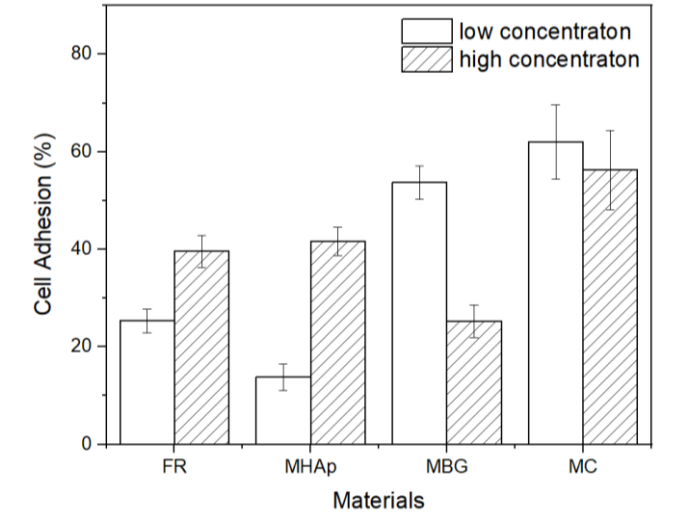

Figure 3.25 - Cell Adhesion to composite materials. Data obtained from a sample of six replicas for each scaffold.

In the FR and MHAp samples cell adhesion increased with the increase of ceramic concentration as expected [62], however in the MBG samples the opposite was observed. This fact could be due to the

increase of pores volume but decrease of pores on the surface (Figure 3.27 C.2) with the increase of MBG concentration in the lyophilization process or morphology variations throughout the sample (Figure A. 18).

The cell proliferation profile is presented in Figure 3.26, where graphic A represents the low-MW chitosan with different concentrations of FR, graphic B the CHL with MHAp, graphic C the CHL with MBG and graphic D the CHL with mesoporous composite.

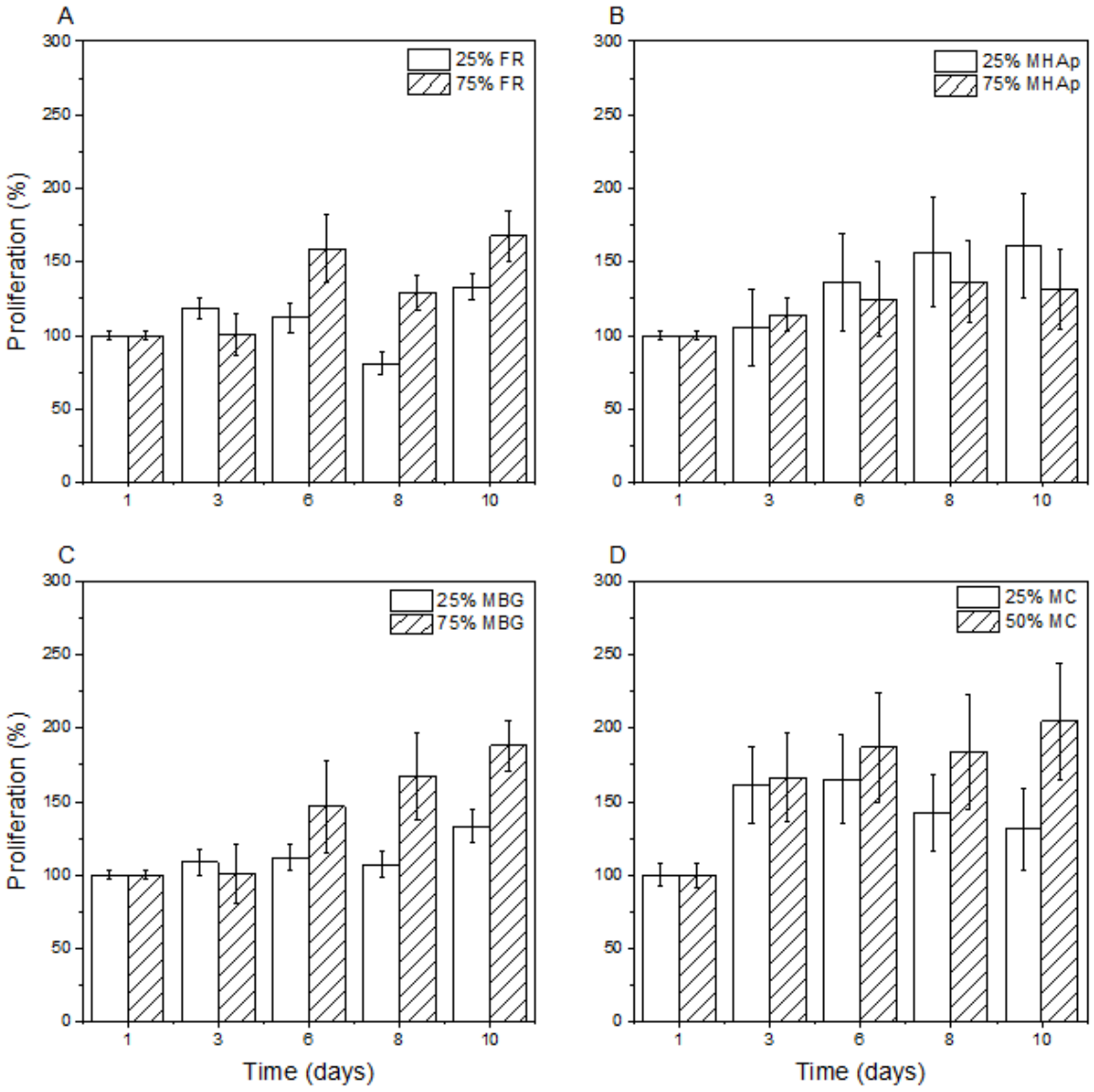

Figure 3.26 - Cell proliferation in composites with CHL of FR (A), MHAp (B), MBG (C) and mesoporous composite (D). Populations are normalized to day 1 values.

Cell proliferation on the MHAp membranes was smaller for the highest ceramic concentration. This fact is a result of the high concentration of material in contact with cells (direct contact) as is a reinforcement of the cytotoxic assays that showed a decrease of cell viability with the increase of contact between membranes and cells.

The other tested scaffolds showed a higher cell proliferation with higher ceramic concentration on the membranes. From the results obtained, the 75% MBG and 50%MC presented superior cell proliferation.

Fluorescence microscopy confirmed that human osteoblasts were able to attach, proliferate and inhabit almost all tested composite scaffolds for 10 days. The MBG and mesoporous composite presents the greatest abundance of stained cells (the bright green spots), which corresponds to viable cell's nucleus. The presented cell density confirms the high cell adhesion and proliferation rate obtained by Resazurin

reading. This test also indicates that the scaffolds support cell viability and could be a suitable support for bone regeneration.

The cell populations did not present any preferential organization and appear to have infiltrated within the scaffold, yielding a uniform population throughout the membrane.

The Fluorescence analysis in Figure 3.27 confirms the higher cell population in the MBG and mesoporous composites. The MHAp did not present marked cell (Appendix VII, Figure A. 23), this fact could be due to cell penetration into the interior of scaffolds and the microscope could not detect their signal or due to the previously obtained signal from Resazurin reduction being a result of membrane chemical variations during cell culture.

The cell controls and materials controls are presented respectively at Appendix VII Figure A. 25 and Figure A. 24.

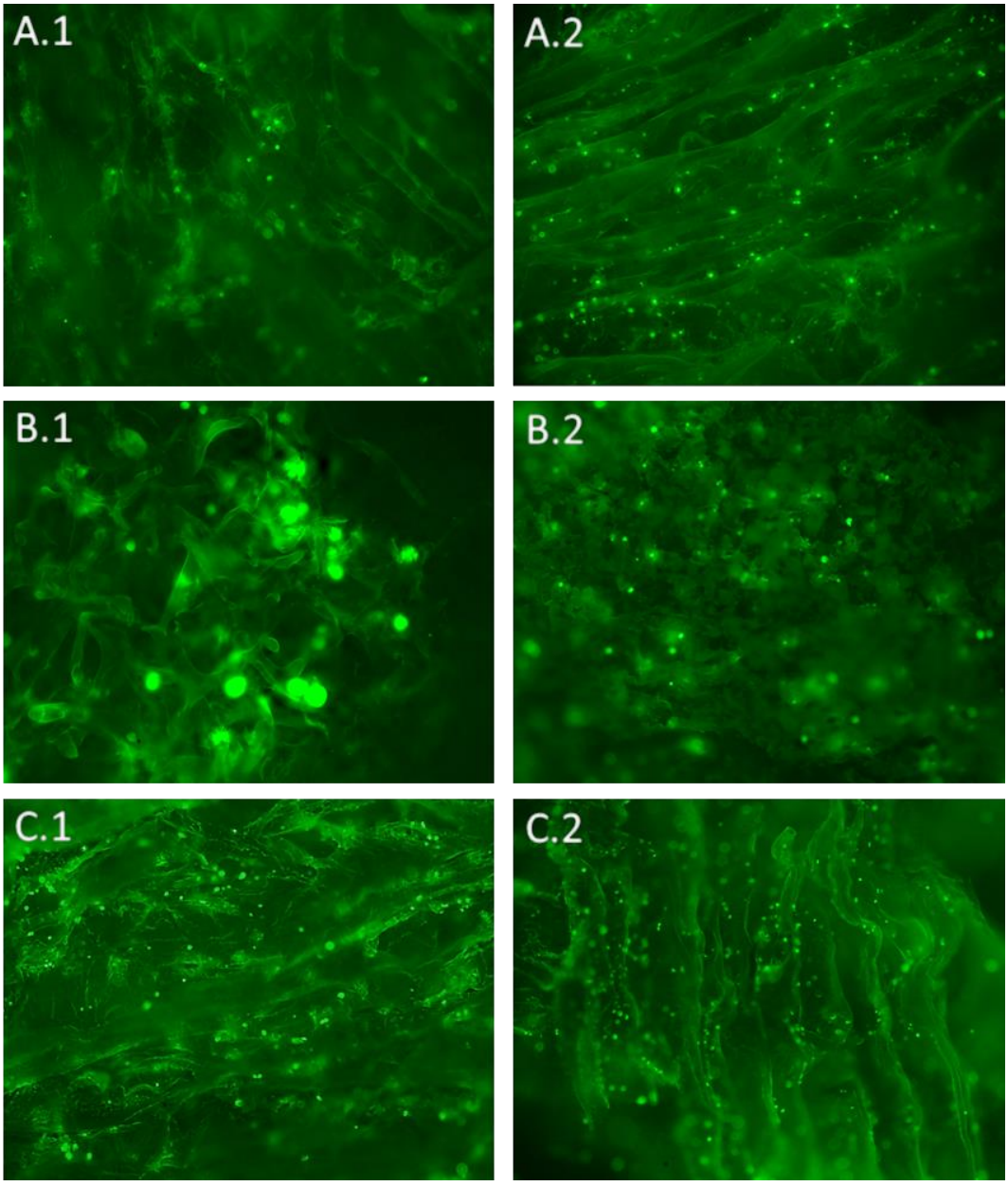

Figure 3.27 - Fluorescence images of FR (A), MBG (B) and MC scaffolds (C) with low (1) and high (2) ceramic concentrations.

4 Conclusion

The ceramic mesoporous materials (MBG and MHAp) were synthesized by the sol-gel method and analyzed by FTIR, DSC-TGA, DRX, TEM, nitrogen sorption porosimetry and cytotoxicity tests. The FTIR results showed the specific peaks of CH for the CHL and CHH samples, the HAp peaks for the FR and MHAp and BG for the MBG. Furthermore, this technique showed a reduction of temperature for the HAp syntheses with the addition of F127 to the reaction with the formation of the specific peaks at lower temperatures. The DSC-TGA confirmed the FTIR results and guaranteed the elimination of the polymeric surfactant with the 700ºC calcination, since the F127 is eliminated at 400ºC.

The XRD analysis of the raw materials confirmed the crystallographic organization of MHAp, the semi-crystalline structure of the used CH and the amorphous structure of the MBG. The TEM images showed patterns typical of mesoporous structure, with poorly ordered wormlike aggregates with numerous individual mesoporous in both MBG and MHAp images. The nitrogen sorption porosimetry confirmed the mesoporous structures of the produced ceramics, with smaller pores than previously reported studies due to the surfactant concentration used in the synthesis. Moreover, the addition of F127 to the HAp reaction, reduced the porous size and increased the surface area. The cytotoxic tests confirmed that all materials are safe to be used in the composite scaffolds.

The pretended polymeric scaffolds were successfully produced by lyophilization. Neutralization and dialysis processes were done to remove all the acid remaining in their structure, so it would maintain their morphology on contact with liquids. The scaffolds were analyzed in terms of their morphology, physicochemical, mechanical properties and cell culture studies.

The structural analysis resorted to XRD and the morphology from Porosimetry and SEM analysis. The XRD showed the presence of major ceramic HAp peaks in FR, MHAp and MC composites. Also showed the absence alteration of peaks in the MBG composites. The Porosimetry presented high values for all the tested samples, with a slightly decrease with the addition of ceramic materials to the scaffolds. SEM images showed that the CHL and CHH membranes presented similar structures with interconnected pores, similar to the structure of the cancellous bone. The addition of ceramics to the CH solutions, facilitated its integration into the chitosan walls and a preferable orientation of pores during the lyophilization process. The added ceramics was distributed uniformly in the polymeric structure, except for some agglomeration in punctual locations on the scaffolds, with higher ceramic concentration.

The physical and/or chemical properties were tested by FTIR, swelling behavior, degradation test and bioactivity assay. The FTIR spectra showed the junction of the bands presented in the raw materials analyses, for the composite scaffolds and band variation on the overlay bands, confirming the ceramic presence in XRD and SEM images. The swelling behavior, with the increase of ceramic concentration in the scaffolds, showed a decrease of swelling capacity and a lower time reaching the swelling plateau. The composite scaffolds with higher swelling capacity were the CHL+75%MBG and the MC. The degradation tests showed a higher degradation for the CHL, that can be reduced by polymer reticulation. The bioactivity assay presented an improvement with the addition of ceramic, as observed with the increase of apatite precipitation, particularly in the FR sample.

The mechanical properties presented an increase of the compressive modulus, with the increase of ceramic concentration. The best results were achieved in the CHL+75%MBG (836 ± 185 KPa) and CHL+50%MC (962 ± 254 KPa).

The cell culture studies included cytotoxic tests, adhesion assays, proliferation tests and fluorescence assays. The cytotoxic tests showed that none of the composite samples produced were cytotoxic, therefore safe to be used in bone regeneration applications. The adhesion was higher on the CHL membrane and the ceramics tend to improve cell adhesion to the scaffold's membranes. The best results were obtained for the MC scaffolds. Cell proliferation study showed the 75% MBG and 50%MC presented superior cell proliferation. The fluorescence presented no preferential organization with cell infiltrated within the scaffold and yielding a uniform population throughout the membrane.

All the produced scaffolds have given evidence of being Biodegradable and Bioactive. However, the overall best performance composite was CHL+50%MC, meaning this sample obtained better results in almost all tested scaffolds proprieties.

5 Future Work

To Further improve the obtained results, the lyophilization process could be adjusted for better uniformity thought-out the same membrane and to obtain more uniform structures in the samples with higher ceramic concentrations. The 75%MC should be evaluated in a 1MBG/1MHAp and different ratios.

The neutralization process could improve if applied before the first lyophilization, so that FR could be implanted completely in scaffold structure instead of being partially washed away during neutralization. This process alteration would improve scaffolds bioactivity and compressive modulus.

To finish this study is still needed *in-vivo* such as sensitization tests, acute systemic toxicity and material-mediated pyrogenicity to verify if all the requirements of ISO10993 for posterolateral spine fusion implants. Additionally, should be needed Gama irradiation studies with variation of dose and radiation effect in the composite membranes, since this process is required for the product commercialization's.

It would be interesting to test the effect of a production of MBG and MHAp composite in a multilayer MHAp/MBG/polymer and if it would have a better cell response and higher compressive strength.

References

[1] K. Storheim and J.-A. Zwart, "Musculoskeletal disorders and the Global Burden of Disease study," *Die Cast. Eng.*, vol. 46, no. 4, p. 64, 2014.

[2] L. March *et al.*, "Burden of disability due to musculoskeletal (MSK) disorders," *Best Pract. Res. Clin. Rheumatol.*, vol. 28, no. 3, pp. 353–366, 2014.

[3] "Orthopedic Biomaterials Market Size | Global Industry Report 2019-2025." [Online]. Available: https://www.grandviewresearch.com/industry-analysis/orthopedic-biomaterials-market. [Accessed: 08-Sep-2019].

[4] O. Johnell and J. A. Kanis, "An estimate of the worldwide prevalence and disability associated with osteoporotic fractures," *Osteoporos. Int.*, vol. 17, no. 12, pp. 1726–1733, 2006.

[5] E. Hernlund *et al.*, "Osteoporosis in the European Union: Medical management, epidemiology and economic burden: A report prepared in collaboration with the International Osteoporosis Foundation (IOF) and the European Federation of Pharmaceutical Industry Associations (EFPIA)," *Arch. Osteoporos.*, vol. 8, no. 1–2, 2013.

[6] T. Kurien, R. G. Pearson, and B. E. Scammell, "Bone graft substitutes currently available in orthopaedic practice: The evidence for their use," *Bone Jt. J.*, vol. 95 B, no. 5, pp. 583–597, 2013.

[7] A. El-Ghannam, "Bone reconstruction: From bioceramics to tissue engineering," *Expert Rev. Med. Devices*, vol. 2, no. 1, pp. 87–101, 2005.

[8] E. García-Gareta, M. J. Coathup, and G. W. Blunn, "Osteoinduction of bone grafting materials for bone repair and regeneration," *Bone*, vol. 81, pp. 112–121, 2015.

[9] V. I. Sikavitsas, J. S. Temenoff, and A. G. Mikos, "Biomaterials and bone mechanotransduction," *Biomaterials*, vol. 22, no. 19, pp. 2581–2593, 2001.

[10] J. S. C. Marks, P. R. Odgren, B. de Crombrugghe, J. Rossert, P. Garnero, and P. D. Delmas, *Principles of Bone Biology*, 2nd ed. Academic Press, 2002.

[11] R. R. Buckwalter, J. A.; Glimcher, M. J.; Becker, "Bone Biology," *J. Bone Jt. Surg. (Intructional Course Lect.*, vol. 77, pp. 1256–1275, 1995.

[12] A. J. Salgado, O. P. Coutinho, and R. L. Reis, "Bone tissue engineering: State of the art and future trends," *Macromol. Biosci.*, vol. 4, no. 8, pp. 743–765, 2004.

[13] P. Fratzl and R. Weinkamer, "Nature's hierarchical materials," *Prog. Mater. Sci.*, vol. 52, no. 8, pp. 1263–1334, 2007.

[14] D. Sommerfeldt and C. Rubin, "Biology of bone and how it orchestrates the form and function of the skeleton," *Eur. Spine J.*, vol. 10, no. SUPPL. 2, pp. 86–95, 2001.

[15] D. de Melo Pereira and P. Habibovic, "Biomineralization-Inspired Material Design for Bone Regeneration," *Adv. Healthc. Mater.*, vol. 1800700, p. 1800700, 2018.

[16] U. G. K. Wegst, H. Bai, E. Saiz, A. P. Tomsia, and R. O. Ritchie, "Bioinspired structural materials," *Nat. Mater.*, vol. 14, no. 1, pp. 23–36, 2015.

[17] M. Saito, K. Fujii, S. Soshi, and T. Tanaka, "Reductions in degree of mineralization and enzymatic collagen cross-links and increases in glycation-induced pentosidine in the femoral neck cortex in cases of femoral neck fracture," *Osteoporos. Int.*, vol. 17, no. 7, pp. 986–995, 2006.

[18] M. Saito and K. Marumo, "Effects of Collagen Crosslinking on Bone Material Properties in Health and Disease," *Calcif. Tissue Int.*, vol. 97, no. 3, pp. 242–261, 2015.

[19] M. Saito, S. Soshi, T. Tanaka, and K. Fujii, “Intensity-related differences in collagen post-translational modification in MC3T3-E1 osteoblasts after exposure to low- and high-intensity pulsed ultrasound,” *Bone*, vol. 35, no. 3, pp. 644–655, 2004.

[20] M. Saito and K. Marumo, “Collagen cross-links as a determinant of bone quality: A possible explanation for bone fragility in aging, osteoporosis, and diabetes mellitus,” *Osteoporos. Int.*, vol. 21, no. 2, pp. 195–214, 2010.

[21] The American Society for Bone and Minera Research, *Primer on the Metabolic Bone Diseases and Disorders of Mineral Metabolism*, 8th ed., vol. 4, no. 2. John Wiley & Sons, Inc. ©, 2013.

[22] R. A. Adler *et al.*, *Osteoporosis*, 3rd ed. 2008.

[23] P. J. Thurner *et al.*, “Osteopontin deficiency increases bone fragility but preserves bone mass,” *Bone*, vol. 46, no. 6, pp. 1564–1573, 2010.

[24] J. R. Harris, A. Soliakov, and R. J. Lewis, “In vitro fibrillogenesis of collagen type I in varying ionic and pH conditions,” *Micron*, vol. 49, pp. 60–68, 2013.

[25] C. F. C. João, “Inverted Colloidal Crystal Scaffolds: New Substitutes for Bone Tissue Engineering,” Universidade nova de Lisboa, 2016.

[26] N. Reznikov, M. Bilton, L. Lari, M. M. Stevens, and R. Kröger, “Fractal-like hierarchical organization of bone begins at the nanoscale,” *Science (80-.).*, vol. 360, no. 6388, 2018.

[27] M. J. Olszta *et al.*, “Bone structure and formation: A new perspective,” *Mater. Sci. Eng. R Reports*, vol. 58, no. 3–5, pp. 77–116, 2007.

[28] B. Wopenka and J. D. Pasteris, “A mineralogical perspective on the apatite in bone,” *Mater. Sci. Eng. C*, vol. 25, no. 2, pp. 131–143, 2005.

[29] L. T. Bang, B. D. Long, and R. Othman, “Carbonate hydroxyapatite and silicon-substituted carbonate hydroxyapatite: Synthesis, mechanical properties, and solubility evaluations,” *Sci. World J.*, vol. 2014, 2014.

[30] B. Gabbasov *et al.*, “Conventional, pulsed and high-field electron paramagnetic resonance for studying metal impurities in calcium phosphates of biogenic and synthetic origins,” *J. Magn. Magn. Mater.*, vol. 470, pp. 109–117, 2019.

[31] E. Boanini, M. Gazzano, and A. Bigi, “Ionic substitutions in calcium phosphates synthesized at low temperature,” *Acta Biomater.*, vol. 6, no. 6, pp. 1882–1894, 2010.

[32] E. Davies *et al.*, “Citrate bridges between mineral platelets in bone,” *Proc. Natl. Acad. Sci.*, vol. 111, no. 14, pp. E1354–E1363, 2014.

[33] J. M. Delgado-López *et al.*, “The synergic role of collagen and citrate in stabilizing amorphous calcium phosphate precursors with platy morphology,” *Acta Biomater.*, vol. 49, pp. 555–562, 2017.

[34] I. V. Pratt and D. M. L. Cooper, “A method for measuring the three-dimensional orientation of cortical canals with implications for comparative analysis of bone microstructure in vertebrates,” *Micron*, vol. 92, pp. 32–38, 2017.

[35] T. G. Bromage, H. M. Goldman, S. C. McFarlin, J. Warshaw, A. Boyde, and C. M. Riggs, “Circularly polarized light standards for investigations of collagen fiber orientation in bone,” *Anat. Rec. - Part B New Anat.*, vol. 274, no. 1, pp. 157–168, 2003.

[36] T. Yamamoto *et al.*, “Structure and formation of the twisted plywood pattern of collagen fibrils in rat lamellar bone,” *J. Electron Microsc. (Tokyo).*, vol. 61, no. 2, pp. 113–121, 2012.

[37] A. J. Wagoner Johnson and B. A. HersCHHer, “A review of the mechanical behavior of CaP and

CaP/polymer composites for applications in bone replacement and repair," *Acta Biomater.*, vol. 7, no. 1, pp. 16–30, 2011.

[38] G. Fernandez de Grado *et al.*, "Bone substitutes: a review of their characteristics, clinical use, and perspectives for large bone defects management," *J. Tissue Eng.*, vol. 9, p. 204173141877681, 2018.

[39] J. Venkatesan and S. K. Kim, "Chitosan composites for bone tissue engineering - An overview," *Mar. Drugs*, vol. 8, no. 8, pp. 2252–2266, 2010.

[40] R. A. Bhatt and T. D. Rozental, "Bone Graft Substitutes," *Hand Clin.*, vol. 28, no. 4, pp. 457–468, 2012.

[41] W. G. De Long *et al.*, "Bone grafts and bone graft substitutes in orthopaedic trauma surgery. A critical analysis.," *J. Bone Joint Surg. Am.*, vol. 89, pp. 649–658, 2007.

[42] P. Habibovic and K. de Groot, "Osteoinductive biomaterials – properties and relevance in bone repair.," *J. Tissue Eng. Regen. Med.*, vol. 1, no. 7, pp. 25–32, 2007.

[43] P. V. Giannoudis, H. Dinopoulos, and E. Tsiridis, "Bone substitutes: An update," *Injury*, vol. 36, no. 3, pp. S20–S27, 2005.

[44] N. I. M. H. Ill, J. G. E. H. Orne, and P. E. A. D. Evane, "Donor Site Morbidity in the Iliac Crest Bone Graft," *J. Surg.*, no. May, pp. 726–728, 1999.

[45] P. Habibovic *et al.*, "Comparative in vivo study of six hydroxyapatite-based bone graft substitutes," *J. Orthop. Res.*, vol. 26, no. 10, pp. 1363–1370, 2008.

[46] M. Erol and A. R. Boccaccini, "Nanoscaled bioactive glass particles and nanofibres," *Bioact. Glas. Mater. Prop. Appl.*, pp. 129–161, 2011.

[47] P. Feng, P. Wei, C. Shuai, and S. Peng, "Characterization of Mechanical and Biological Properties of 3-D Scaffolds Reinforced with Zinc Oxide for Bone Tissue Engineering," *Eur. Cytokine Netw.*, vol. 8, no. 1, pp. 37–43, 2014.

[48] I. Uysal, F. Severcan, A. Tezcaner, and Z. Evis, "Co-doping of hydroxyapatite with zinc and fluoride improves mechanical and biological properties of hydroxyapatite," *Prog. Nat. Sci. Mater. Int.*, vol. 24, no. 4, pp. 340–349, 2014.

[49] M. U. Munir *et al.*, "Hollow mesoporous hydroxyapatite nanostructures; smart nanocarriers with high drug loading and controlled releasing features," *Int. J. Pharm.*, vol. 544, no. 1, pp. 112–120, 2018.

[50] W. Qiao *et al.*, "Biomimetic hollow mesoporous hydroxyapatite microsphere with controlled morphology, entrapment efficiency and degradability for cancer therapy," *RSC Adv.*, vol. 7, no. 71, pp. 44788–44798, 2017.

[51] D. Arcos *et al.*, "Mesoporous bioactive glasses: Mechanical reinforcement by means of a biomimetic process," *Acta Biomater.*, vol. 7, no. 7, pp. 2952–2959, 2011.

[52] H. Zhou, Y. Yang, M. Yang, W. Wang, and Y. Bi, "Synthesis of mesoporous hydroxyapatite via a vitamin C templating hydrothermal route," *Mater. Lett.*, vol. 218, pp. 52–55, 2018.

[53] N. F. Mohammad, R. Othman, and F. Y. YEOH, "Controlling the pore characteristics of mesoporous apatite materials: Hydroxyapatite and carbonate apatite," *Ceram. Int.*, vol. 41, no. 9, pp. 10624–10633, 2015.

[54] F. Zeng *et al.*, "Preparation of pore expanded mesoporous hydroxyapatite via auxiliary solubilizing template method," *Colloids Surfaces A Physicochem. Eng. Asp.*, vol. 441, pp. 737–743, 2014.

[55] H. Liu, Y. Du, X. Wang, and L. Sun, “Chitosan kills bacteria through cell membrane damage,” *Int. J. Food Microbiol.*, vol. 95, no. 2, pp. 147–155, 2004.

[56] S. A. Sell, P. S. Wolfe, K. Garg, J. M. McCool, I. A. Rodriguez, and G. L. Bowlin, “The use of natural polymers in tissue engineering: A focus on electrospun extracellular matrix analogues,” *Polymers (Basel).*, vol. 2, no. 4, pp. 522–553, 2010.

[57] S. Jana, S. J. Florczyk, M. Leung, and M. Zhang, “High-strength pristine porous chitosan scaffolds for tissue engineering,” *J. Mater. Chem.*, vol. 22, no. 13, pp. 6291–6299, 2012.

[58] A. E. Machado, “Produção de Matrizes à Base de Quitosano para o Tratamento de Feridas,” FCT, 2014.

[59] M. Rodríguez-Vázquez, B. Vega-Ruiz, R. Ramos-Zúñiga, D. A. Saldaña-Koppel, L. F. Quiñones-Olvera, and Translational, “Chitosan and Its Potential Use as a Scaffold for Tissue Engineering in Regenerative Medicine,” *Biomed Res. Int.*, vol. 24, no. 3, pp. 121–143, 2015.

[60] A. Jain, A. Gulbake, S. Shilpi, A. Jain, P. Hurkat, and S. K. Jain, “A new horizon in modifications of chitosan: Syntheses and applications,” *Crit. Rev. Ther. Drug Carrier Syst.*, vol. 30, no. 2, pp. 91–181, 2013.

[61] S. a Kauffman and N. P. Group, “Heterotopic Bone formed in a Synthetic Sponge in the Skin of Young Pigs,” *© 1969 Nat. Publ. Gr.*, vol. 224, pp. 177–178, 1969.

[62] W. W. Thein-Han and R. D. K. Misra, “Biomimetic chitosan–nanohydroxyapatite composite scaffolds for bone tissue engineering,” *Acta Biomater.*, vol. 95, no. 2, pp. 147–155, 2008.

[63] Y. M. Khan, E. K. Cushnie, J. K. Kelleher, and C. T. Laurencin, “In situ synthesized ceramic-polymer composites for bone tissue engineering: Bioactivity and degradation studies,” *J. Mater. Sci.*, vol. 42, no. 12, pp. 4183–4190, 2007.

[64] D. Bellucci, A. Sola, and V. Cannillo, “Hydroxyapatite and tricalcium phosphate composites with bioactive glass as second phase: State of the art and current applications,” *J. Biomed. Mater. Res. - Part A*, vol. 104, no. 4, pp. 1030–1056, 2016.

[65] A. A. El-Rashidy, J. A. Roether, L. Harhaus, U. Kneser, and A. R. Boccaccini, “Regenerating bone with bioactive glass scaffolds: A review of in vivo studies in bone defect models,” *Acta Biomater.*, vol. 62, pp. 1–28, 2017.

[66] J. R. Jones, “Scaffolds for tissue engineering,” *Biomater. Artif. Organs Tissue Eng.*, pp. 201–214, 2005.

[67] V. Karageorgiou and D. Kaplan, “Porosity of 3D biomaterial scaffolds and osteogenesis,” *Biomaterials*, vol. 26, no. 27, pp. 5474–5491, 2005.

[68] S. Dorozhkin, “Self-Setting Calcium Orthophosphate Formulations,” *J. Funct. Biomater.*, vol. 4, no. 4, pp. 209–311, 2013.

[69] T. A. Russell and R. K. Leighton, “Comparison of Autogenous Bone Graft and Endothermic Calcium Phosphate Cement for Defect Augmentation in Tibial Plateau Fractures,” *J. Bone Jt. Surgery-American Vol.*, vol. 90, no. 10, pp. 2057–2061, 2008.

[70] H. Bae *et al.*, “A prospective randomized FDA-IDE trial comparing cortoss with PMMA for vertebroplasty: A comparative effectiveness research study with 24-month follow-up,” *Spine (Phila. Pa. 1976).*, vol. 37, no. 7, pp. 544–550, 2012.

[71] T. Lerner, V. Bullmann, T. L. Schulte, M. Schneider, and U. Liljenqvist, “A level-1 pilot study to evaluate of ultraporous β-tricalcium phosphate as a graft extender in the posterior correction of adolescent idiopathic scoliosis,” *Eur. Spine J.*, vol. 18, no. 2, pp. 170–179, 2009.

[72] C. J. Anker, S. P. Holdridge, B. Baird, H. Cohen, and T. A. Damron, “Ultraporous β-tricalcium phosphate is well incorporated in small cavitary defects,” *Clin. Orthop. Relat. Res.*, no. 434, pp. 251–257, 2005.

[73] V. Storybook, “Stryker Biologics The Gold Standard,” 2016.

[74] V. Bimodal, “The newest member of Increased calcium phosphate deposition with Vitoss BiModal *,” 2013.

[75] C. Cassidy *et al.*, “Norian SRS cement compared with conventional fixation in distal radial fractures. A randomized study.,” *J. Bone Joint Surg. Am.*, vol. 85-A, no. 11, pp. 2127–2137, 2003.

[76] N. E. Epstein, “High lumbar noninstrumented fusion rates using lamina autograft and Nanoss/bone marrow aspirate Nancy,” *Surg. Neurol. Int.*, vol. 8, pp. 1–7, 2017.

[77] N. E. Epstein, “Preliminary documentation of the comparable efficacy of vitoss versus NanOss bioactive as bone graft expanders for posterior cervical fusion,” *Surg. Neurol. Int.*, vol. 6, no. 5, p. 164, 2015.

[78] T. Kokubo and H. Takadama, “How useful is SBF in predicting in vivo bone bioactivity?,” *Biomaterials*, vol. 27, no. 15, pp. 2907–2915, 2006.

[79] X. Yan, C. Yu, X. Zhou, J. Tang, and D. Zhao, “Highly ordered mesoporous bioactive glasses with superior in vitro bone-forming bioactivities,” *Angew. Chemie - Int. Ed.*, vol. 43, no. 44, pp. 5980–5984, 2004.

[80] M. H. Fathi and A. Hanifi, “Evaluation and characterization of nanostructure hydroxyapatite powder prepared by simple sol-gel method,” *Mater. Lett.*, vol. 61, no. 18, pp. 3978–3983, 2007.

[81] C. C. Leffler and B. W. Müller, “Influence of the acid type on the physical and drug liberation properties of chitosan-gelatin sponges,” *Int. J. Pharm.*, vol. 194, no. 2, pp. 229–237, 2000.

[82] S. T. Ho and D. W. Hutmacher, “A comparison of micro CT with other techniques used in the characterization of scaffolds,” *Biomaterials*, vol. 27, no. 8, pp. 1362–1376, 2006.

[83] M. Tamplenizza *et al.*, “In vivo imaging study of angiogenesis in a channelized porous scaffold,” *Mol. Imaging*, vol. 14, no. 4, 2015.

[84] R. C. Davies, A. Neuberger, and B. M. Wilson, “The dependence of lysozyme activity on pH and ionic strength,” *BBA - Enzymol.*, vol. 178, no. 2, pp. 294–305, 1969.

[85] T. Freier, H. S. Koh, K. Kazazian, and M. S. Shoichet, “Controlling cell adhesion and degradation of chitosan films by N-acetylation,” *Biomaterials*, vol. 26, no. 29, pp. 5872–5878, 2005.

[86] H. Sashiwa, H. Saimoto, Y. Shigemasa, R. Ogawa, and S. Tokura, “Lysozyme susceptibility of partially deacetylated chitin,” *Int. J. Biol. Macromol.*, vol. 12, no. 5, pp. 295–296, 1990.

[87] M. Peter *et al.*, “Nanocomposite scaffolds of bioactive glass ceramic nanoparticles disseminated chitosan matrix for tissue engineering applications,” *Carbohydr. Polym.*, vol. 79, no. 2, pp. 284–289, 2010.

[88] F. L. A. do Carmo, “Study on production methods of Bioglass Porous Structures for Bone Tissue Engineering,” FCT, 2018.

[89] S. Prata, “Desenvolvimento de novos implantes biocompatíveis para a regeneração óssea,” 2012.

[90] R. M. De Almeida, “Hydroxyapatite Porous Structures for Bone Tissue Engineering,” FCT, 2014.

[91] C. J. Shih, H. T. Chen, L. F. Huang, P. S. Lu, H. F. Chang, and I. L. Chang, “Synthesis and in vitro bioactivity of mesoporous bioactive glass scaffolds,” *Mater. Sci. Eng. C*, vol. 30, no. 5, pp. 657–

663, 2010.

[92] S. Mondal, B. Mondal, A. Dey, and S. S. Mukhopadhyay, “Studies on Processing and Characterization of Hydroxyapatite Biomaterials from Different Bio Wastes,” *J. Miner. Mater. Charact. Eng.*, vol. 11, no. 01, pp. 55–67, 2012.

[93] L. Pighinelli and M. Kucharska, “Properties and Structure of Microcrystalline Chitosan and Hydroxyapatite Composites,” *J. Biomater. Nanobiotechnol.*, vol. 05, no. 02, pp. 128–138, 2014.

[94] P. Q. Franco, “Produção de Fibras de Hidroxiapatite por Electrofiação,” UNIVERSIDADE NOVA DE LISBOA, Faculdade de Ciências e Tecnologia, 2009.

[95] D. dos S. TAVARES, L. de O. CASTRO, G. D. de A. SOARES, G. G. ALVES, and J. M. GRANJEIRO, “Synthesis and cytotoxicity evaluation of granular magnesium substituted β-tricalcium phosphate,” *J. Appl. Oral Sci.*, vol. 21, no. 1, pp. 37–42, Feb. 2013.

[96] A. El-Fiqi *et al.*, “Capacity of mesoporous bioactive glass nanoparticles to deliver therapeutic molecules,” *Nanoscale*, vol. 4, no. 23, pp. 7475–7488, 2012.

[97] G. E. Stan *et al.*, “Highly adherent bioactive glass thin films synthetized by magnetron sputtering at low temperature,” *J. Mater. Sci. Mater. Med.*, vol. 22, no. 12, pp. 2693–2710, 2011.

[98] M. F. Queiroz, K. R. T. Melo, D. A. Sabry, G. L. Sassaki, and H. A. O. Rocha, “Does the use of chitosan contribute to oxalate kidney stone formation?,” *Mar. Drugs*, vol. 13, no. 1, pp. 141–158, 2015.

[99] A. Molaei, M. Yari, and M. R. Afshar, “Modification of electrophoretic deposition of chitosan–bioactive glass–hydroxyapatite nanocomposite coatings for orthopedic applications by changing voltage and deposition time,” *Ceram. Int.*, vol. 41, no. 10, pp. 14537–14544, 2015.

[100] C. R. Correia *et al.*, “Chitosan Scaffolds Containing Hyaluronic Acid for Cartilage Tissue Engineering,” *Tissue Eng. Part C Methods*, vol. 17, no. 7, pp. 717–730, Jul. 2011.

[101] H. F. Song *et al.*, “Preparation of chitosan-based hemostatic sponges by supercritical fluid technology,” *Materials (Basel).*, vol. 7, no. 4, pp. 2459–2473, 2014.

[102] S. Waheed, M. Sultan, T. Jamil, and T. Hussain, *Comparative Analysis of Hydroxyapatite Synthesized by Sol-gel, Ultrasonication and Microwave Assisted Technique*, vol. 2, no. 10. Elsevier Ltd., 2015.

[103] X. X. Yan *et al.*, “Mesoporous bioactive glasses. I. Synthesis and structural characterization,” *J. Non. Cryst. Solids*, vol. 351, no. 40–42, pp. 3209–3217, 2005.

[104] O. H. Ojeda-Niño, C. Blanco, and C. E. Daza, “High temperature CO2 capture of hydroxyapatite extracted from tilapia scales,” *Univ. Sci.*, vol. 22, no. 3, pp. 215–236, 2017.

[105] JCPDS, *Card No. 9-0432*. 2001.

[106] A. López-Noriega, D. Arcos, I. Izquierdo-Barba, Y. Sakamoto, O. Terasaki, and M. Vallet-Regí, “Ordered mesoporous bioactive glasses for bone tissue regeneration,” *Chem. Mater.*, vol. 18, no. 13, pp. 3137–3144, 2006.

[107] C. Yu, J. Fan, B. Tian, G. D. Stucky, and D. Zhao, “Synthesis of mesoporous silica from commercial poly(ethylene oxide)/poly(butylene oxide) copolymers: Toward the rational design of ordered mesoporous materials,” *J. Phys. Chem. B*, vol. 107, no. 48, pp. 13368–13375, 2003.

[108] X. Yan *et al.*, “The in-vitro bioactivity of mesoporous bioactive glasses,” *Biomaterials*, vol. 27, no. 18, pp. 3396–3403, 2006.

[109] C. H. Ahn, B. Anczykowski, M. Z. Atashbar, W. Bacsa, W. S. Bainbridge, and A. Baldi, *Springer*

Handbook of Nanotechnology. 2007.

[110] I. Standard, “ISO 10993-5,” 2009.

[111] M. Mozafari, F. Moztarzadeh, and M. Tahriri, “Investigation of the physico-chemical reactivity of a mesoporous bioactive SiO2-CaO-P2O5 glass in simulated body fluid,” *J. Non. Cryst. Solids*, vol. 356, no. 28–30, pp. 1470–1478, 2010.

[112] P. X. Ma and J. Choi, “Biodegradable Polymer Scaffolds with Well-Defined Interconnected Spherical Pore Network,” *Tissue Eng.*, vol. 7, no. 1, pp. 23–33, Feb. 2001.

[113] Q. L. Loh and C. Choong, “Three-dimensional scaffolds for tissue engineering applications: Role of porosity and pore size,” *Tissue Eng. - Part B Rev.*, vol. 19, no. 6, pp. 485–502, 2013.

[114] N. Thadavirul, P. Pavasant, and P. Supaphol, “Improvement of dual-leached polycaprolactone porous scaffolds by incorporating with hydroxyapatite for bone tissue regeneration,” *J. Biomater. Sci. Polym. Ed.*, vol. 25, no. 17, pp. 1986–2008, 2014.

[115] J. Chen, P. Pan, Y. Zhang, S. Zhong, and Q. Zhang, “Preparation of chitosan/nano hydroxyapatite organic–inorganic hybrid microspheres for bone repair,” *Colloids Surfaces B Biointerfaces*, vol. 134, pp. 401–407, Oct. 2015.

[116] M. M. Mecwan, G. E. Rapalo, S. R. Mishra, W. O. Haggard, and J. D. Bumgardner, “Effect of molecular weight of chitosan degraded by microwave irradiation on lyophilized scaffold for bone tissue engineering applications,” *J. Biomed. Mater. Res. - Part A*, vol. 97 A, no. 1, pp. 66–73, 2011.

[117] M. Peter, N. S. Binulal, S. V. Nair, N. Selvamurugan, H. Tamura, and R. Jayakumar, “Novel biodegradable chitosan–gelatin/nano-bioactive glass ceramic composite scaffolds for alveolar bone tissue engineering,” *Chem. Eng. J.*, vol. 158, no. 2, pp. 353–361, Apr. 2010.

[118] M. Peter, P. T. Sudheesh Kumar, N. S. Binulal, S. V. Nair, H. Tamura, and R. Jayakumar, “Development of novel α-chitin/nanobioactive glass ceramic composite scaffolds for tissue engineering applications,” *Carbohydr. Polym.*, vol. 78, no. 4, pp. 926–931, 2009.

[119] P. Gentile *et al.*, “Bioactive glass/polymer composite scaffolds mimicking bone tissue,” *J. Biomed. Mater. Res. - Part A*, vol. 100 A, no. 10, pp. 2654–2667, 2012.

[120] V. Maquet, A. R. Boccaccini, L. Pravata, I. Notingher, and R. Jérôme, “Preparation, characterization, and in vitro degradation of bioresorbable and bioactive composites based on Bioglass®-filled polylactide foams,” *J. Biomed. Mater. Res. - Part A*, vol. 66, no. 2, pp. 335–346, 2003.

[121] B. Gaihre and A. C. Jayasuriya, “Comparative investigation of porous nano-hydroxyapaptite/chitosan, nano-zirconia/chitosan and novel nano-calcium zirconate/chitosan composite scaffolds for their potential applications in bone regeneration,” *Mater. Sci. Eng. C*, vol. 91, no. May, pp. 330–339, Oct. 2018.

[122] M. Peter, N. S. Binulal, S. V. Nair, N. Selvamurugan, H. Tamura, and R. Jayakumar, “Novel biodegradable chitosan-gelatin/nano-bioactive glass ceramic composite scaffolds for alveolar bone tissue engineering,” *Chem. Eng. J.*, vol. 158, no. 2, pp. 353–361, 2010.

[123] B. P. Kanungo, E. Silva, K. Van Vliet, and L. J. Gibson, “Characterization of mineralized collagen-glycosaminoglycan scaffolds for bone regeneration,” *Acta Biomater.*, vol. 4, no. 3, pp. 490–503, 2008.

[124] A. Roi, L. C. Ardelean, C. I. Roi, E. Boia, S. Boia, and L. Rusu, “Oral Bone Tissue Engineering : Advanced Biomaterials for Cell Adhesion , Proliferation and Di ff erentiation,” pp. 1–16.

[125] W. M. Kulicke and R. Kniewske, “The shear viscosity dependence on concentration, molecular

weight, and shear rate of polystyrene solutions," *Rheol. Acta*, vol. 23, no. 1, pp. 75–83, 1984.

[126] A. Lončarević, M. Ivanković, A. Rogina, M. Ivanković or Opalički, and A. Rogina, "Lysozyme-Induced Degradation of Chitosan: The Characterisation of Degraded Chitosan Scaffolds," *J. Tissue Repair Regen.*, vol. 1, no. 1, Dec. 2017.

[127] T. Han, N. Nwe, T. Furuike, S. Tokura, and H. Tamura, "Methods of N-acetylated chitosan scaffolds and its in vitro biodegradation by lysozyme," *J. Biomed. Sci. Eng.*, vol. 05, no. 01, pp. 15–23, 2012.

[128] D. Ren, H. Yi, W. Wang, and X. Ma, "The enzymatic degradation and swelling properties of chitosan matrices with different degrees of N-acetylation," *Carbohydr. Res.*, vol. 340, no. 15, pp. 2403–2410, 2005.

[129] L. L. Hench, R. J. Splinter, W. C. Allen, and T. K. Greenlee, "Bonding mechanisms at the interface of ceramic prosthetic materials," *J. Biomed. Mater. Res.*, vol. 5, no. 6, pp. 117–141, 1971.

[130] T. Valente, J. L. Ferreira, C. Henriques, J. P. Borges, and J. C. Silva, "Polymer blending or fiber blending: A comparative study using chitosan and poly(ε-caprolactone) electrospun fibers," *J. Appl. Polym. Sci.*, vol. 136, no. 11, pp. 1–11, 2019.

[131] S. V. Dorozhkin, "Calcium orthophosphate bioceramics," *Eurasian Chem. J.*, vol. 12, no. 3–4, pp. 247–258, 2010.

[132] E. Bayrak and P. Yilgor Huri, "Engineering Musculoskeletal Tissue Interfaces," *Front. Mater.*, vol. 5, no. April, pp. 1–8, 2018.

[133] K. R. Mohamed, H. H. Beherei, and Z. M. El-Rashidy, "In vitro study of nano-hydroxyapatite/chitosan-gelatin composites for bio-applications," *J. Adv. Res.*, vol. 5, no. 2, pp. 201–208, 2014.

[134] Y. Li, D. Li, and W. Weng, "Preparation of nano carbonate-substituted hydroxyapatite from an amorphous precursor," *Int. J. Appl. Ceram. Technol.*, vol. 5, no. 5, pp. 442–448, 2008.

[135] H. Benhayoune *et al.*, "A new sol–gel synthesis of 45S5 bioactive glass using an organic acid as catalyst," *Mater. Sci. Eng.*, vol. 47, pp. 407–412, 2014.

Appendix

Appendix I

Table A. 1 - Bone grafting materials used for bone repair and regeneration: examples, advantages and disadvantages.

Bone grafting materials		Examples	Advantages	Disadvantages	References
Polymers	Natural	Protein: collagen, fibrin, gelatin, silk fibroin Polysaccharides: hyaluronic acid, chondroitin sulphate, cellulose, starch, alginate, agarose, chitosan, pullulan, dextran	Biodegradability Biocompatibility Bioactivity Unlimited source (some of them)	Low mechanical strength High rates of degradation High batch to batch variations	[8], [12], [16], [43], [57], [67]
	Synthetic	PGA PLA PCL PLGA poly-HEMA	Biodegradability Biocompatibility Versatility Hight tensile modulus	Low mechanical strength High local concentration of acidic degradation products	[8], [12], [16], [43], [66], [67]
Ceramics	Calcium-phosphate (CaP)	Coralline or synthetic HA Silicate-substituted HA (β-TCP) Dicalcium phosphate dehydrate (DCPD)	Biocompatibility Biodegradability Bioactivity Osteoconductivity Osteoinductivity Antibacterial properties (Bioglasses)	Brittleness Low fracture strength Degradation rates difficult to predict	[8], [16], [37], [41], [43], [66]–[68], [131]
	Bioglasses and glass-ceramics	Silicate bioactive glasses (45S5, 13-93) Borate/borosilicate bioactive glasses (13-93B2, 13-93B3, Pyrex®)			[8], [43], [46], [66], [67]
Metals		Titanium and its alloys Tantalum Stainless Steel Magnesium and its alloys Cobalt–chromium alloys	Excellent mechanical properties (high strength and wear resistance, ductility) Biocompatibility	Lack of tissue adherence Corrosion Risk of toxicity due to release of metal ions	[8], [16], [67]
Composites		Calcium-phosphate coatings on metals HA/poly-(D,L-lactide) HA/chitosan-gelatin Alumina ceramic (Al_2O_3)	Combination of the above	Combination of the above	[8], [43], [66], [132], [133]

Appendix II

Table A. 2 - Assignment of Hap with (MHAp) and without F127 (nHAp) FTIR spectra bands. [62], [93], [94], [97], [134]

Wavenumber (cm^{-1})		Description
Hap without F127	Hap with F127	
3556	3570	v (OH^-) stretching mode
3479	3475	
3446		
2989	2997	
1622	1637	v_2(H–O–H) bending mode
1419	1414	$v_3(CO_3^{2-})$ asymmetric stretching mode
1452	1456	
1367		v(NO_3^-) stretching mode
1348	1333	
1115	1116	$v_3'(PO_4^{3-})$ asymmetric stretching mode
1020	1020	$v_3(PO_4^{3-})$ asymmetric stretching mode
958	960	$v_1(PO_4^{3-})$ symmetric stretching mode
924	928	
872	879	$v_2(CO_3^{2-})$ asymmetric bending mode
814	814	
742	746	
600	600	$v_4(PO_4^{3-})$ asymmetric bending mode
559	561	

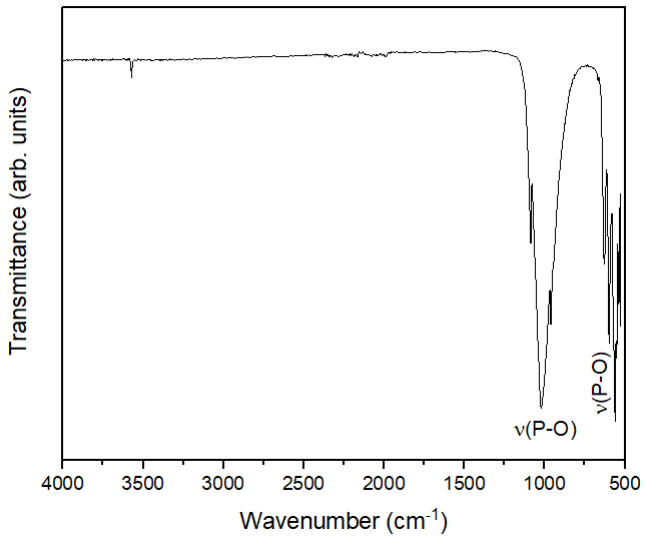

Figure A. 1 - FTIR of FR.

Table A. 3 - Assignment of MBG FTIR spectra bands. [51], [91], [97], [135]

Wavenumber (cm^{-1})	Description
3375	v(OH^-) stretching mode
2983 - 2880	-CH_2- bending and stretching vibrations
1433 -1246	-CH_2- bending and stretching vibrations
1150	Si–O–Si asymmetric stretching
1032	Si–O Q^2 and Q^3 units
947	Si–O Q^1 and Q^2 units
820 - 780	Si–O–Si symmetric stretching or vibration modes
569	Si–O–Si bending mode

Table A. 4 - Assignment of CHH and CHL FTIR spectra bands. [62], [98]–[100]

Wavenumber (cm^{-1})		Description
CHH	CHL	
3354 - 3292	3344 - 3278	v(N-H) and v(OH^-) stretching mode
2868	2866	C-H asymmetric stretching
1645	1637	v(-C=O-) stretching mode of Amide I
1583	1579	δ(N-H) bending of the primary Amine
1421	1425	δ(C-H) bending
1373	1371	CH_3 symmetrical deformations
1313	1309	v(-C=O-) stretching mode of Amide III
1149	1149	v(C-O-C) asymmetric stretching
1057 - 1022	1065 - 1016	v(C-O-C) symmetric and asymmetric stretching of ester band
889	887	δ(C-H) bending vibration
658	617	δ(O-H) bending vibration

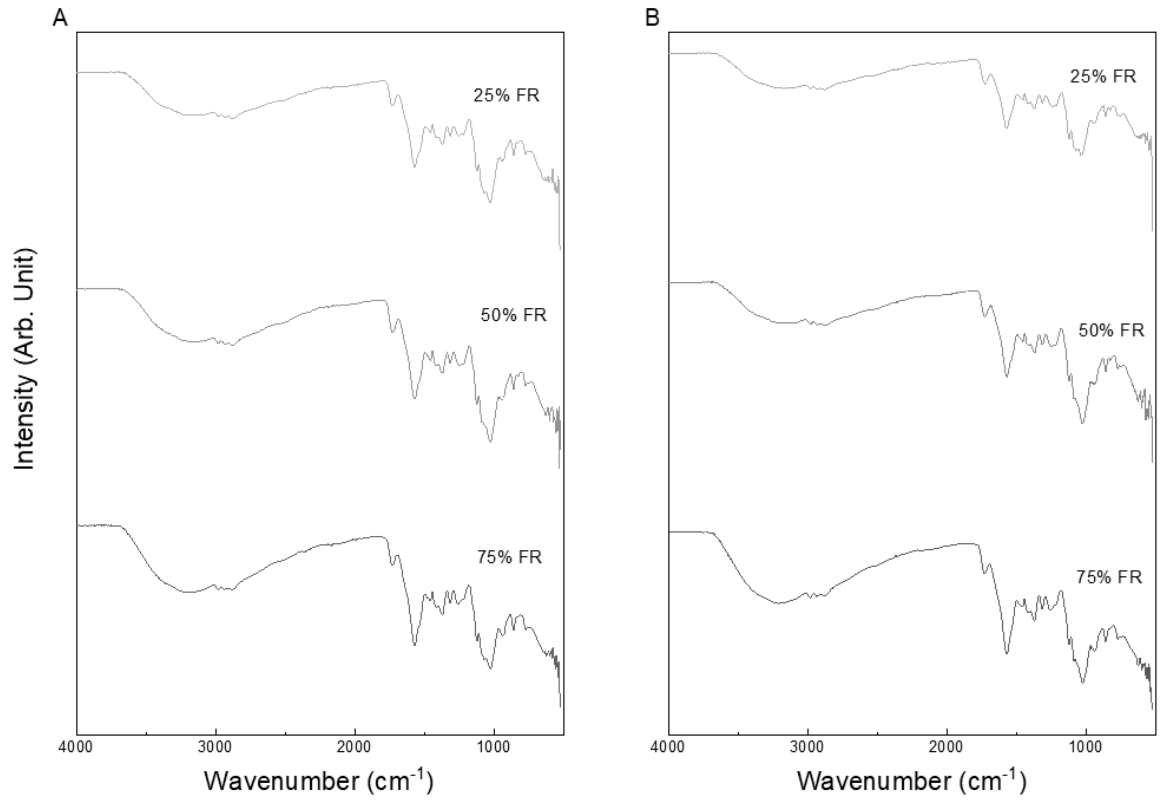

Figure A. 2 - FTIR of FR composite scaffolds with CHL (A) and CHH (B).

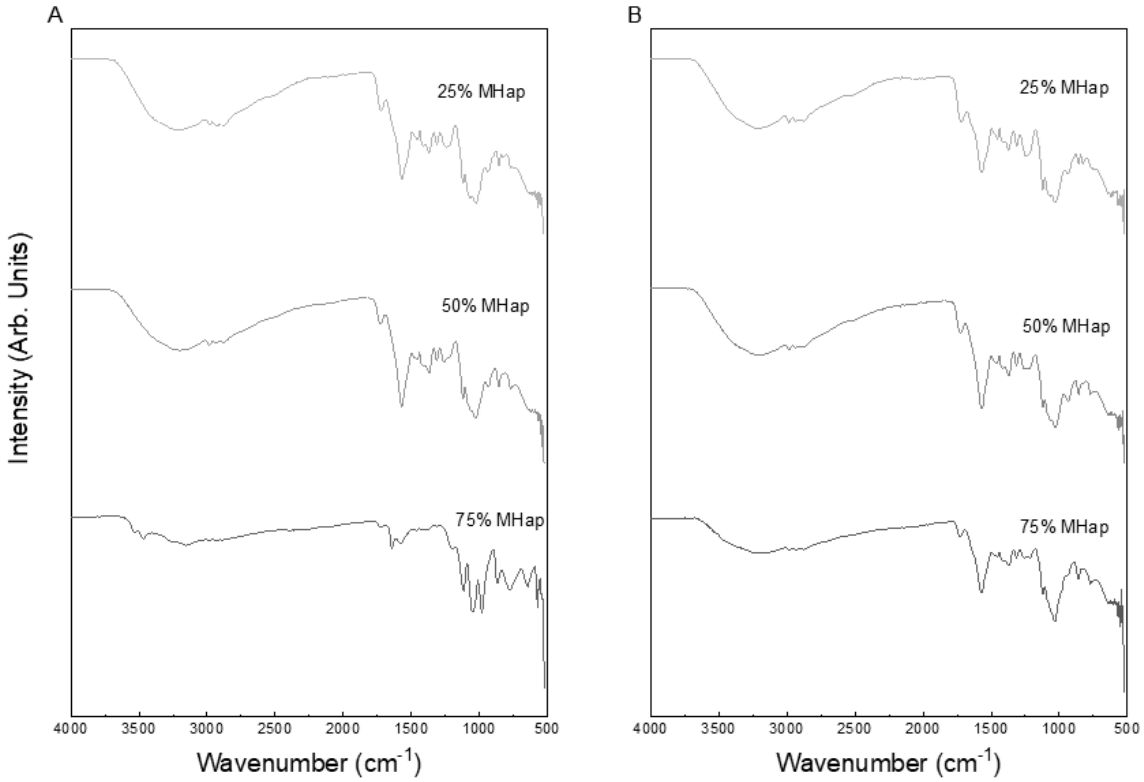

Figure A. 3 - FTIR of MHAp composite scaffolds with CHL (A) and CHH (B).

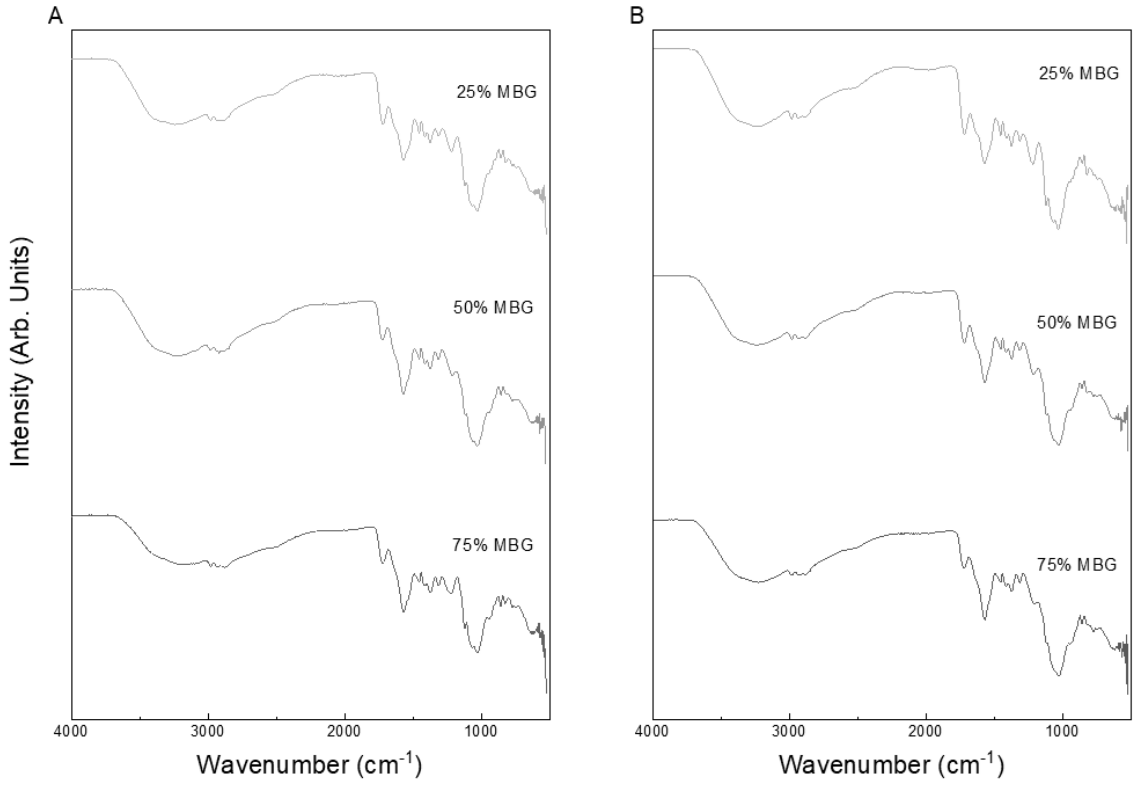

Figure A. 4 - FTIR of MBG composite scaffolds with CHL (A) and CHH (B).

Appendix III

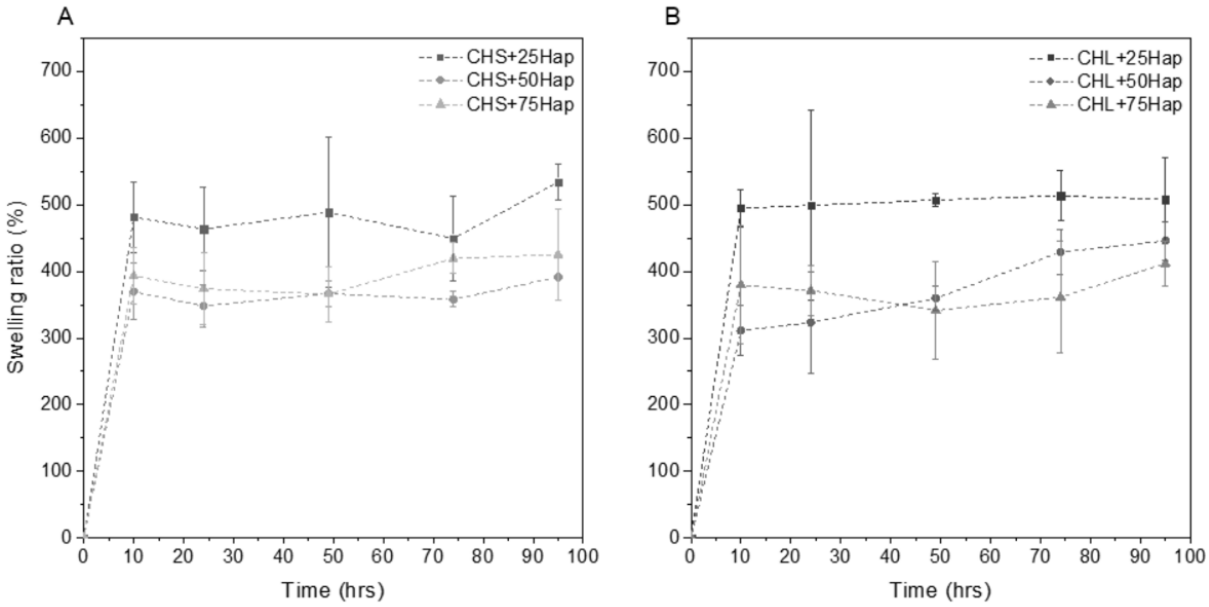

Figure A. 5 - Swelling ratio of FR composites with CHL (A) and CHH (B). Data obtained from a sample of three replicas for plot point.

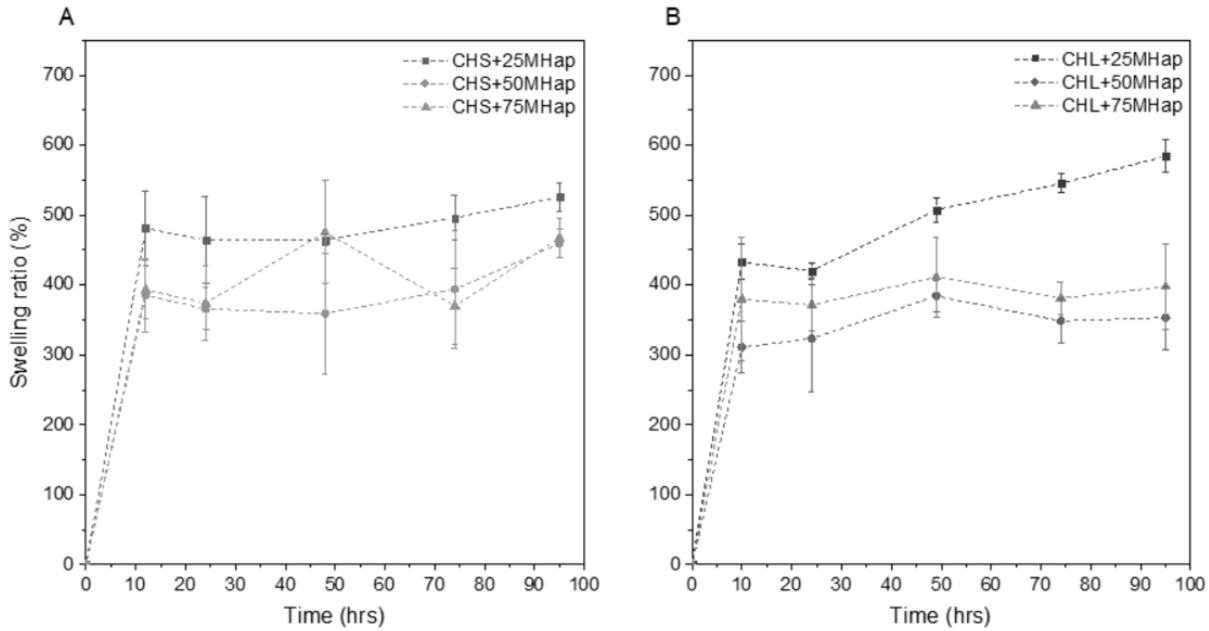

Figure A. 6 - Swelling ratio of MHAp composites with CHL (A) and CHH (B). Data obtained from a sample of three replicas for plot point.

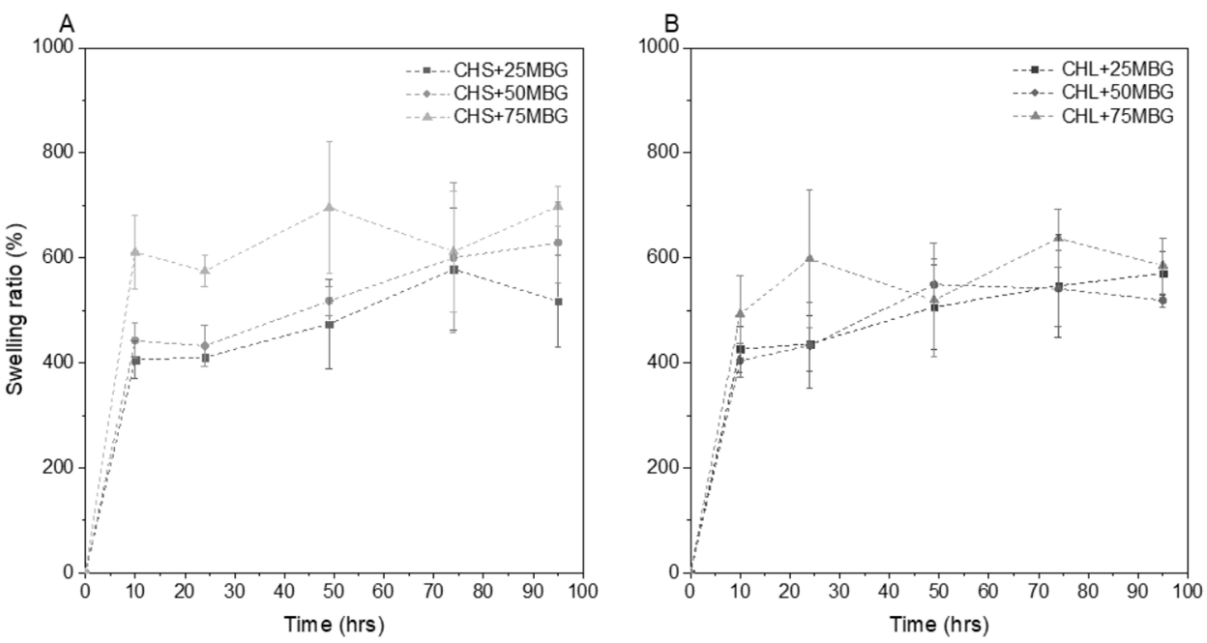

Figure A. 7 - Swelling ratio of MBG composites with CHL (A) and CHH (B). Data obtained from a sample of three replicas for plot point.

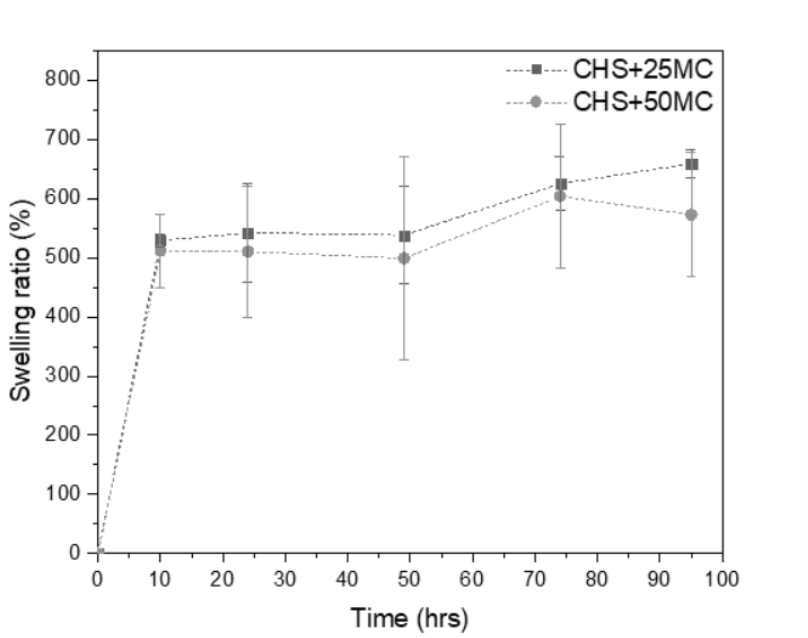

Figure A. 8 - Swelling ratio of mesoporous composite (MHAp and MBG) with CHL. Data obtained from a sample of three replicas for plot point.

Appendix IV

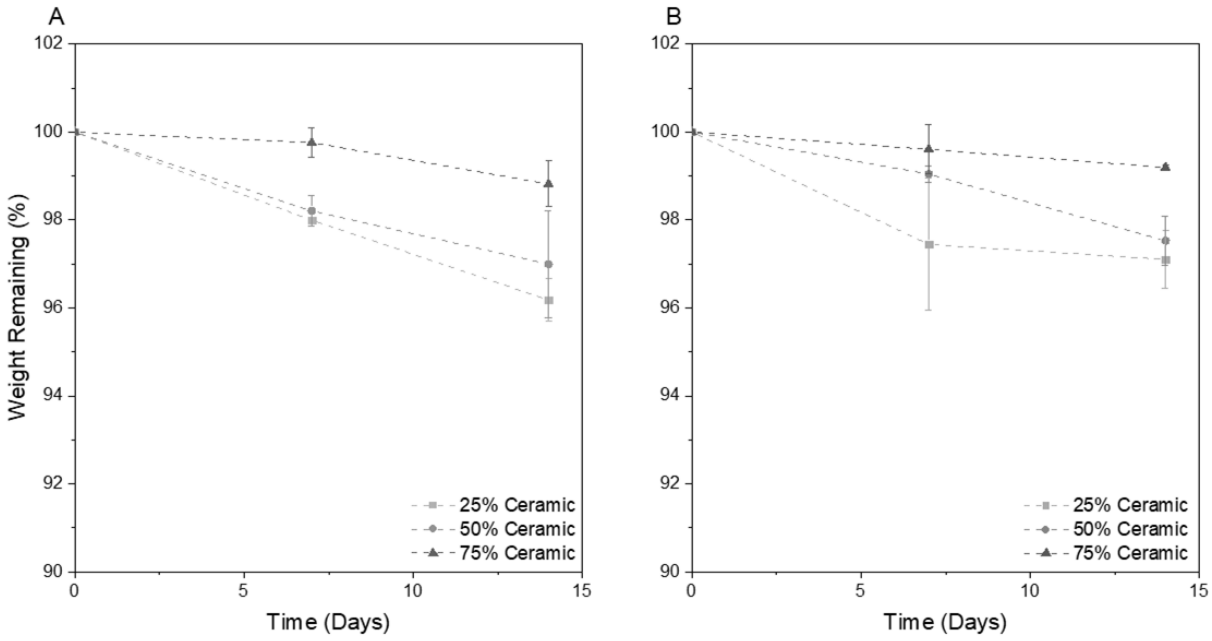

Figure A. 9 – Degradation behavior of FR composites with CHL (A) and CHH (B). Data obtained from a sample of three replicas for plot point.

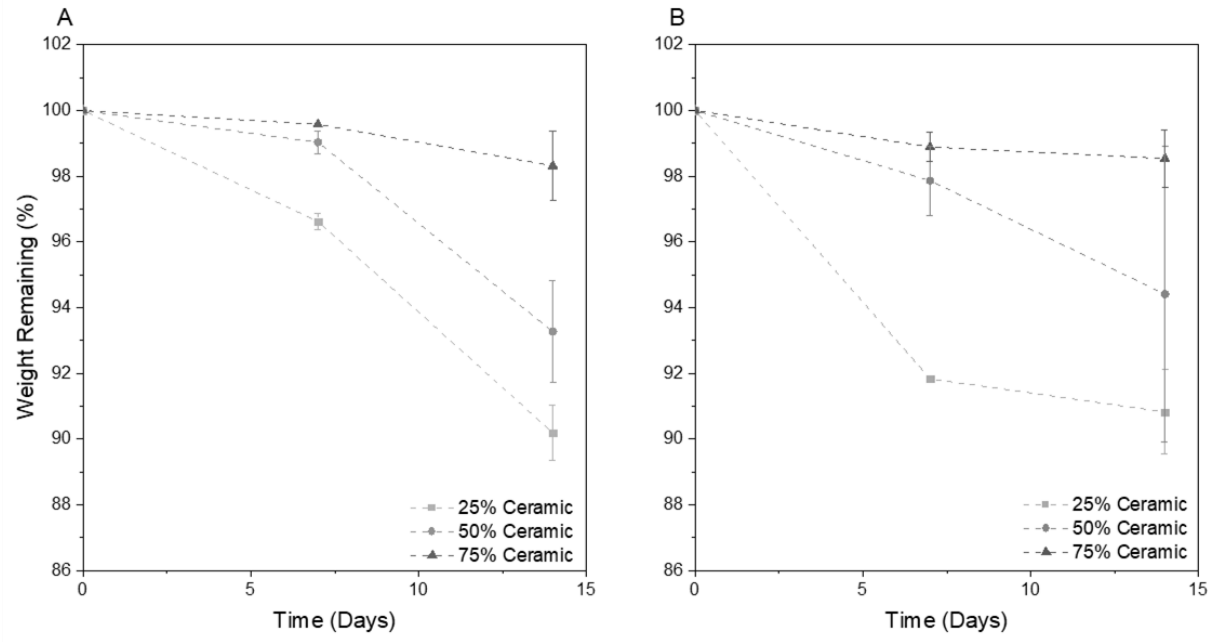

Figure A. 10 - Degradation behavior of MHAp composites with CHL (A) and CHH (B). Data obtained from a sample of three replicas for plot point.

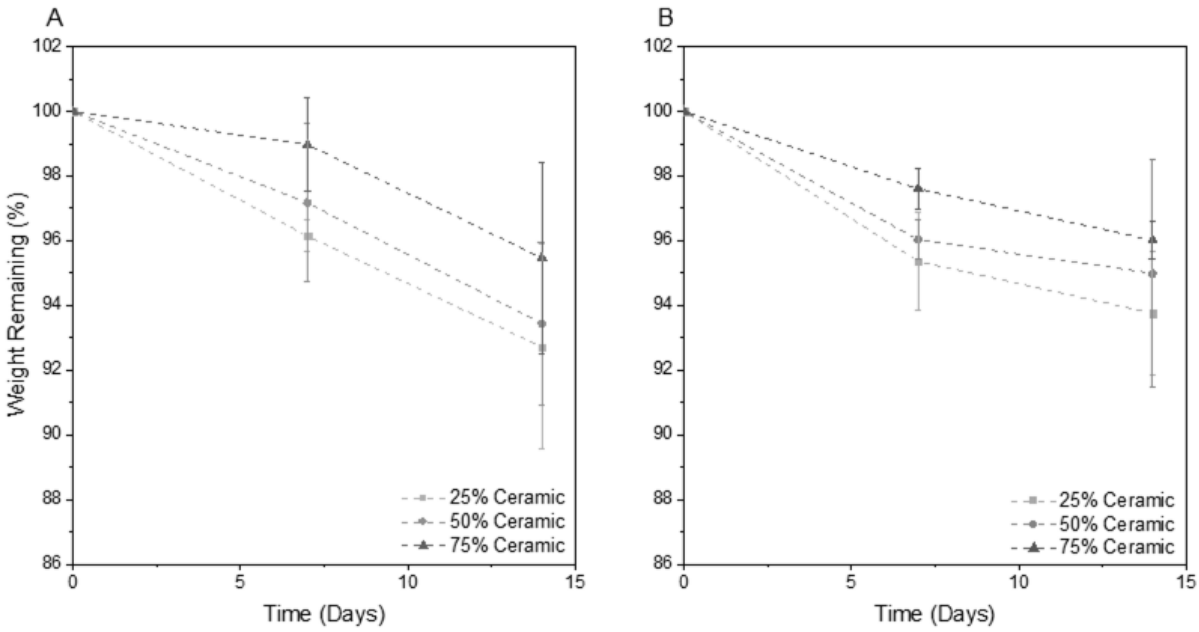

Figure A. 11 - Degradation behavior of MBG composites with CHL (A) and CHH (B). Data obtained from a sample of three replicas for plot point.

Appendix V

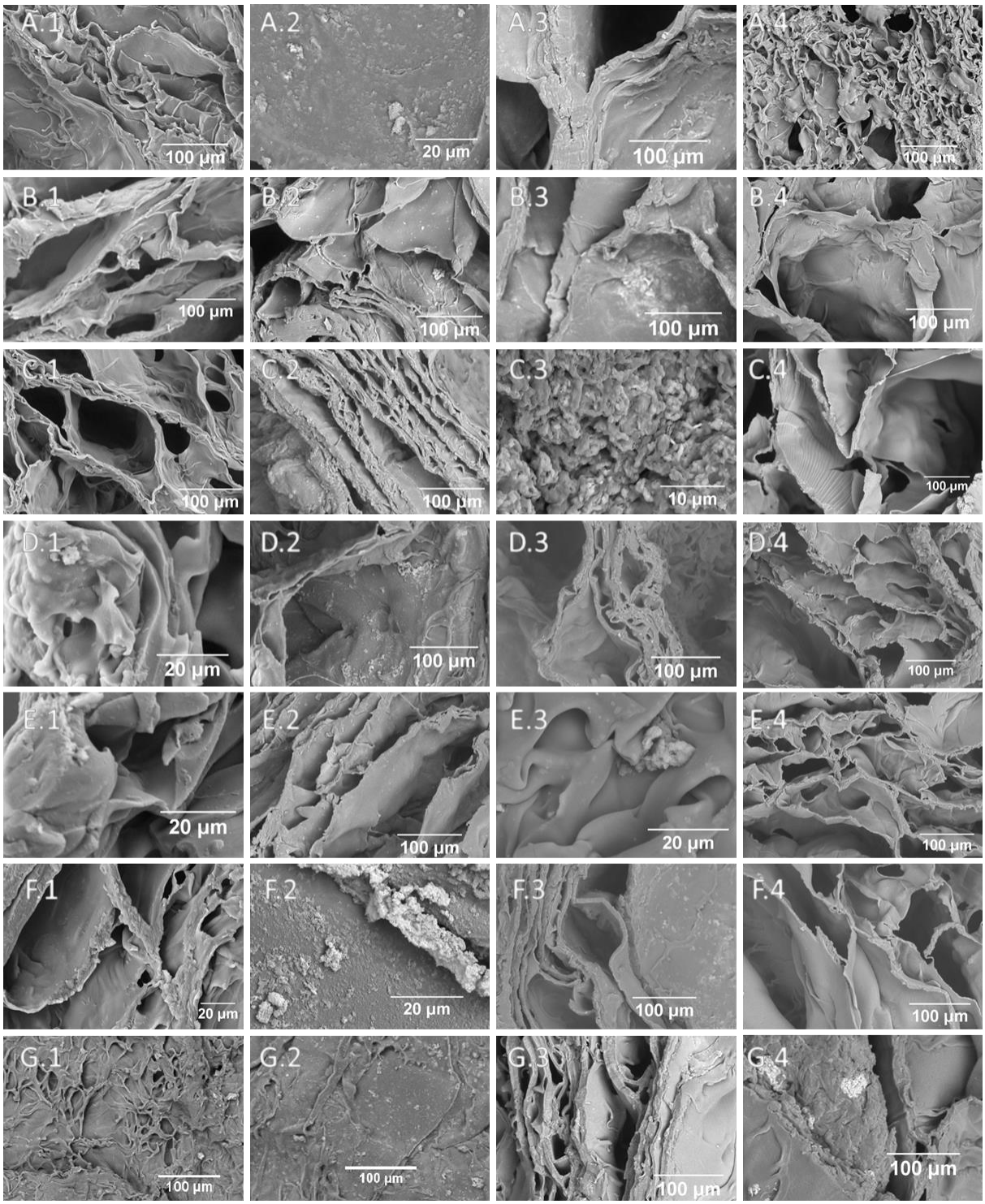

Figure A. 12 - SEM images of the CHH membranes (1), CHH+25%FR (2), CHH+24%MHAp (3) and CHH+25%MBG (4) after immersion in SBF for 3h (A), 6h (B), 12h (C), 24h (D), 48h (E), 72h (F) and 7days (G).

Appendix VI

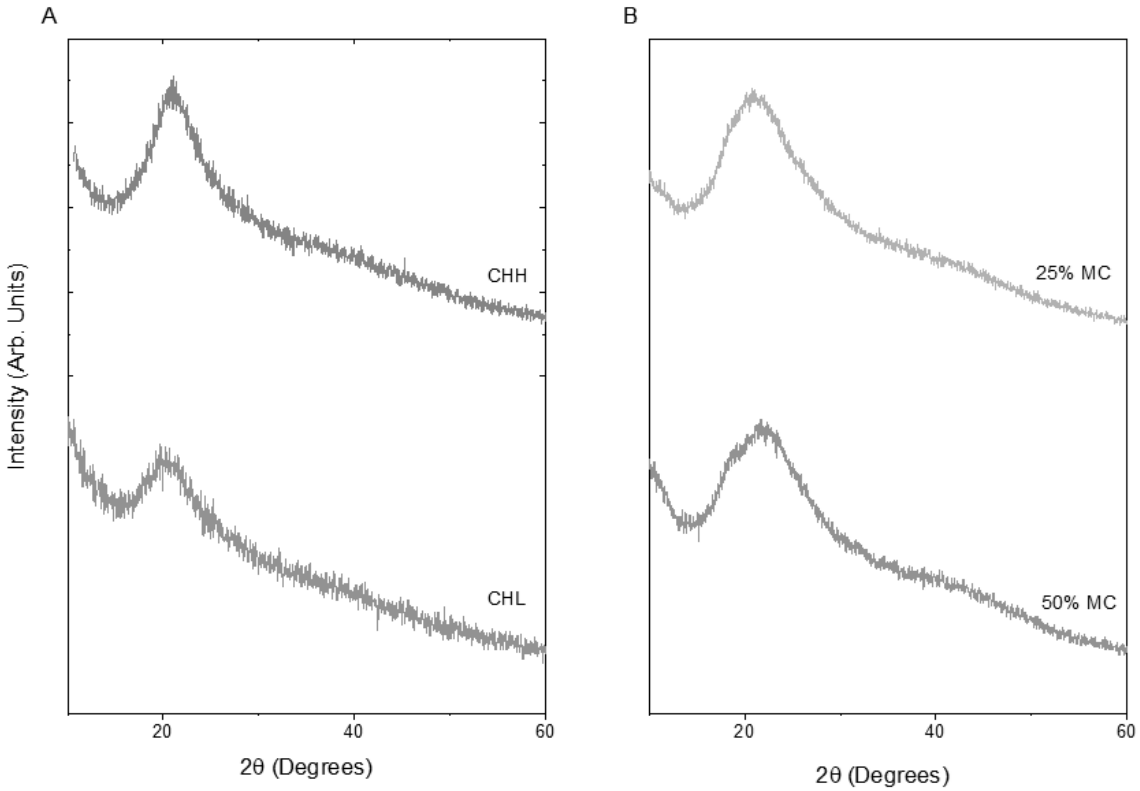

Figure A. 13 - XRD diffractograms of the polymeric membranes (A) and of mesoporous membranes with CHL (B) in different concentrations.

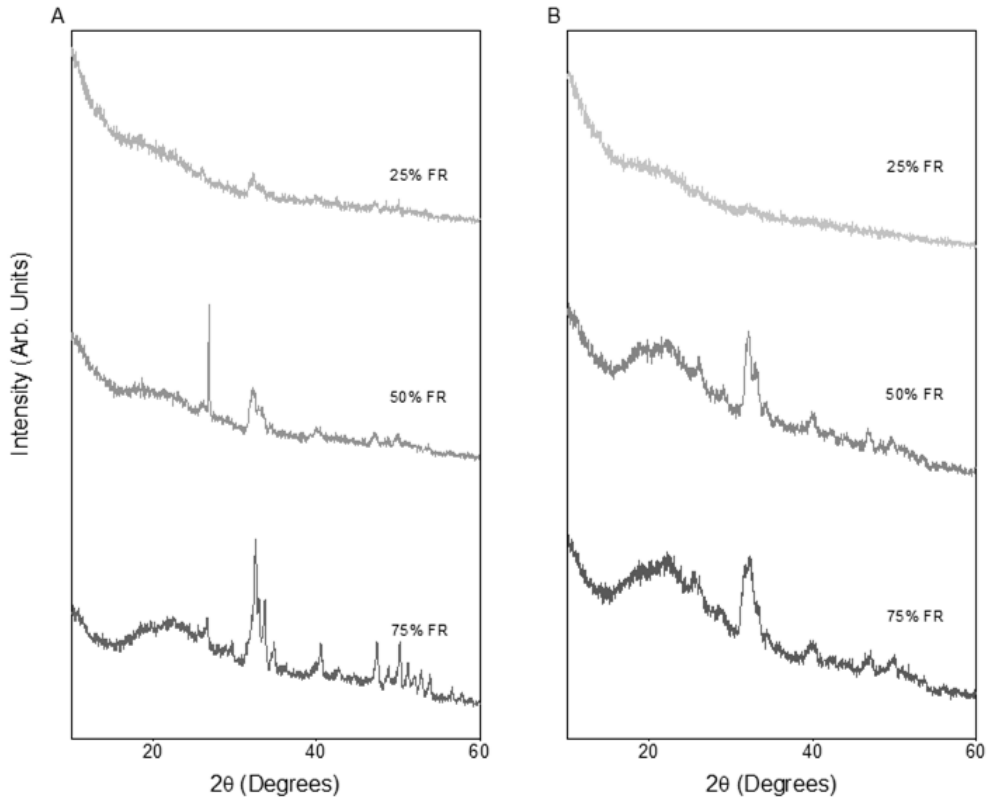

Figure A. 14 - XRD diffractograms of composite membranes of FR in different concentrations with CHL (A) and CHH (B).

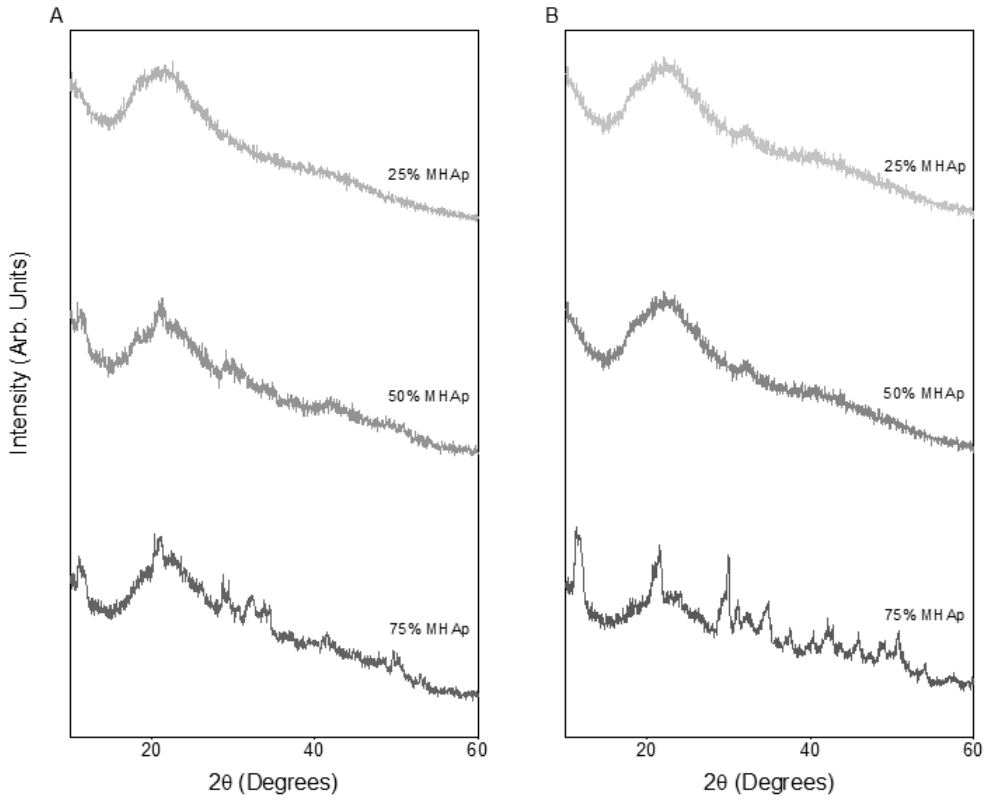

Figure A. 15 - XRD diffractograms of composite membranes of MHAp in different concentrations with CHL (A) and CHH (B).

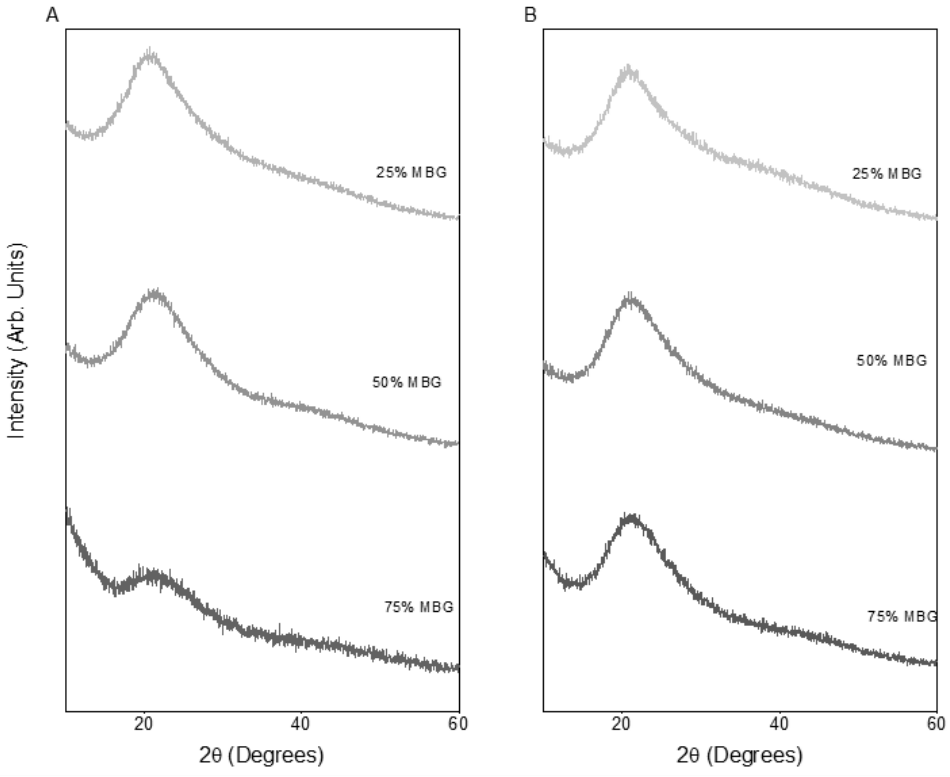

Figure A. 16 - XRD diffractograms of composite membranes of MBG in different concentrations with CHL (A) and CHH (B).

Appendix VII

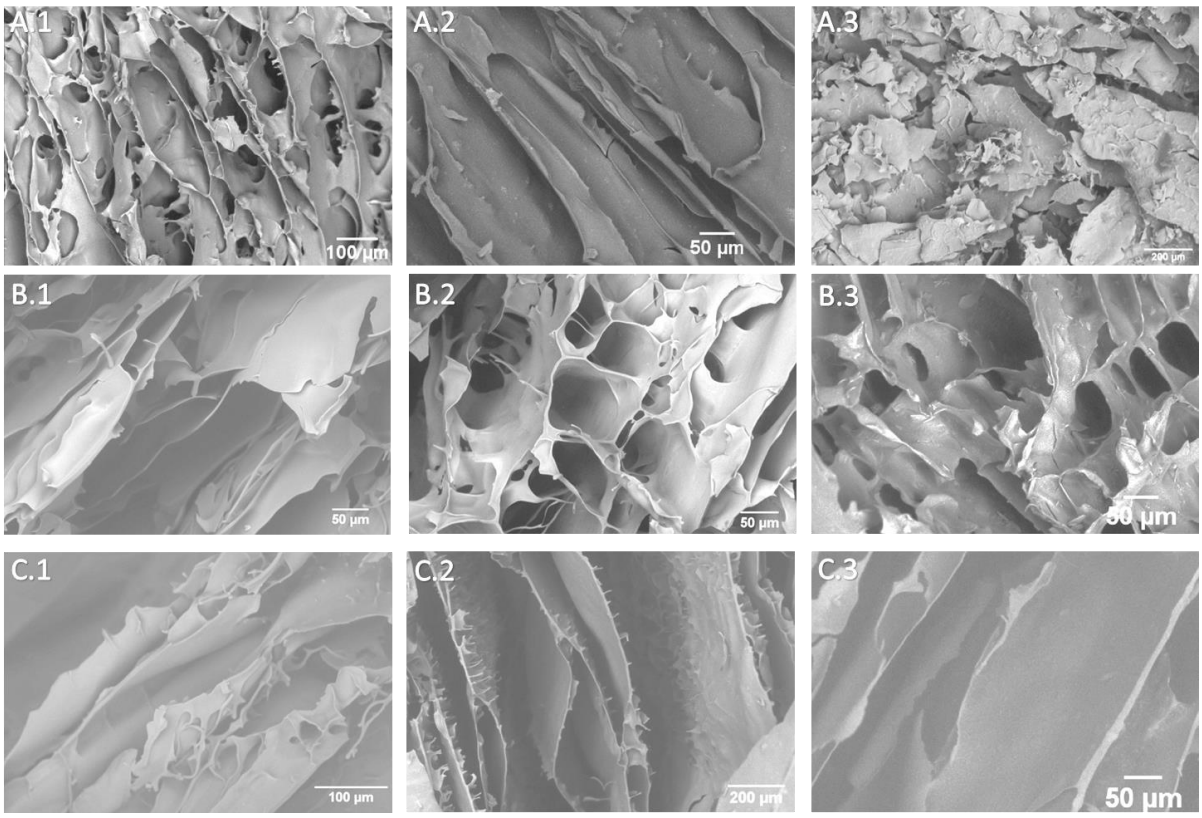

Figure A. 17 - SEM images of CHH composites with FR (1), MHAp (2) and MBG with different concentrations: 25% (A), 50% (B) and 75% (C).

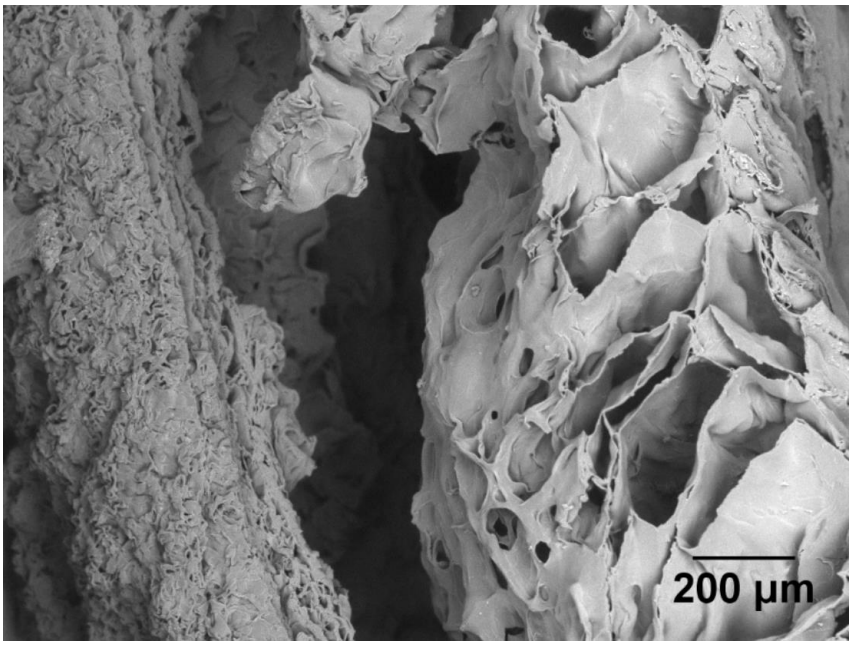

Figure A. 18 – SEM images of CHL+25%MBG scaffold.

Appendix VIII

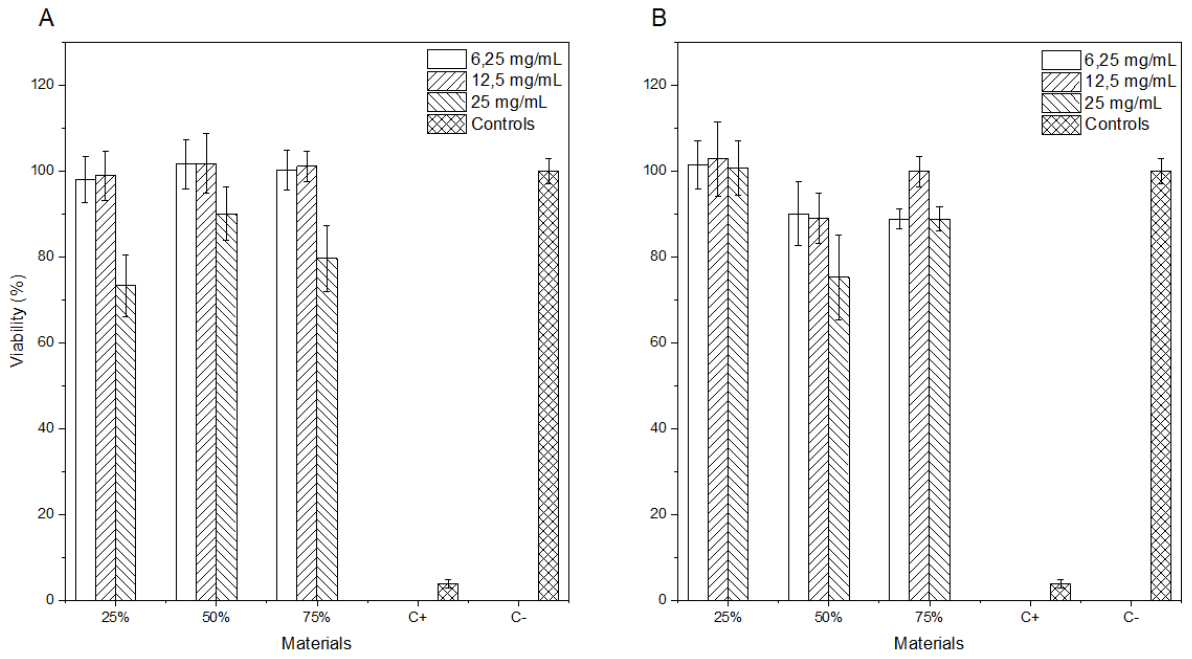

Figure A. 19 – Relative Cell Viability in cytotoxicity tests of composite membranes with FR ceramic and CHL (graphic A) or CHH (graphic B) scaffolds with different ceramic wt.% (25%, 50% and 75%). Data obtained from a sample of four replicas for each scaffold.

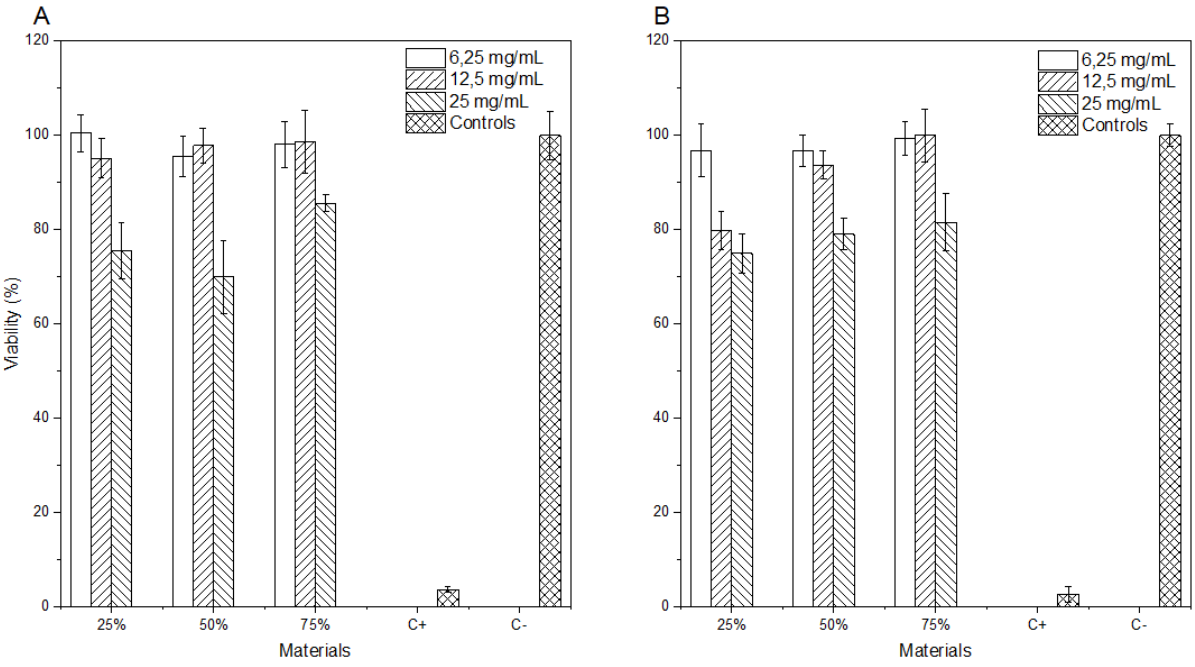

Figure A. 20 – Relative Cell Viability in cytotoxicity tests of composite membranes with MHAp ceramic and CHL (A) or CHH (B) scaffolds with different ceramic wt.% (25%, 50% and 75%). Data obtained from a sample of four replicas for each scaffold.

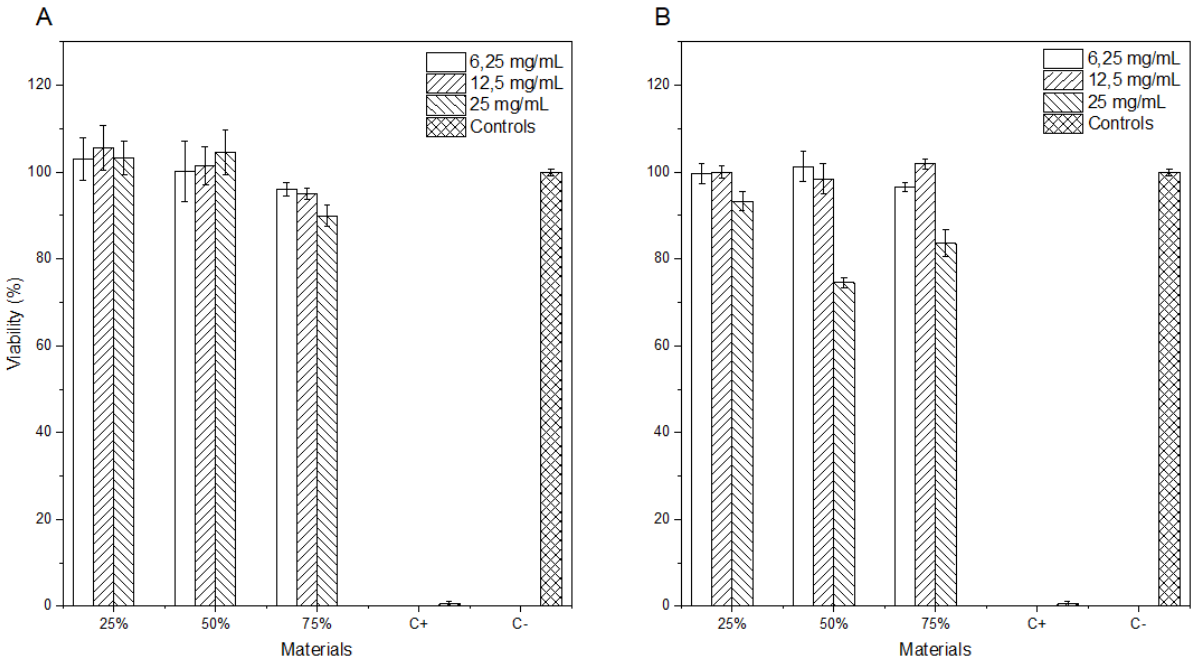

Figure A. 21 – Relative Cell Viability in cytotoxicity tests of composite membranes with MBG ceramic and CHL (A) or CHL (B) scaffolds with different ceramic wt.% (25%, 50% and 75%). Data obtained from a sample of four replicas for each scaffold.

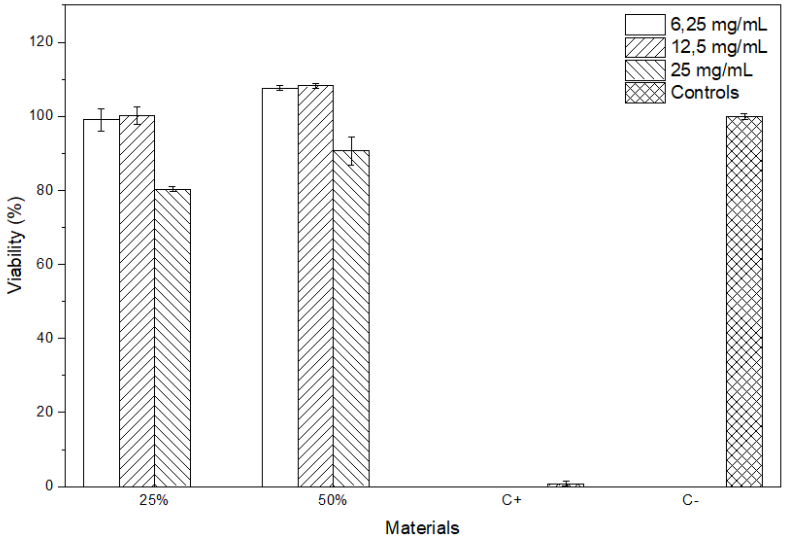

Figure A. 22 – Relative Cell Viability in cytotoxicity tests of composite membranes with MBG and MHAp ceramic with CHL. Data obtained from a sample of four replicas for each scaffold.

Table A. 5 - Cell Adhesion to composite materials in percentage (%).

Ceramic Materials	**Ceramic concentration**	
	Low (25%)	High (75%)
FR	25 ± 3	40 ± 2
MHAP	14 ± 3	42 ± 3
MBG	54 ± 3	25 ± 3
MC*	62 ± 8	56 ± 8

* in the MC composites, the high concentration is 50%

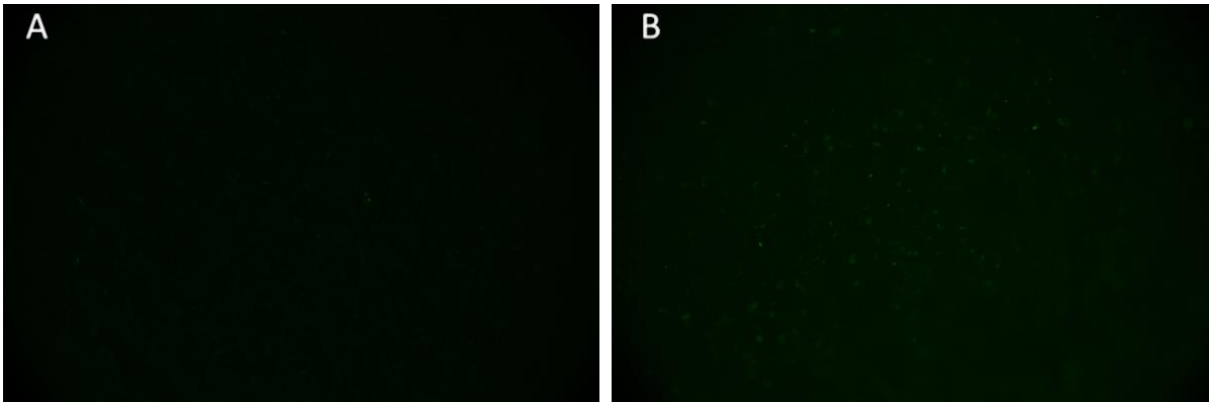

Figure A. 23 - Fluorescence images of MHAp with 25% (A) and 75% (B) of ceramic concentration.

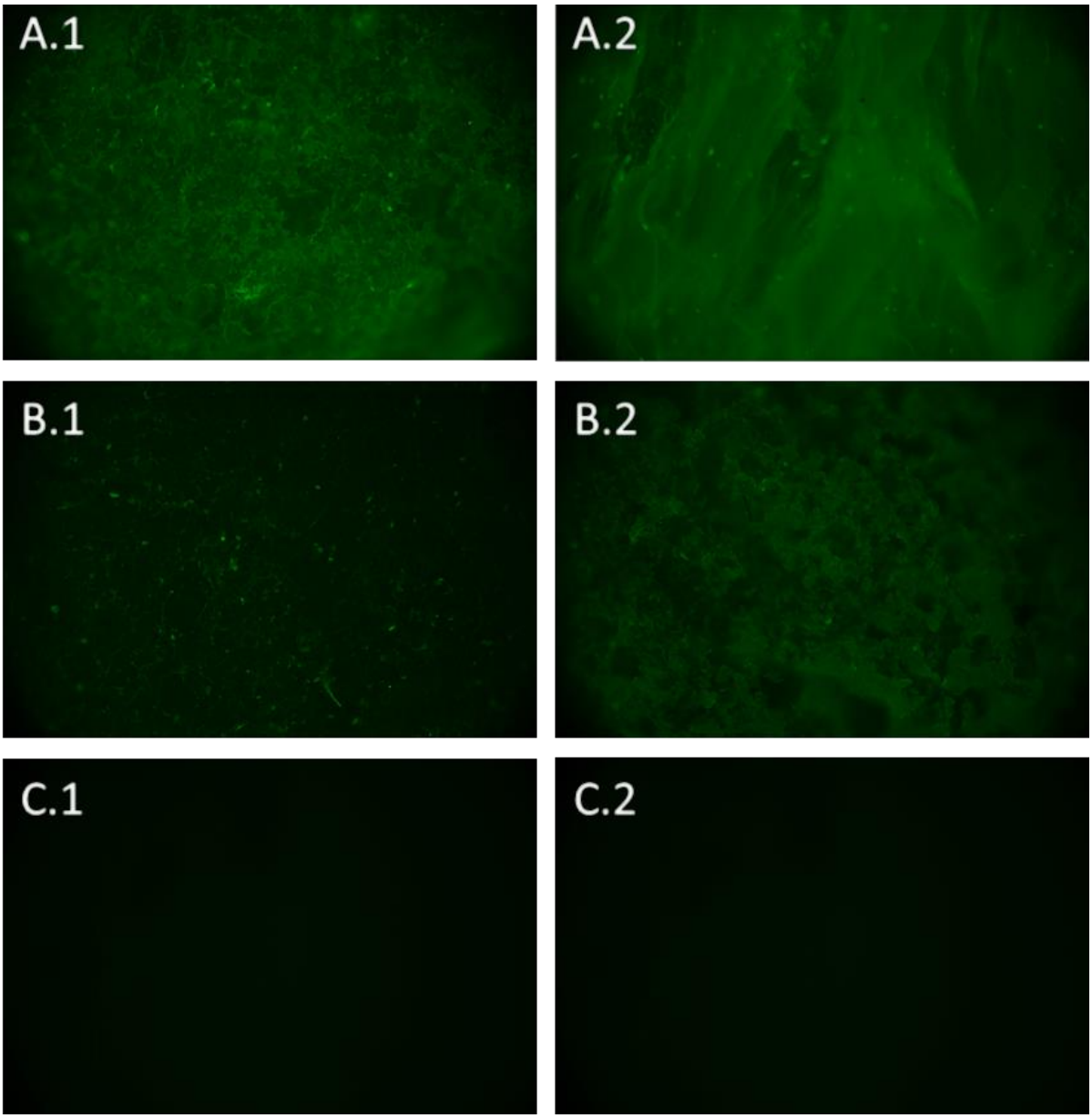

Figure A. 24 - Material controls for the Fluorescence images of FR (A), MBG (B) and MC scaffolds (C) with low (1) and high (2) ceramic concentrations.

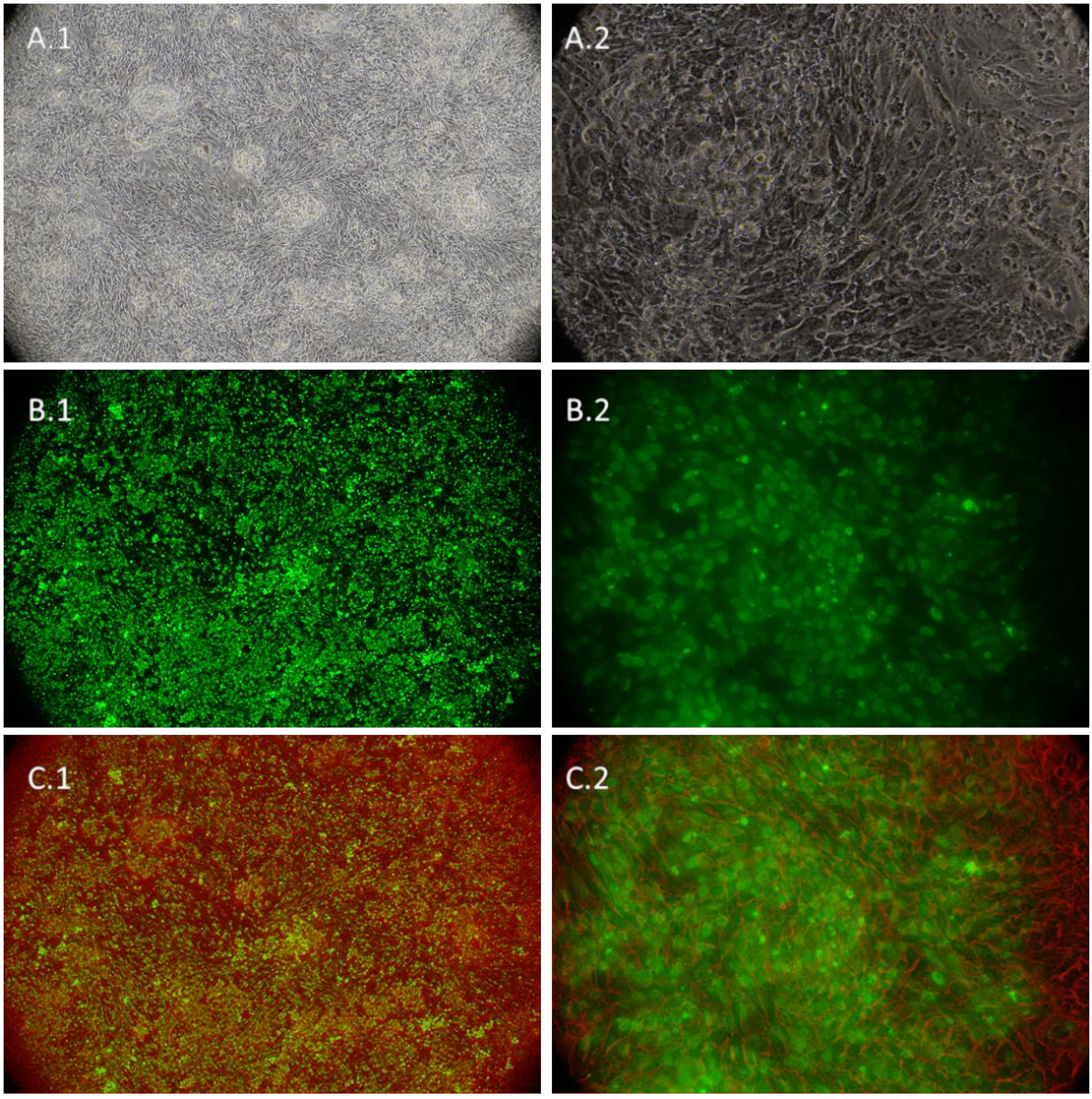

Figure A. 25 - Cell controls for the Fluorescence images (1 and 2), in transmittance (A), fluorescence (B) and conjugations of the two images (C).